

Investigating the Effect of Aerodynamic Damping on an Axial Flow Fan Blade

by

Nico Raymond Basson



*Thesis presented in partial fulfilment of the requirements for
the degree of Master of Engineering in Mechanical
Engineering in the Faculty of Engineering at Stellenbosch
University*

Supervisor: Dr. S.J. van der Spuy

Co-supervisor: Dr. D.N.J. Els

December 2015

Declaration

By submitting this thesis electronically, I declare that the entirety of the work contained therein is my own, original work, that I am the sole author thereof (save to the extent explicitly otherwise stated), that reproduction and publication thereof by Stellenbosch University will not infringe any third party rights and that I have not previously in its entirety or in part submitted it for obtaining any qualification.

Date: 2015/08/20

Copyright © 2015 Stellenbosch University
All rights reserved.

Abstract

Investigating the Effect of Aerodynamic Damping on an Axial Flow Fan Blade

N.R. Basson

*Department of Mechanical and Mechatronic Engineering,
University of Stellenbosch,
Private Bag X1, Matieland 7602, South Africa.*

Thesis: MEng (Mech)

December 2015

Axial flow fans used in air-cooled condensers experience a variation in blade loading due to distorted inlet flow patterns and obstacles in close proximity to the fan blades. The fan blades vibrate at their natural frequencies when excited. Observations made during the operation of these fans have shown that the vibrational response exhibited by the blades varies with angle of attack. This phenomenon is suspected to be due to aerodynamic damping.

The purpose of this study was to investigate the influence of aerodynamic damping on the vibrational behaviour of a generic flat plate axial flow fan blade. The blade's structural vibrational properties were determined at vacuum conditions in a purpose designed and built vacuum chamber. Experiments were subsequently conducted in a large wind tunnel at various flow velocities, with the blade's setting angle altered between data sets.

The blade's measured damped frequency and damping ratio was shown to be proportional to air density. The total damping was further shown to be proportional to the airflow velocity at which the blade was excited, with a greater increase noted at large setting angles.

Phenomena noted during the investigation were validated numerically using a dynamic Euler-Bernoulli beam model. The model performed well for instances of static atmospheric conditions, but was unable to replicate results obtained from wind tunnel experiments. Trends noted during the vacuum chamber experiments were successfully replicated.

Examination of the trends exhibited by the experimental results suggest a complex fluid interaction with the blade. It is therefore recommended that a fluid-structure-interaction analysis be performed.

Uittreksel

Onderzoek na die Uitwerking van Aërodinamiese Demping op 'n Aksiaalwaaierlem

(“Investigating the Effect of Aerodynamic Damping on an Axial Flow Fan Blade”)

N.R. Basson

*Departement Meganiese en Megatroniese Ingenieurswese,
Universiteit van Stellenbosch,
Privaatsak X1, Matieland 7602, Suid Afrika.*

Tesis: MIng (Meg)

Desember 2015

Aksiaalwaaier wat gebruik word in lugverkoelde kondensors ondervind wisselende lembelasting a.g.v. verwronge invloei-patrone en hindernisse naby die waaierlemme. Die waaierlemme vibreer teen hulle natuurlike frekwensies wanneer hulle opgewek word. Waarnemings tydens die bedryf van die waaier het gewys dat die vibrasie-reaksie by die lemme verskil soos wat die invalshoek verander. Hierdie verskynsel is moontlik a.g.v. aërodinamiese demping.

Die doel van hierdie studie is om die invloed van aërodinamiese demping op die vibrasie-gedrag van 'n generiese plat-plaat aksiale waaierlem te ondersoek. Die lem se strukturele vibrasie-eienskappe word bepaal onder vakuumtoestande in 'n doel-geboude vakuumkamer. Eksperimente is hierna gedoen teen verskeie vloeisnelhede in 'n groot windtonnel met die lem se monterhoek as veranderlike in die datastelle.

Die lem se gemete dempings-frekwensie en dempings-verhouding is in verhouding met lugdigtheid. Die totale demping is verder eweredig aan die lugvloeisnelheid waarteen die lem opgewek raak, met 'n hoër verhoging teen 'n groter invalshoek.

Verskynsels wat waargeneem is tydens die ondersoek is numeries geëvalueer deur gebruik te maak van 'n dinamiese Euler-Bernoulli-balkmodel. Die model het goed presteer tydens statiese atmosferiese toestande, maar die resultate van die windtonnel eksperimente kon nie dupliseer word nie. Tendense waargeneem tydens die vakuumkamer eksperimente is suksesvol gedupliseer.

Nadere ondersoek van die tendense deur die eksperimentele data toon 'n komplekse vloeï-interaksie met die lem. Daar word dus voorgestel dat 'n vloeï-struktuur-interaksie analise gedoen word.

Acknowledgements

I would like to express my sincere gratitude to the following people for their involvement in helping me complete this work:

- My supervisors, Dr. Johan van der Spuy and Dr. Danie Els, for their guidance, assistance and encouragement,
- Jacques Muiyser for the exchange of ideas and his kind words or encouragement,
- The personnel at the Mechanical and Mechatronic Engineering workshop for their assistance in manufacturing, advice, positive attitude and the use of their equipment.

Dedications

This thesis is dedicated to Liz, whose never-ending love and support makes anything seem possible.

Contents

Declaration	i
Abstract	ii
Uittreksel	iii
Acknowledgements	v
Dedications	vi
Contents	vii
List of Figures	x
List of Tables	xiv
Nomenclature	xv
1 Introduction	1
1.1 Background	1
1.2 Problem Definition	4
1.3 Objectives and Scope of Research	4
1.4 Outline of the Thesis	5
2 Literature Review	6
2.1 Blade Loading and Vibration	6
2.2 Aerodynamic Damping	7
2.3 Added Mass	8
2.4 Inertial Coupling	10
2.5 Vortex Induced Vibration	11
2.6 Modelling Vibration and Damping	12
3 Quantifying the Structural Properties of the Fan Blade	13
3.1 The Experimental Fan Blade	13
3.2 Strain Gauge Measurement	15
3.3 Static Deflection Tests	16

3.4	Determining the Young's Modulus	21
3.5	FRF Analysis	23
4	Vacuum Chamber Experiments	27
4.1	Experimental Setup	27
4.2	Experimental Procedure	33
4.3	Results	34
5	Wind Tunnel Experiments	42
5.1	The Wind Tunnel	42
5.2	Experimental Setup	44
5.3	Calibration	47
5.4	Experimental Procedure	52
5.5	Results	54
6	Numerical Evaluation	65
6.1	Modelling Beam Vibration	65
6.2	Discretization Method and Solver	69
6.3	Modelling Cases	70
6.4	Results	72
6.5	Advantages and Limitations of the Numerical Model	77
7	Conclusions and Recommendations	78
7.1	Quantifying the Structural Properties of the Fan Blade	78
7.2	Vacuum Chamber Experiments	79
7.3	Wind Tunnel Experiments	79
7.4	Numerical Evaluation	80
7.5	Recommendations for Future Work	80
	Appendices	81
A	Low Pass Filter Design	82
A.1	Kaiser-Bessel Window	82
A.2	LP Filter Implementation and Evaluation	84
B	Analytical Evaluation of Blade Dynamics	87
B.1	Blade Velocity	87
B.2	Angle of Attack	89
B.3	Sample Calculations	90
C	Wind Tunnel Experiments - Additional Information	93
C.1	Base Excitation Analysis and Modification	93
C.2	Determining Measurement Intervals	95
C.3	Flow Calculations	97
C.4	Blade Mount Failure and Modification	99

<i>CONTENTS</i>	ix
D Determining The Damping Ratio	103
D.1 Common Vibration Parameters	104
D.2 Base Excitation of a Viscously Damped Cantilever Beam	104
E Blade Lift and Drag Data	110
List of References	112

List of Figures

1.1	Diagrammatic representation of the Rankine cycle.	1
1.2	Sketch of A-Frame air-cooled condenser, modified from Venter (1990).	2
2.1	Geometries subject to an added mass equal to $\rho\pi a^2$, for the indicated direction of motion.	9
2.2	Cylindrical bluff body subject to vortex induced vibration.	11
3.1	Diagram of the axial flow fan selected for the investigation.	13
3.2	Experimental axial flow fan blade with full bridge strain gauge arrangement. Strain gauges in the figure are loaded as if there is a positive bending moment (M_y) acting on the blade.	14
3.3	Wheatstone bridge strain gauge arrangement used to measure bending stresses experienced by the fan blade during experimentation.	15
3.4	Exploded view detailing how the fan blade was secured in the blade mount jig.	17
3.5	Static deflection experimental setup.	18
3.6	Tip displacement, D_{tip} relative to measured strain for both the single load and the multiple load case, with a line of best fit plotted through each data set.	20
3.7	Applied Moment, M relative to measured strain for both the single and multiple load case, with a line of best fit plotted through the collective data.	20
3.8	Tip Displacement, D_{tip} relative to the applied moment experienced by the blade for both the multiple load and single load cases, with a line of best fit plotted through each data set.	23
3.9	FRF analysis setup, detailing the relative placement and designation of each accelerometer.	24
3.10	Acceleration, A in relation to frequency for all four accelerometers attached to the blade.	25
4.1	Detailed view of the experimental setup, with the walls of the vacuum chamber sectioned.	28
4.2	Exploded view of the blade mount end-cap assembly, illustrating the placement of the relevant seals and components.	29

4.3	Tip deflection mechanism used to impart a state of free vibration on the fan blade.	31
4.4	Configuration of equipment used during the vacuum chamber experiments.	32
4.5	Blade free response measured at a gauge pressure of -90 kPa.	35
4.6	Detailed view of figure 4.5 taken 15s from the start of free vibration and examined over a range of 2s.	36
4.7	Damped frequency, f_d in relation to gauge pressure for three tests, with a line of best fit plotted through all resulting points.	37
4.8	Positive peak strain values plotted on a semi-log scale relative to time, with a line of best fit plotted through the combined data sets.	38
4.9	Series of plots illustrating the increasing linearity of the blades free vibration, during the first few seconds of recorded data.	39
4.10	Detailed view of figure 4.8 taken 13s from the start of free vibration and examined over range of 4s.	40
4.11	Combined plot depicting logarithmic decrement, δ and damping ratio, ζ relative to gauge pressure.	41
5.1	Stellenbosch large wind tunnel facility modified from Du Buisson (1988).	43
5.2	Mechanical actuation mechanism used to apply base excitation to the fan blade.	44
5.3	Experimental setup, at a setting angle of 0° , located inside the wind tunnel test section.	45
5.4	External wind tunnel experimental setup, depicting data acquisition layout.	46
5.5	Betz manometer pressure, P_{Betz} relative to measured pressure transducer output voltage.	47
5.6	High speed camera calibration setup.	49
5.7	Screenshot detailing the process used to determine the pixel to millimetre conversion factor, using a reference image.	50
5.8	Screenshot detailing the process used to determine the blade tip amplitude, in pixels.	50
5.9	Tip displacement, D_{tip} relative to measured strain, determined by halving the calculated amplitude.	51
5.10	Motion transmissibility ratio, X/Y relative to frequency ratio, for fan blade tested at γ of 0°	57
5.11	Motion transmissibility ratio, X/Y relative to frequency ratio, for fan blade tested at γ of 5°	57
5.12	Motion transmissibility ratio, X/Y relative to frequency ratio, for fan blade tested at γ of 6°	58
5.13	Motion transmissibility ratio, X/Y relative to frequency ratio, for fan blade tested at γ of 7°	58

<i>LIST OF FIGURES</i>	xii
5.14 Motion transmissibility ratio, X/Y relative to frequency ratio, for fan blade tested at γ of 8°	59
5.15 Motion transmissibility ratio, X/Y relative to frequency ratio, for fan blade tested at γ of 9°	59
5.16 Total Damping Ratio, ζ relative to airflow velocity, for the setting angles under investigation, with a line of best fit plotted through each data set.	61
5.17 Average blade deflection relative to the recorded measurement, with the average deflection prior to base excitation plotted as a dashed line.	63
6.1 Blade angle of attack (α) during vibration and in the presence of a uniform airflow, while at a setting angle $\gamma = 0^\circ$	67
6.2 Drag force imparted on vibrating blade, under static atmospheric conditions.	68
6.3 Schematic illustrating the discretization of the blade, for the case in which it has been split into 10 equal segments and the boundary condition at $i = 1$ corresponds to the base excitation variation of equation 6.4.	69
6.4 Combined plot depicting transmissibility ratio, X/Y and damping ratio, ζ relative to number of blade divisions.	73
6.5 Results obtained during numerical free vibration evaluation.	74
6.6 Numerically determined motion transmissibility ratio, X/Y relative to frequency ratio, for a blade at atmospheric and vacuum conditions.	75
6.7 Numerically determined motion transmissibility ratio, X/Y relative to frequency ratio, for base excitation of the blade at various airflow velocities ($\alpha = 0^\circ$).	76
A.1 Low-pass filter design.	82
A.2 Comparison between the raw data and filtered data of the blade, while in a state of free response. The data was obtained during the course of the vacuum chamber experimentation described in chapter 4, at a gauge pressure of -90 kPa.	85
A.3 Evaluation of filter performance using a FFT analysis of the data depicted in figure A.2.	85
B.1 Cantilever beam subject to an end load.	87
B.2 Blade setting angle.	89
C.1 Series of acceleration-time graphs depicting a portion of the time measurements taken, emphasising the improvement of the base excitation mechanism.	94
C.2 Detailed look at the base excitation mechanism, with the location of the phosphor bronze bushes emphasised.	95
C.3 Comparison of baseline motion transmissibility ratios.	96

C.4	Recorded strain vs time curve of the fan blade, for a base excitation of 10.18 Hz, emphasising the point of failure.	100
C.5	Sectioned view of base excitation mechanism assembly and unsectioned fan blade, illustrating fan blade locational fit.	101
C.6	Comparison of motion transmissibility curves before and after blade mount modification for (a) $\gamma = 0^\circ$ and (b) $\gamma = 9^\circ$	102
D.1	SDOF system subject to base excitation.	103
E.1	Lift (C_l) and drag (C_d) coefficient data relative to the blade's angle of attack.	110

List of Tables

3.1	Stiffness matrix constants.	22
3.2	Summary of results obtained during FRF analysis.	26
4.1	Summary of the fan blade's vibrational properties.	41
B.1	Summary of the blade's effective angle of attack exhibited during wind tunnel experiments, while subject to base excitation.	92

Nomenclature

Constants

- g - Gravitational acceleration
- R - Gas constant

Variables

- A - Area, acceleration, attenuation
- a - Half width
- C - Viscous damping coefficient
- D - Displacement
- E - Young's Modulus
- F - Force
- f - Frequency
- I - Area moment of inertia
- k - Gauge factor, stiffness
- L - Length
- M - Bending moment
- m - Mass
- N - Filter order
- P - Pressure, point load
- R - Resistance
- Re - Reynolds number
- r - Frequency ratio
- T - Period
- t - Time
- V - Velocity, voltage, nodal displacement
- X - Tip displacement amplitude
- Y - Base excitation amplitude
- α - Angle of attack
- β - Shape parameter

γ	-	Setting angle
ϵ	-	Strain
Δ	-	Change
δ	-	Logarithmic decrement, common ripple, boundary layer thickness
ζ	-	Damping ratio
θ	-	Angle
μ	-	Dynamic viscosity
ρ	-	Density
Σ	-	Sum
Φ	-	Phase shift
ω	-	Vibrational frequency

Subscripts

<i>a</i>	-	Added
<i>air</i>	-	Air
<i>app</i>	-	Applied
<i>atm</i>	-	Atmospheric
<i>b</i>	-	Base
<i>c</i>	-	Complimentary
<i>d</i>	-	Damped
<i>drag</i>	-	Drag
<i>dyn</i>	-	Dynamic
<i>in</i>	-	Input
<i>l</i>	-	Lift
<i>lam</i>	-	Laminar
<i>ML</i>	-	Multiple loads
<i>max</i>	-	Maximum
<i>min</i>	-	Minimum
<i>n</i>	-	Natural
<i>out</i>	-	Output
<i>PT</i>	-	Pressure transducer
<i>pass</i>	-	Passband
<i>p</i>	-	Particular
<i>tip</i>	-	Blade tip
<i>tran</i>	-	Transitional
<i>SL</i>	-	Single load
<i>stag</i>	-	Stagnation

- stat* - Static
- step* - Step
- stop* - Stopband
- turb* - Turbulent

Matrices and Vectors

- A** - Discretization matrix
- D** - Nodal degrees of freedom vector
- E** - Base excitation vector
- F** - Force matrix
- K** - Stiffness matrix
- R** - Force vector

Chapter 1

Introduction

1.1 Background

1.1.1 Thermoelectric Power Generation

There are a number of ways in which electrical power may be generated. One such method is described by the Rankine cycle. The Rankine cycle works on the principle of heating water to produce high pressure steam, which is used to drive a turbine and produce electricity. The cycle is completed by condensing the low pressure steam after it has passed through the turbine, thereby allowing it to be pumped back to the boiler and reheated.

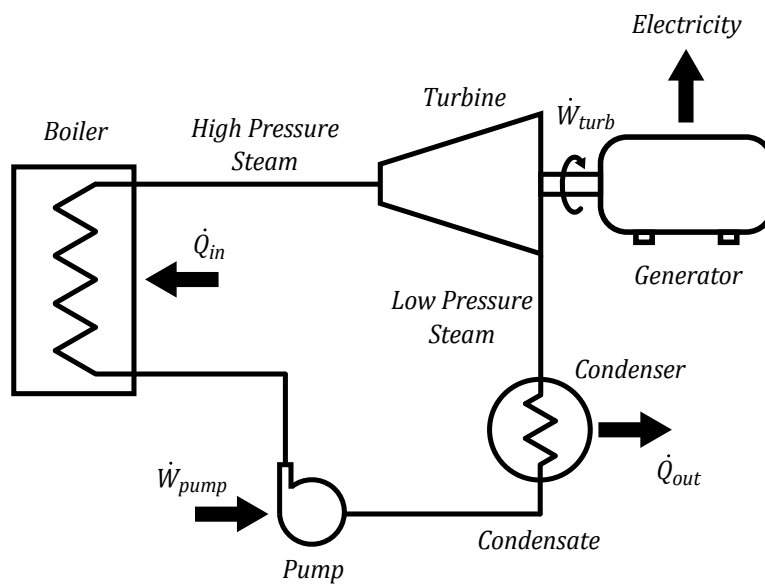


Figure 1.1: Diagrammatic representation of the Rankine cycle.

The low pressure steam is condensed by transferring its heat to a coolant, such as air or water. Air-cooling is a method of heat rejection typically employed in arid regions, in which there is little or no water available to be used as a cooling agent. This method of heat rejection is known as dry-cooling. It is advantageous, as theoretically no water is used in the cooling process. This is important as power generation in arid regions is becoming more prevalent, due to the advances being made in the renewable energy sector. The primary reason being that there is a strong correlation between dry regions and the presence of a strong solar resource.

Mechanical draft air-cooled condensers (ACC) are often used in dry-cooled thermoelectric power plants. ACCs are typically tailored to the thermoelectric power plant in which they are utilized, but the operational principles remain the same. The fan units in ACCs are arranged in arrays, the exact format of which depend on the cooling requirements of the plant in question. These arrays have been known to consist of hundreds of fan units.

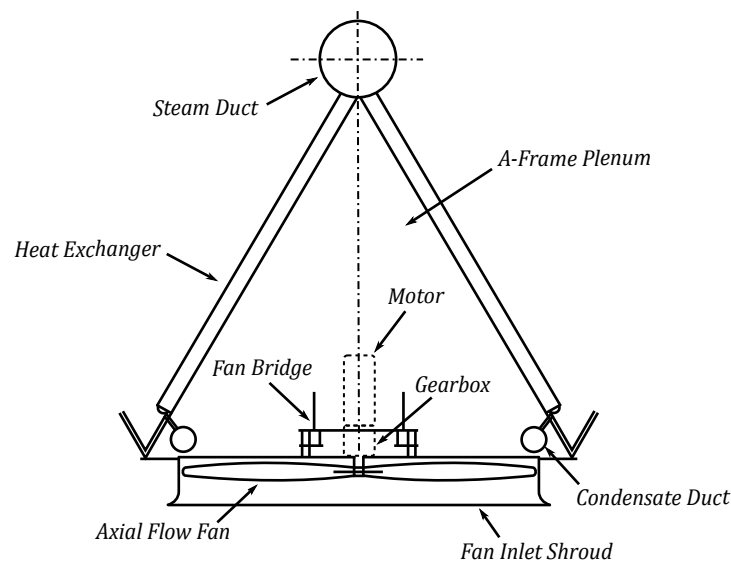


Figure 1.2: Sketch of A-Frame air-cooled condenser, modified from Venter (1990).

A diagram showing a typical A-Frame fan unit is shown in figure 1.2. The fan unit consists of an elevated structure, providing a mount for an axial flow fan and a set of inclined heat exchanger bundles. The fan blows air through the heat exchanger bundles, removing heat from the steam and bringing about its condensation. The heat exchanger bundles are configured in an A-frame arrangement, maximising the available heat transfer surface. The area between the fan and the heat exchanger bundles is known as the plenum chamber. The plenum chamber houses a fan bridge, which serves not only as a mounting point for the axial flow fan's gearbox and motor, but acts as a walkway upon which

maintenance crews may move around. It is from this fan bridge that the axial flow fan is suspended. The area below the suspended fan is occupied by an inlet shroud.

1.1.2 Fluid Structure Interaction

Vibrations are one of the major causes of mechanical and structural failure. Systems subjected to excitation frequencies approaching resonance exhibit amplified vibrational amplitudes. When the system in question is lightly damped, the vibrational amplitudes have been known to become very large. The system experiences excessive stresses and strains, which could potentially bring about catastrophic failure.

There are many examples of failure occurring due to excessive vibrational amplitudes. One such example was the collapse of the Tacoma Narrows Bridge in 1940. The bridge was excited by a 68 km/h wind, which provided an external periodic frequency. The bridge underwent twisted mode vibrations, caused by aeroelastic flutter and ultimately failed.

Aeroelastic flutter is characterised as the dynamic instability caused by the interaction of aerodynamic, elastic and inertial forces (Hodges and Pierce, 2011). In order to elaborate on this definition, it is necessary to define total damping as the sum of an object's structural and aerodynamic damping. In instances of flutter, the aerodynamic damping imparted on a structure is negative in magnitude. In a linear system, the flutter point occurs when the total damping experienced by a structure is zero and as a result the structure is subjected to simple harmonic motion. Any further decrease in the aerodynamic damping will result in the structure being subjected to negative total damping, the result of which is a continuous increase in the vibrational amplitude. Flutter may be characterised as being either hard or soft in nature. Hard flutter exhibits a sudden decrease in total damping near the flutter point, while soft flutter exhibits a gradual decrease (Wright and Cooper, 2014).

Aeroelastic flutter has been responsible for a number of aviation failures. One such incident occurred in 1997 at an air-show in Maryland, when an F-117A Nighthawk lost most of its right wing and crashed. The failure has been attributed to flutter, which was brought about by a loose elevon. Wings are not the only aircraft components subjected to flutter. A prototype of the Grob SPn business jet suffered tailplane separation in 2006, during a demonstration flight at Mindelheim-Mattsies Airport. As the pilot was preparing the aircraft for a fly-by, excessive flutter caused parts from the stabilizer to separate and the pilot lost control of the aircraft.

Fluid structure interaction is an important consideration for all dynamic applications conducted in a fluid medium. The interaction is not simply limited to a negative damping effect, but has been known to bring about positive damping as well. Positive aerodynamic damping, like structural damping, has a stabilizing effect and dissipates a system's energy.

1.2 Problem Definition

There is a considerable amount of research being done that pertains to ACCs and as a result, they are constantly being improved. It has been noted that the axial flow fans employed in ACCs are occasionally subjected to vibration. The vibration affects not only the operation of the fans, but potentially shortens their lifetime. Fatigue damage of the blades and the gearbox are a legitimate concern, making it important to develop a greater understanding of the dynamics that affect the system.

During on-site testing, adjustments were made to an ACC axial flow fan. Upon alteration of the fan blade's angle of attack, it was noted that the fan was subject to an increase in vibration (Muyser, 2014). The reason for the increased vibration was unclear and it was hypothesised that aerodynamic damping was a contributing factor. It is therefore clear that a greater understanding of aerodynamic damping, as it pertains to axial flow fans, is needed.

1.3 Objectives and Scope of Research

The primary purpose of this study was to investigate and characterize the effect of aerodynamic damping on an experimental axial flow fan blade.

The scope of the research involved the experimental and numerical investigation of an axial flow fan blade and its resulting vibrational characteristics. The study was limited to the investigation of a single axial flow fan blade, with a flat plate profile. As a result the number of variables influencing the characteristics was kept to a minimum.

A test bench was used to calibrate the blade's measured strain relative to an applied moment. The tip displacement was simultaneously measured for various loading configurations, from which a methodology was developed and implemented to determine the unknown structural properties of the fan blade. The same test bench was used to perform a frequency response function analysis on the blade in order to determine its approximate bending modes.

An experimental apparatus was developed that would allow the blade to be tested at conditions approaching vacuum. The blade was mounted inside the vacuum chamber and excited by means of a cam mechanism. The resulting free response was measured and the experiment was conducted at various gauge pressures. The results were analysed and used to determine the vibrational characteristics of the fan blade.

The blade was investigated under simulated operational conditions in a wind tunnel at various uniform airflow velocities. Under these conditions, the blade was subjected to controlled base excitation over a spectrum of excitation frequencies. The response of the blade was analysed and the aerodynamic influence subsequently determined. The operational conditions were further varied by altering the blade's setting angle.

The blade was analytically modelled and a numerical evaluation was performed. The evaluation provided evidence to the hypothesised reasons for phenomena encountered during the course of the investigation. The limitations of the model were determined and recommendations were made for future studies.

The relevance of this research is applicable to the implementation and design of axial flow fans. By increasing the level of understanding surrounding the blade's vibrational behaviour, the effective lifetime of the blades and any accompanying equipment may be improved. Existing research into the field of aerodynamic damping is primarily concerned with its effect on turbomachinery and flutter associated with airfoils. Limited research has been conducted with regards to the aerodynamic damping effect on axial flow fans. This research serves as a starting point from which further studies may be conducted. Knowing the vibrational characteristics of the experimental fan blade will make it possible to perform accurate fluid structure interaction (FSI) analyses in the future.

1.4 Outline of the Thesis

The thesis is laid out as follows. Chapter 1 examines the background of the study. The objectives and scope of the research are discussed, followed by a brief breakdown outlining the thesis.

In chapter 2, a detailed literature review of aerodynamic damping is given. It contains all the relevant sources which have been referenced in the chapters that follow.

Chapter 3 details the static deflection tests used in the calibration of the blade's strain gauges. The procedure used to determine the unknown structural properties of the blade has been described, along with a FRF analysis which was conducted on the blade.

Chapter 4 contains all relevant information pertaining to the experiments conducted on the blade, while inside a vacuum chamber. The results were used to determine the blade's vibrational characteristics at vacuum conditions.

Chapter 5 describes the base excitation tests which were conducted on the fan blade, in Stellenbosch University's large wind tunnel facility. The facility was operated at various airflow velocities and the blade's setting angle was varied between data sets.

Chapter 6 evaluates the proposed reasons for phenomena identified over the course of the investigation. An analytical model was selected and subsequently solved numerically.

The final conclusions are drawn in chapter 7, along with recommendations for future studies.

Chapter 2

Literature Review

2.1 Blade Loading and Vibration

A fan operating under ideal inlet air flow conditions is expected to experience constant blade loading. The blade loading is dependent on factors such as the volumetric air flow rate, the setting angle of the fan blades and the rotational velocity of the fan in question. These factors determine the effective angle of attack of the fan's blades and thereby influences its lift and drag characteristics. It is therefore reasonable to assume that the aerodynamic load imparted on the blades will vary, when the fan is exposed to distorted inflow conditions.

Bredell *et al.* (2006) numerically investigated the bending moments exerted on axial flow fans subject to distorted inlet air flow conditions. It was found that as fan blades approached the windward side of the fan, the blade loading increased. It was determined that the variation in blade bending moments could exceed the steady loading condition by as much as 70%. Bredell went on to discover that the addition of a solid platform, spanning the upstream flow area of the fan, reduced the peak blade bending moments.

Muiyser *et al.* (2014) measured the bending load of a fullscale ACC axial flow fan during operation. The measurements were obtained by attaching strain gauges to the neck of a single fan blade, which was located at the edge of the ACC in question. The results obtained over the course of the investigation revealed that the blade experienced large vibrations at its natural frequency of 6 Hz. In addition to large vibrations at its natural frequency, the blade was also found to possess significant vibrational contributions at frequencies corresponding to 2 Hz and 4 Hz respectively. It was noted that the rotational speed of the fan was equal to one third the natural frequency of the blade. It was therefore determined that the third harmonic of the fan's rotation speed was exciting the blade. Another vibrational contribution occurred at a frequency which was twice that of the rotational speed of the fan and was attributed to the fan passing beneath the fan bridge. Muiyser went on to show that the aerodynamic load on the fan was periodic, with a large peak in

blade loading occurring at the windward side of the fan.

2.2 Aerodynamic Damping

Damping may be defined as the dissipation of energy with regards to time or distance (Harris and Piersol, 2009). This dissipation of energy is typically described by adding a $C\dot{x}$ term to an object's equation of motion, where C is a constant and \dot{x} is the velocity of the object undergoing vibration. This type of damping shows a good correlation to physically observed phenomena and is known as viscous damping (Inman, 2009).

For systems possessing positive mass, damping and stiffness coefficients, there are three types of viscous damping. Underdamped motion occurs when a system's damping ratio is less than one and results in the oscillatory decay of its motion. The damping ratio for underdamped motion dictates the rate of decay of motion. Overdamped motion occurs when a system's damping ratio is greater than one, which results in the system being free of oscillation. Overdamped systems exponentially return to their rest position. Critically damped motion occurs when a system's damping ratio is equal to one. These systems may be thought of as possessing the smallest damping ratio that results in non-oscillatory motion. Critically damped systems are largely dependent on their initial conditions and provide the fastest return to zero, absent of oscillation.

A object surrounded by a fluid experiences a change in its vibrational characteristics. Blevins (2009) quantifies the change as an increase in natural frequency and damping ratio of the object.

Kammerer and Abhari (2009) conducted an investigation on a centrifugal compressor rotor, which was constructed out of aluminium. The total damping was measured during operation and the structural damping was subtracted to obtain the aerodynamic damping component. The results of the investigation suggested that the aerodynamic damping was proportional to the inlet pressure of the compressor. It was further noted that aerodynamic damping dominated the overall damping, a statement illustrated by the fact that at an inlet pressure of 1 bar, the aerodynamic damping was higher than the structural damping by a factor of 10.

Tarnopolsky *et al.* (2002) investigated the aerodynamic damping of oscillating plates of various shapes and sizes in both stationary and moving air. The plates were placed normal to the direction of air flow and excited to oscillate parallel to the flow direction. The aerodynamic damping was found to be significantly larger while the air was moving, than the aerodynamic damping determined while the air was stationary. Furthermore, the aerodynamic damping was found to vary linearly with regards to the flow velocity. Experiments were conducted for instances of constrained and unconstrained flow. From these experiments, it was determined that the aerodynamic damping

component did not largely depend on the flow direction, but rather on the air density.

Kimber *et al.* (2009) investigated the change in aerodynamic loading experienced by a beam, when it was configured in an array with another beam of similar geometry, material properties and subsequently, vibrational properties. The experiments took place at various atmospheric pressures, including those approaching vacuum. Once more, it was shown that the objects under investigation exhibited a reduction in their damping ratios, as the pressure in which the investigation was conducted was decreased.

The change in an object's damping ratio may better be understood when one considers the quantification of the force imparted on the object by the surrounding fluid. Blevins (1977) has stated that an object vibrating in air or a fluid experiences a force proportional to the square of its velocity. As a result, Inman (2009) has quantified the damping force as

$$F = \frac{C_d \rho A}{2} \operatorname{sgn}(\dot{x}) \dot{x}^2 \quad (2.1)$$

where \dot{x} is the velocity of the object, C_d is its drag coefficient, ρ is the fluid density and A is the cross-sectional area of the object. It should be apparent that this equation is simply the drag force imparted on the object by the surrounding fluid, which is valid when the object is vibrating in a stagnant fluid medium.

2.3 Added Mass

An object vibrating in a fluid medium such as air, is subject to more than simply an altered damping component. Sources such as Kimber *et al.* (2009) and Kammerer and Abhari (2009) have stated that objects vibrating in air experience an added mass effect. Kimber *et al.* (2009) noted that experiments conducted on vibrating cantilever beams under atmospheric conditions possessed lower natural frequencies than the same beams tested under vacuum conditions. It was determined that the added mass due to the presence of air resulted in a reduction of the natural frequency. Kielb and Abhari (2003) noted the same reduction in natural frequency while conducting experiments on a turbine, in a shock tunnel.

A moving body encompassed by a fluid draws the fluid along with it. This entrainment of fluid results in an increase in the body's perceived mass, which is referred to as the added mass or virtual mass effect (Blevins, 2009). The increased mass results in a reduction in the body's natural frequency, a consideration which is particularly important when the fluid density approaches that of the structure. The added mass is directly proportional to the density of the fluid multiplied by a factor, which varies with regards to the cross-sectional geometry of the body. The added mass term for a flat plate may be calculated

using

$$m_a = \rho\pi a^2 \quad (2.2)$$

where ρ is the density of the fluid and a is half the width of the plate. It should be noted that m_a is the added mass per unit length of the object in question. The added mass expression for a flat plate is identical to the expression for an object in possession of a elliptical or round cross-section, as illustrated in figure 2.1.

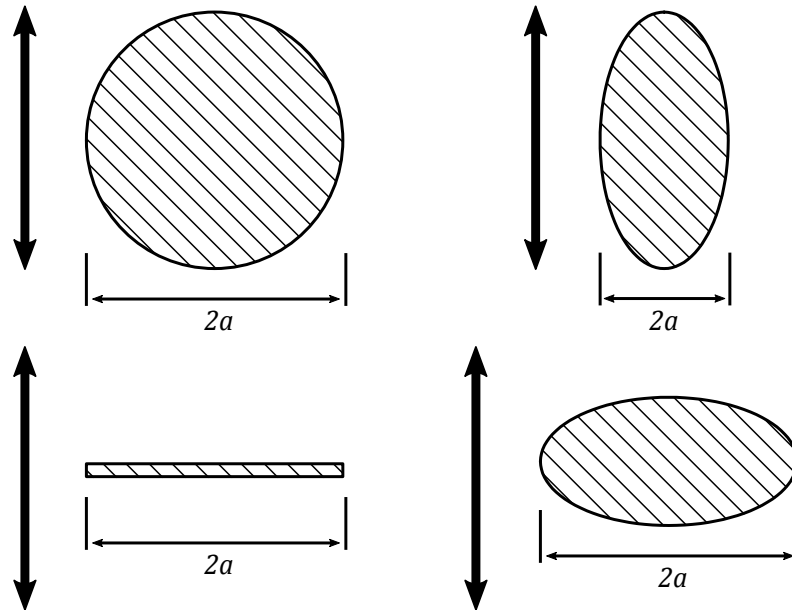


Figure 2.1: Geometries subject to an added mass equal to $\rho\pi a^2$, for the indicated direction of motion.

The added mass phenomenon is particularly prevalent for fluids with large densities, such as sea water. It is therefore not surprising that research conducted into the effect of added mass is commonly conducted on objects submerged in water. Vu *et al.* (2007) conducted experiments on a plated structure, which had been submerged in water. It was observed that the added mass increased along with the depth of the plate. It was also noted that the added mass would converge once a specific depth had been attained. The depth was found to vary depending on the geometry of the submerged plate in question. As an additional point, Vu *et al.* (2007) noted that the effect of added mass was most significant for the first bending mode. The effect decreases considerably for higher bending modes. The effect of added mass related to torsional modes was noted to remain nearly constant. Sedlar *et al.* (2011) reported similar findings from a set of experiments in which a cantilever beam was partially submerged in water.

When considering equation 2.2 it is apparent that for objects in the presence of low density gasses such as air, the added mass effect would ordinarily be negligible. The exception would however occur in instances in which the weight of the object itself is relatively small. Typical light structures which may be affected include things such as aircraft or spherical projectiles e.g. a ball.

Shirzadeh *et al.* (2012) illustrated the added mass effect of air on a vibrating object, with limited weight. This was accomplished by conducting a set of experiments on a piezoelectric fan in a vacuum box at atmospheric and vacuum conditions. The beam was incrementally excited from 80 Hz to 130 Hz and the vibration measurements were performed using a Scanning Laser Doppler Vibrometer. Frequency response function (FRF) curves were plotted for both cases. The damping ratio at vacuum was found to be 0.23%, while at atmospheric conditions, it was 0.69%. Additionally, the natural frequency of the fan was found to vary between the two experiments. The natural frequency was determined to be 118.9 Hz at atmospheric conditions, while at vacuum conditions it increased to 119.2 Hz. The frequency shift was attributed to the increased mass of the fan, as a result of the added mass of the displaced air.

2.4 Inertial Coupling

Inertial coupling within the context of aerodynamic damping, as it pertains to axial flow fan blades, refers to the effect whereby the aerodynamic loading of a single beam or blade is altered when it is configured in an array. This effect has been described by Blevins (2009) as the coupled vibration of an elastic structure to adjacent structures, with dense fluid forming the bridge between the two. The effect under consideration is unlikely to occur in axial flow fans, based on the typical low solidity of fan rotors. The effect is more likely to be experienced in turbine and compressor rotors owing to the large number of blades and therefore, the reduced distance between successive blades.

Kimber *et al.* (2009) investigated the aerodynamic coupling in arrays of macro-sized vibrating cantilevers. This was achieved by investigating the in-phase and out-of-phase vibration of two piezoelectric fans orientated firstly in a face-to-face orientation and then in an edge-to-edge orientation. It was shown that there was a decrease in fluid damping for in-phase vibration, while the opposite was true for out-of-phase vibration. It was also shown that the coupling effect was dependent on the distance between the cantilevers, a fact which held true regardless of the orientation or phase difference. Additionally, it was found that for the face-to-face configuration, the dependence on distance showed a strong correlation to vibration amplitude. The dependence for the edge-to-edge configuration however was found to be dependent on the beam width.

2.5 Vortex Induced Vibration

Vortex induced vibration may be described as the phenomenon whereby a structure resonates with the periodic components of an induced wake (Blevins, 2009). It is most common with bluff bodies, which are characterized by their abrupt contours.

As the fluid flows around a body, it is slowed and a boundary layer is created. When the fluid is subjected to abrupt or excessive curvature, the boundary layer may separate from the body's surface and vortices are formed. The newly developed vortices change the pressure distribution along the body's surface (Cengel and Cimbala, 2010). If the body in question is not symmetric or is orientated in such a way as to generate localized vortices with regards to the body's mid-plane, the resulting change in pressure along its surface would generate non-symmetric lift. This would bring about the transverse motion of the body relative to the flow, as illustrated in figure 2.2.

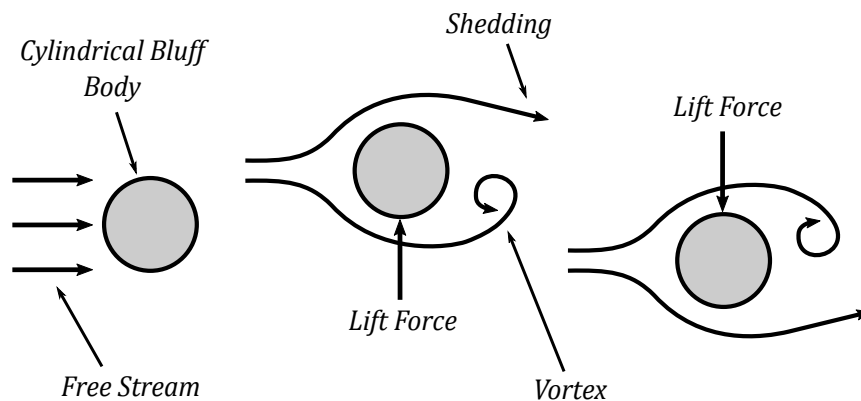


Figure 2.2: Cylindrical bluff body subject to vortex induced vibration.

Blevins (1974) developed a model for the vortex induced vibration of a circular cylinder. The model predicts that an elastically mounted cylinder resonates with vortex shedding as the shedding frequency of the cylinder approaches the cylinder's natural frequency. The result being that the cylinder will experience large amplitude oscillation.

2.6 Modelling Vibration and Damping

2.6.1 Single-Degree-of-Freedom Modelling

Fan blades may be modelled as cantilever beams. A commonly employed modelling approach is to describe the system as a single-degree-of-freedom (SDOF) system. This process involves describing the system using a mass, a spring and a linear viscous damper. SDOF freedom systems are well founded and will thus not be discussed at length. Sources such as Inman (2009) may be consulted for more information. Appendix D details the process used to formulate a SDOF model of a cantilever beam, subject to a fixed-amplitude sinusoidal base excitation.

2.6.2 Euler-Bernoulli Beam Modelling

Vibrational piezoelectric (PZT) energy harvesters convert kinetic energy into electrical energy. The most commonly investigated type of vibrational energy harvesters are cantilevered beams with PZT layers. Erturk and Inman (2008) conducted an extensive study in which it was demonstrated that the SDOF method of predicting the motion of vibrating cantilevered beams and bars may yield highly inaccurate results. It was shown that an Euler-Bernoulli beam modelling formulation would provide improved results.

Bambill *et al.* (2003) modelled a continuous beam with a mass at its free end, which was subject to forced sinusoidal excitation. Once more, the Euler-Bernoulli beam model was utilized in place of a SDOF model. The model was evaluated absent of a forcing function and the results were shown to correlate well with published data related to the static model.

Baker *et al.* (1967) introduced internal and external damping forces into the transverse Euler-Bernoulli beam equation, which was solved numerically using energy methods. The predicted decrements of free vibration were then compared to experiments conducted by previous investigators. It was found that air damping at large amplitudes was due to a drag force, which was proportional to dynamic pressure. It was further noted that drag coefficients were not constant and were proportional to a scale factor determined by tip amplitude and beam thickness. Air damping at small amplitudes was determined to be due to a drag force proportional to velocity and the damping was noted to be independent of frequency, but rather dependent on amplitude.

It may be noted from the above publications, that if the cantilever beam being modelled is subject to complex external forces or has an irregular mass distribution, a SDOF system is not the appropriate model of choice. The Euler-Bernoulli beam model was thus elected for this investigation's numerical evaluation and will be discussed in detail in chapter 6.

Chapter 3

Quantifying the Structural Properties of the Fan Blade

Before any experimentation or numerical simulations could take place, it was necessary to determine the structural properties of the axial flow fan blade under investigation. Following the same logic, the bending modes of the blade were simultaneously determined.

3.1 The Experimental Fan Blade

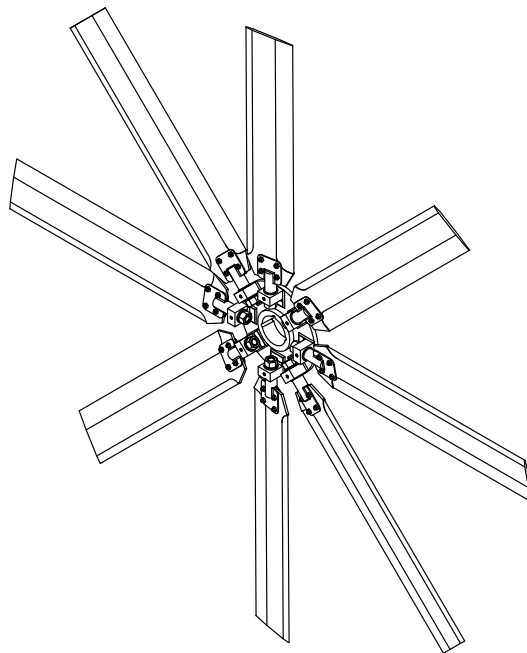


Figure 3.1: Diagram of the axial flow fan selected for the investigation.

At the outset of the investigation, it was decided to utilise a fan blade possessing a flat plate blade profile. The primary reason for using a relatively simple profile was that it was of great importance that the vibrational characteristics and the structural properties of the fan blade be accurately determined. This would be of value to not only to the investigation in question, but for future investigations into the field of study. The certainty of the determined properties would be invaluable to fluid-structure-interaction (FSI) and numerical investigations conducted in the future. This is equally true regarding the validation of the results obtained over the course of the experimentation.

It should be noted that for the purposes of the study, one of the blade assemblies has been removed from the axial flow fan rotor and will form the focus of the investigation. The fan blade in question came from the 1.5 m diameter experimental axial flow fan seen in figure 3.1. The blade has a full length of 630 mm, a chord length of 120 mm and a maximum thickness of 5 mm. The fan blade is more clearly shown in figure 3.2, where it may be noted that the blade profile is not flat, as the name suggests. The profile has been modified, in accordance with the dimensions shown in Riegels (1961), to possess the leading and trailing edge seen in the figure. This was done in order to ensure that the implementation of the lift and drag characteristics of the blade are in fact representative of the blade profile in question.

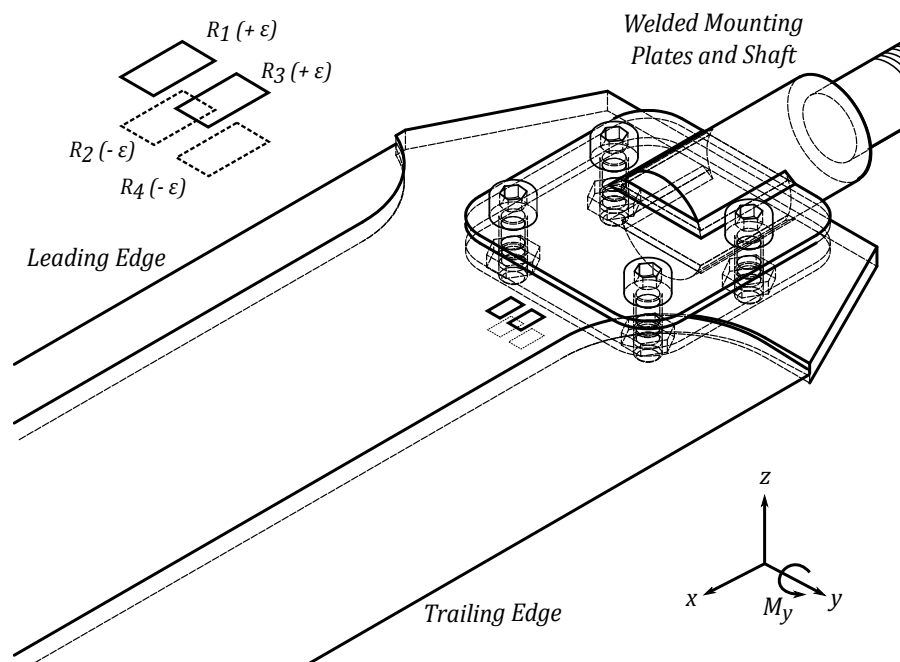


Figure 3.2: Experimental axial flow fan blade with full bridge strain gauge arrangement. Strain gauges in the figure are loaded as if there is a positive bending moment (M_y) acting on the blade.

The fan blade is an assembly consisting of the aforementioned aluminium blade and a mild steel mounting piece responsible for attaching it to the fan hub. The blade assembly has a M16 threaded shaft which passes through a hole in the hub assembly and is located by its 25 mm diameter shoulder. The blade is then adjusted to the desired angle and a grub screw is used to temporarily lock it in place. Finally, the blade is secured by tightening a retaining nut on the threaded portion of the blade's shaft. It was decided to investigate the entire blade assembly and not simply the aluminium blade profile. This would ensure that the results of the investigation provide the most accurate representation of what the blade would be experiencing during normal operational conditions.

3.2 Strain Gauge Measurement

The experiments conducted on the fan blade, over the course of the investigation, required a reliable means of measuring the blade's deflection. These proposed experiments typically take place under conditions in which it would not be possible or suitable to physically measure the deflection using conventional methods. It was therefore decided to make use of a full bridge strain gauge arrangement, which could be calibrated in order to accurately determine the blade's tip deflection relative to the measured strain.

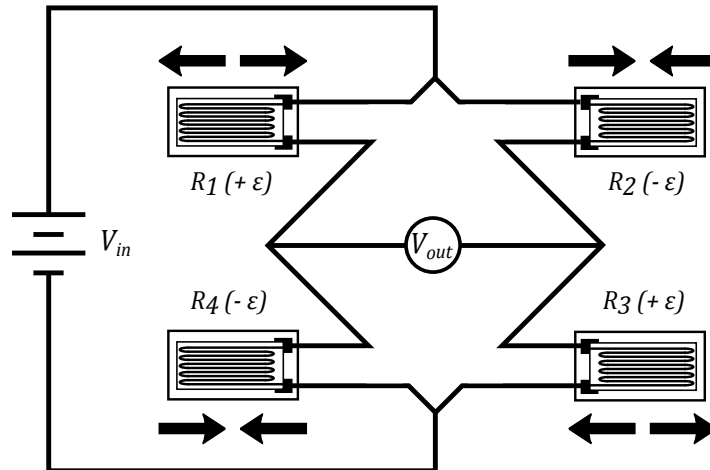


Figure 3.3: Wheatstone bridge strain gauge arrangement used to measure bending stresses experienced by the fan blade during experimentation.

Strain gauges are a type of electrical resistor which are capable of measuring small deformations that occur in a structure, when it is subjected to

a mechanical load. This is done by attaching strain gauges to the structure in question and measuring the change in resistance. This change in resistance is indirectly measured by arranging the strain gauges in a Wheatstone bridge configuration, as seen in figure 3.3. When the structure undergoes deformation, the lengths of continuous resistance wire which make up the strain gauges deform along with the structure. The resulting elongation or compression of the wires bring about a measurable change in resistance, which in turn dictates the change in the bridge output voltage. This is illustrated by

$$\frac{\Delta V_{out}}{V_{in}} = \frac{1}{4} \left(\frac{\Delta R_1}{R_1} - \frac{\Delta R_2}{R_2} + \frac{\Delta R_3}{R_3} - \frac{\Delta R_4}{R_4} \right) \quad (3.1)$$

Equation 3.1 provides a relation between the output and input voltages, as a function of the change in individual strain gauge resistances. Typically, the strain gauges possess the same resistance values and the bridge is balanced. As a result, the output voltage (V_{out}) is equal to zero, prior to the structure undergoing deformation. It should also be noted that the gauge factor (k) of selected strain gauges are typically known and may be used to express the change of resistance in terms of strain (ϵ). This relation is given by

$$\frac{\Delta R}{R} = k\epsilon \quad (3.2)$$

which may then be used in conjunction with equation 3.1 to obtain

$$\frac{\Delta V_{out}}{V_{in}} = \frac{k}{4} (\epsilon_1 - \epsilon_2 + \epsilon_3 - \epsilon_4) \quad (3.3)$$

This relation has been used to arrange the strain gauges in what is known as a full bridge configuration. The arrangement has been illustrated in figure 3.2 and allows for the measurement of the average bending strain experienced by the blade. This particular arrangement is temperature compensated and is not sensitive to axial forces acting on the blade. It should be noted that a half bridge configuration would be capable of measuring the same bending strain, but the proposed data acquisition equipment was configured to work with a full bridge configuration. In addition, the full bridge arrangement has twice the sensitivity of the half bridge arrangement.

3.3 Static Deflection Tests

A series of static deflection tests were conducted in order to determine the Young's Modulus (E) of the fan blade in question, as well as to calibrate the strain gauges discussed in Section 3.2.

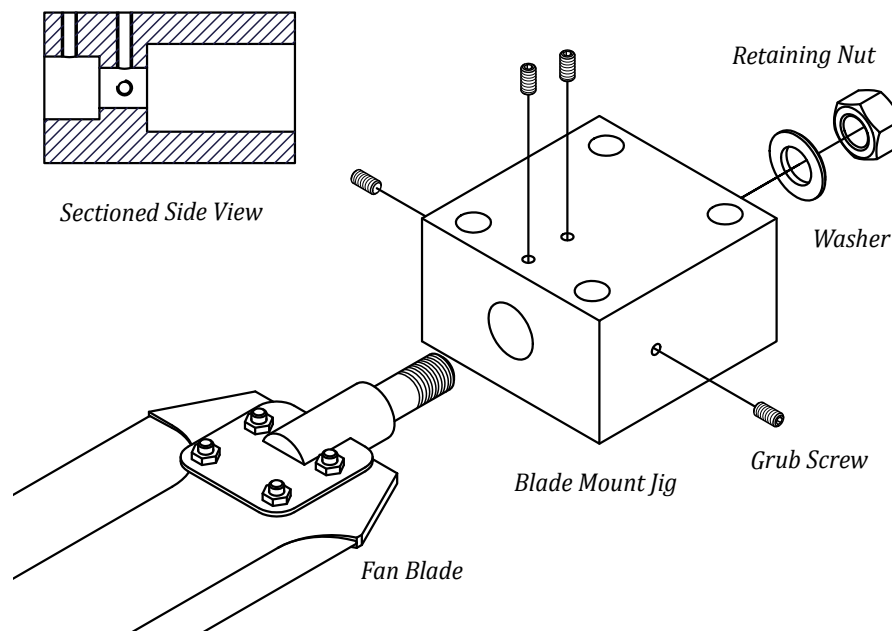


Figure 3.4: Exploded view detailing how the fan blade was secured in the blade mount jig.

3.3.1 Experimental Setup

An aluminium mounting jig was designed and machined in which the fan blade could be secured. The jig needed to be able to provide the blade with a stable mounting point, with no relative movement occurring between the blade and the jig. Furthermore, the jig would have to be modular, thereby allowing it to be used in conjunction with existing equipment. The final design can be seen in figure 3.4.

The experimental setup can be seen in figure 3.5 and consists of the blade mount jig being attached to an existing steel structure. The fan blade was inserted into the jig and a digital inclinometer was used to ensure that the flat surface of the blade was parallel to the horizontal plane. Once parallel, the blade orientation was locked by means of four separate grub screws. This made it possible to further secure the blade, by tightening a M16 nut onto the screw thread located on the shaft of the fan blade assembly. Once correctly secured and orientated, a dial gauge was attached to the base of the structure. The measuring needle of the dial gauge was then moved into contact with the blade tip. Great care was taken to ensure that that dial gauge and all of its relevant components were correctly orientated. Any deviation from desired perpendicular interaction between the needle and the blade would result in measurement error. Once satisfied that the dial gauge was correctly positioned, it was zeroed.

At this point, it should be noted that two experimental setups were explored

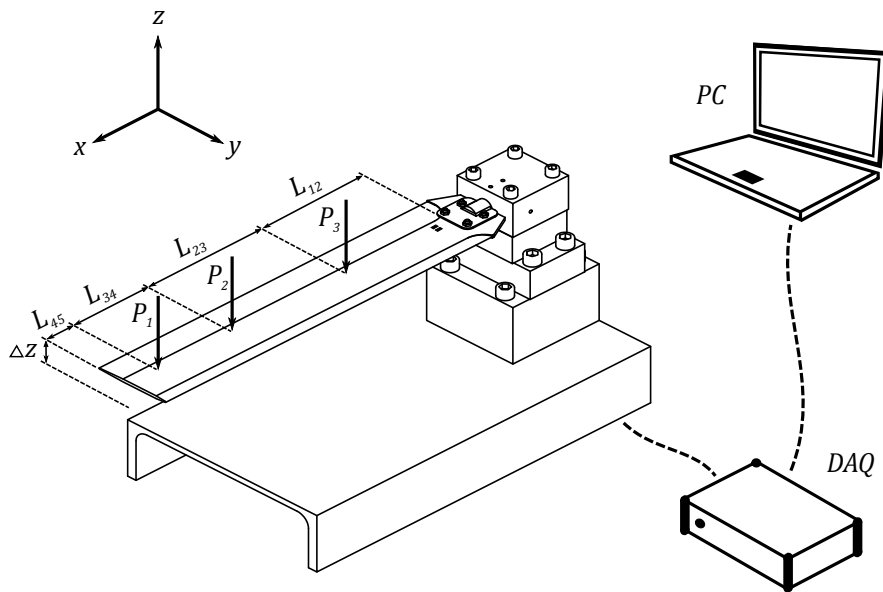


Figure 3.5: Static deflection experimental setup.

and individually tested. The first setup consisted of a single point load being applied to the blade at a fixed distance (P_1), while the second setup consisted of three point loads being applied to the blade at fixed distances (P_1 , P_2 and P_3). The reason for using two separate experimental configurations was to ensure the validity of the calibration data obtained from the static deflection experiment. The point loads were applied to the fan blade by making use of cradles of known masses. The cradles in question made contact with the blade by means of sharp needle-like tips, thereby ensuring that a point load was applied to the blade at the desired distance.

The full bridge strain gauge arrangement described in section 3.2 was used to measure the strain gauge data in $\mu\text{m}/\text{m}$, while the dial gauge was used to measure the tip deflection in mm. The strain gauges were connected to a Spider 8 data acquisition unit (DAQ) and were recorded on a laptop using Catman Easy. The DAQ was configured to sample the strain gauge data at a frequency of 600 Hz.

3.3.2 Experimental Procedure

Before the experiment was performed, the masses and the cradles used during the course of the experimentation were weighed using a calibrated digital scale. The weighed objects were marked and their masses recorded. The single point load test was performed first. A zero reading was recorded, after which one

of the three cradles was placed at the desired distance along the centreline of the blade. It should be noted that the distance in question was recorded and has been indicated in figure 3.5. A collection of small masses were then systematically placed on top of the cradle, thereby incrementally increasing the applied moment experienced by the blade. Both the tip deflection and strain were recorded for each moment applied to the blade.

Once all the masses had been applied to the blade and the subsequent measurements recorded, the experimental setup was altered by rotating the blade through 180° . The same methodology discussed in section 3.3.1 was followed with regards to the setup, before the experimental procedure described above could be repeated. The measured deflection was then effectively recorded in the negative z-direction. Upon completion of the measurements recorded in the altered orientation, the blade was rotated back to its original orientation. This entire procedure was repeated twice, thereby resulting in a total of 108 data points.

Finally, the multiple load test was conducted by following the same procedure employed for the single load test. As previously mentioned, the multiple load test consisted of using three cradles. As all the mass pieces had been used for the single load test, fewer data points could be recorded owing to the fact that the masses had to be spread between three cradles. As before, the blade was rotated through 180° after all the masses had been added to the relevant cradles and the process repeated. This procedure was conducted three times and resulted in a total of 48 data points.

3.3.3 Results

Figure 3.6 plots the recorded strain relative to the blade's tip displacement, for both the single load and multiple load cases. The first thing that is apparent is that the respective lines of best fit possess different gradients. This would suggest that a simple deflection test is an insufficient means of calibrating the strain gauges for generalized deflection. This statement may be clarified by explaining that the blade's tip deflection is dependent on the manner in which the blade has been loaded. The deflection-strain data will however be utilised in section 3.4.

Figure 3.7 plots the applied moment exerted on the blade relative to the resulting strain. Unlike Figure 3.6, the single load and multiple load cases possess the same relationship. Figure 3.7 may therefore be used to obtain a reliable calibration equation, which may be used to determine the applied moment experienced by the blade during operation. This calibration equation may be characterised as

$$M_{app} = 0.0258 \varepsilon \quad (3.4)$$

where M_{app} is the applied moment exerted on the fan blade in $\text{N} \cdot \text{m}$ and ε is the corresponding strain experienced by the blade in $\mu\text{m}/\text{m}$.

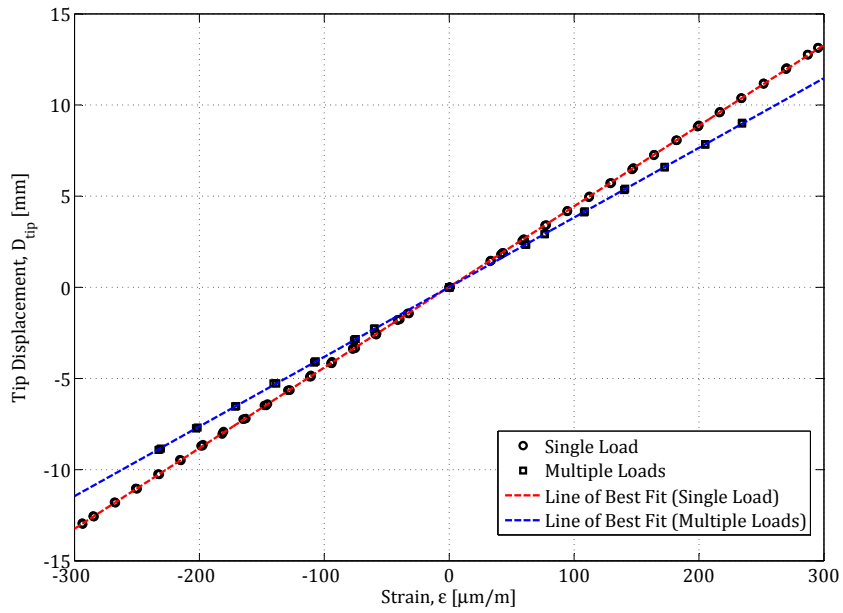


Figure 3.6: Tip displacement, D_{tip} relative to measured strain for both the single load and the multiple load case, with a line of best fit plotted through each data set.

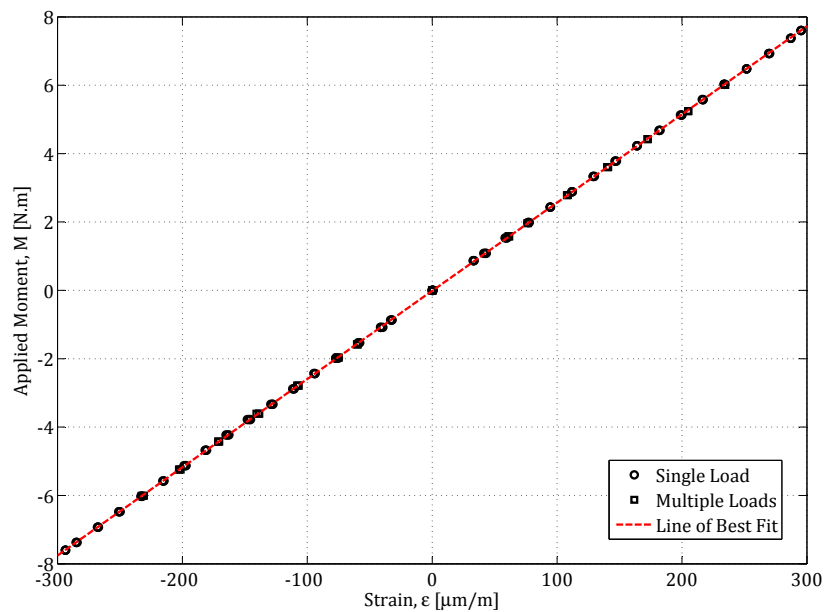


Figure 3.7: Applied Moment, M relative to measured strain for both the single and multiple load case, with a line of best fit plotted through the collective data.

3.4 Determining the Young's Modulus

As previously discussed, the fan blade used during the course of the investigation has been constructed out of Aluminium 5083. Aluminium 5083 is rated as having a Young's Modulus E of between 70 and 80 GPa. The range associated with the rated value of E would result in a significant amount of uncertainty related to analytical solutions, when calculating tip displacement. A process was thus needed to determine the blade's actual value of E .

The deflection of the blade was analysed using a set of 2-dimensional beam equations. The beam equations were constructed using Euler-Bernoulli beam theory, which accounts for lateral translation and rotation. It was decided not to include the transverse shear deformation component, as the beam equations were simply used to analyse the lateral deflection of the blade. Owing to this fact and the static nature of the tests conducted in section 3.3, no value would result from employing Timoshenko beam theory in this analysis. It should be noted that Timoshenko beam theory is typically only employed during vibrational analysis.

Equation 3.5 is known as the structural stiffness equation, where \mathbf{K} is the global stiffness matrix, \mathbf{D} is a vector of the respective nodal degrees of freedom and \mathbf{R} is a vector of the forces acting upon the beam's nodes.

$$[\mathbf{K}] [\mathbf{D}] = [\mathbf{R}] \quad (3.5)$$

The structural stiffness equation accounts for each of the beam segments seen in figure 3.5. Each segment is treated as a separate beam and has its own stiffness matrix (Cook *et al.*, 2002) calculated using

$$[\mathbf{K}] = \begin{bmatrix} \frac{12EI_z}{L^3} & \frac{6EI_z}{L^2} & \frac{-12EI_z}{L^3} & \frac{6EI_z}{L^2} \\ \frac{6EI_z}{L^2} & \frac{4EI_z}{L} & \frac{-6EI_z}{L^2} & \frac{2EI_z}{L} \\ \frac{-12EI_z}{L^3} & \frac{-6EI_z}{L^2} & \frac{12EI_z}{L^3} & \frac{-6EI_z}{L^2} \\ \frac{6EI_z}{L^2} & \frac{2EI_z}{L} & \frac{-6EI_z}{L^2} & \frac{4EI_z}{L} \end{bmatrix} \quad (3.6)$$

The individual stiffness equations pertaining to each beam segment is then combined into a single global stiffness matrix, representing the stiffness of the entire structure. The reduced global stiffness matrix is obtained by eliminating rows and columns pertaining to fixed nodes, which will therefore not experience any deflection. The reduced stiffness matrix for the single load test setup is

$$[\mathbf{K}]_{SL} = \begin{bmatrix} \frac{12EI}{L_{14}^3} + \frac{12EI}{L_{45}^3} & \frac{6EI}{L_{45}^2} - \frac{6EI}{L_{14}^2} & \frac{-12EI}{L_{45}^3} & \frac{6EI}{L_{45}^2} \\ \frac{6EI}{L_{45}^2} - \frac{6EI}{L_{14}^2} & \frac{4EI}{L_{14}} + \frac{4EI}{L_{45}} & \frac{-6EI}{L_{45}^2} & \frac{2EI}{L_{45}} \\ \frac{-12EI}{L_{45}^3} & \frac{-6EI}{L_{45}^2} & \frac{12EI}{L_{45}^3} & \frac{-6EI}{L_{45}^2} \\ \frac{6EI}{L_{45}^2} & \frac{2EI}{L_{45}} & \frac{-6EI}{L_{45}^2} & \frac{4EI}{L_{45}} \end{bmatrix} \quad (3.7)$$

Table 3.1: Stiffness matrix constants.

Constant	Value
I	$829.35 \times 10^{-12} \text{ m}^4$
L_{12}	0.132 m
L_{23}	0.17 m
L_{34}	0.185 m
L_{45}	0.085 m

which is used in conjunction with equation 3.5 to obtain the structural stiffness equation for the single load case

$$[\mathbf{K}]_{SL} \{V_4 \ \theta_4 \ V_5 \ \theta_5\}' = \{-P_1 \ 0 \ 0 \ 0\}' \quad (3.8)$$

The reduced stiffness matrix may be obtained in a similar manner for the multiple load case. It should be noted that where the single load case has been reduced to a 6 by 6 matrix, the multiple load stiffness matrix contains more nodes of interest and therefore has been reduced to a 10 by 10 matrix.

$$[\mathbf{K}]_{ML} = \begin{bmatrix} \frac{12EI}{L_3^3} + \frac{12EI}{L_{33}^3} & \frac{6EI}{L_3^2} - \frac{6EI}{L_{33}^2} & -\frac{12EI}{L_3^3} & \frac{6EI}{L_3^2} & 0 & 0 & 0 & 0 & 0 & 0 \\ \frac{6EI}{L_3^2} - \frac{6EI}{L_{33}^2} & \frac{4EI}{L_{12}} + \frac{4EI}{L_{23}} & -\frac{6EI}{L_3^2} & \frac{2EI}{L_3} & 0 & 0 & 0 & 0 & 0 & 0 \\ -\frac{12EI}{L_3^3} & -\frac{6EI}{L_3^2} & \frac{12EI}{L_3^3} + \frac{12EI}{L_{33}^3} & \frac{6EI}{L_3^2} - \frac{6EI}{L_{33}^2} & -\frac{12EI}{L_3^3} & \frac{6EI}{L_3^2} & 0 & 0 & 0 & 0 \\ \frac{6EI}{L_3^2} - \frac{6EI}{L_{33}^2} & \frac{2EI}{L_{23}} & \frac{6EI}{L_3^2} - \frac{6EI}{L_{33}^2} & \frac{4EI}{L_{23}} + \frac{4EI}{L_{34}} & -\frac{6EI}{L_3^2} & \frac{2EI}{L_3} & 0 & 0 & 0 & 0 \\ 0 & 0 & -\frac{12EI}{L_3^3} & -\frac{6EI}{L_3^2} & \frac{12EI}{L_3^3} + \frac{12EI}{L_{33}^3} & \frac{6EI}{L_3^2} - \frac{6EI}{L_{33}^2} & -\frac{12EI}{L_3^3} & \frac{6EI}{L_3^2} & -\frac{12EI}{L_3^3} & \frac{6EI}{L_3^2} \\ 0 & 0 & \frac{6EI}{L_3^2} & \frac{2EI}{L_{34}} & \frac{6EI}{L_3^2} - \frac{6EI}{L_{33}^2} & \frac{4EI}{L_{34}} + \frac{6EI}{L_{45}} & -\frac{6EI}{L_3^2} & \frac{2EI}{L_3} & -\frac{6EI}{L_3^2} & \frac{2EI}{L_3} \\ 0 & 0 & 0 & 0 & -\frac{12EI}{L_3^3} & -\frac{6EI}{L_3^2} & \frac{12EI}{L_3^3} + \frac{12EI}{L_{33}^3} & \frac{6EI}{L_3^2} - \frac{6EI}{L_{33}^2} & -\frac{12EI}{L_3^3} & \frac{6EI}{L_3^2} \\ 0 & 0 & 0 & 0 & \frac{6EI}{L_3^2} & \frac{2EI}{L_{34}} & \frac{6EI}{L_3^2} - \frac{6EI}{L_{33}^2} & \frac{4EI}{L_{34}} + \frac{6EI}{L_{45}} & -\frac{6EI}{L_3^2} & \frac{2EI}{L_3} \\ 0 & 0 & 0 & 0 & -\frac{12EI}{L_3^3} & -\frac{6EI}{L_3^2} & \frac{12EI}{L_3^3} + \frac{12EI}{L_{33}^3} & \frac{6EI}{L_3^2} - \frac{6EI}{L_{33}^2} & -\frac{12EI}{L_3^3} & \frac{6EI}{L_3^2} \\ 0 & 0 & 0 & 0 & \frac{6EI}{L_3^2} & \frac{2EI}{L_{45}} & \frac{6EI}{L_3^2} - \frac{6EI}{L_{33}^2} & \frac{4EI}{L_{45}} + \frac{6EI}{L_{45}} & -\frac{6EI}{L_3^2} & \frac{2EI}{L_3} \end{bmatrix} \quad (3.9)$$

Once more, equation 3.5 is used to obtain the structural stiffness equation

$$[\mathbf{K}]_{ML} \{V_2 \ \theta_2 \ V_3 \ \theta_3 \ V_4 \ \theta_4 \ V_5 \ \theta_5\}' = \{-P_3 \ 0 \ -P_2 \ 0 \ -P_1 \ 0 \ 0 \ 0\}' \quad (3.10)$$

These equations were used to reconstruct the data obtained in section 3.4. The data represented in figures 3.6 and 3.7 have been combined into a single figure, which relates the blade's tip displacement to the applied moment. A relationship which is linear in nature is found, thereby making it possible to construct lines of best fit through the two data sets.

By making use of the above analytical equations, two straight lines have been plotted through the two respective data sets. Both sets of equations contain the same constant values, meaning that the only difference between them is the externally applied forces. Additionally, all of these constants have known values which can be found in table 3.1, where the only unknown value is the Young's Modulus. This makes it a simple matter to obtain the Young's Modulus by varying its value until both straight lines represent the best possible fit through the measured data. Using this method, it was determined that the Young's Modulus of the fan blade in question had a value of 74 GPa. The results of this process can be seen in figure 3.8.

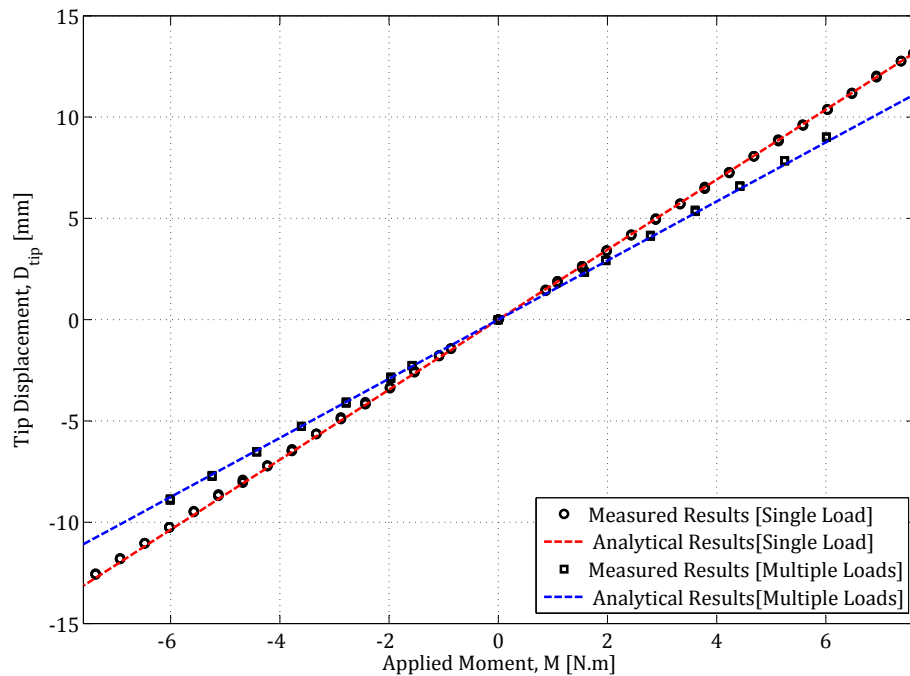


Figure 3.8: Tip Displacement, D_{tip} relative to the applied moment experienced by the blade for both the multiple load and single load cases, with a line of best fit plotted through each data set.

3.5 FRF Analysis

It was decided that before any additional experimentation could be conducted on the fan blade, it would be useful to determine the bending modes that the blade could experience during operation. This was accomplished by means of a Frequency Response Function (FRF) Analysis.

3.5.1 Experimental Setup

The experimental setup was similar to the one seen in figure 3.5. Once again, the blade was inserted into the blade mount jig and orientated using a digital inclinometer. The procedure detailed in section 3.3.1 was employed once more to ensure that the blade was correctly orientated and securely fixed in place. There was no need for the applied loads used in the static deflection test.

Four accelerometers were attached to the blade using wax and were arranged in the fashion seen in figure 3.9. In order to measure higher bending and torsional modes, it would require more accelerometers and it was decided that the acquisition of such information would be of limited value. The reason

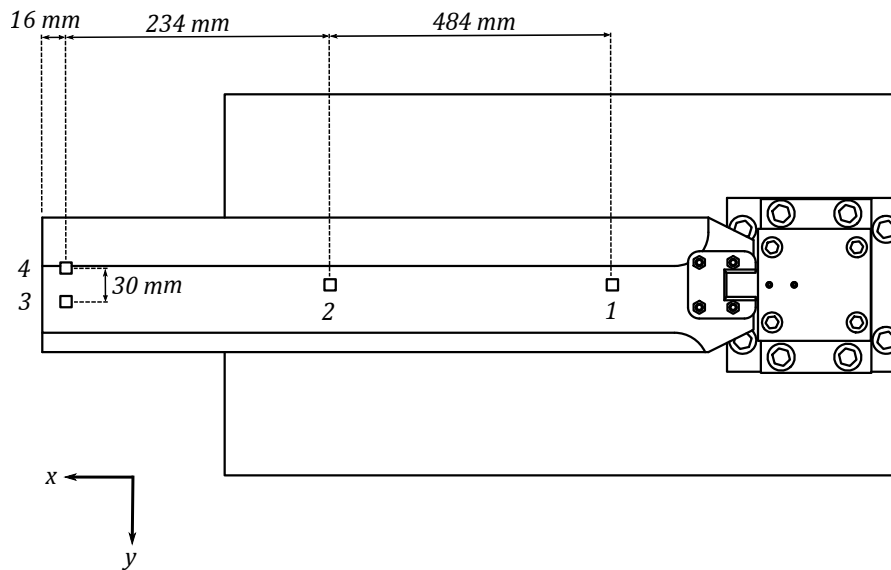


Figure 3.9: FRF analysis setup, detailing the relative placement and designation of each accelerometer.

being that the proposed transmissibility curves which will be constructed and analysed in chapter 5 are expected to lie in a frequency range far lower than the higher bending and torsional modes. It is therefore highly unlikely that these modes would be excited. As an additional point, it should be noted that by placing accelerometers on the blade, the effective mass of the blade is altered. By adding more accelerometers and therefore mass, the results obtained through the analysis become less accurate. This means that the frequencies obtained using the FRF analysis may be accepted as being approximate in nature and should therefore only be used to assist in interpretation of future data analysis.

3.5.2 Experimental Procedure

A frequency response may be characterized as the quantitative measure of the output spectrum of a system or device in response to a stimulus. It is used to characterise the dynamics of the system by measuring the magnitude and phase of the output as a function of frequency relative to the input. In this analysis, an input impulse was applied using a modal hammer, while the output was measured using a series of accelerometers.

The analysis was conducted using the LMS TestLab software, while the signals from both the accelerometers and the modal hammer were captured using a LMS SCADAS data acquisition unit (DAQ). The individual sensitivity values of each accelerometer was obtained from their respective calibration

certificates and entered into TestLab. A similar procedure was then followed for the modal hammer, followed by the relative displacements of the four accelerometers, which were measured in the Cartesian coordinates indicated in figure 3.9.

The final step was to start the analysis in TestLab. The analysis involved striking the tip of the blade with the modal hammer and measuring the resulting response of each of the accelerometers in the z -direction. The software would provide an audible prompt every time the blade needed to be struck, thereby ensuring that sufficient time was allowed between measurements.

3.5.3 Results

The results obtained from the FRF analysis have been plotted in figure 3.10. The acceleration has been scaled to decibel and plotted on the y -axis, while the x -axis plots the frequency in Hz. It should be noted that the x -axis has been limited to include only the data of interest and therefore ranges from 0 to 512 Hz.

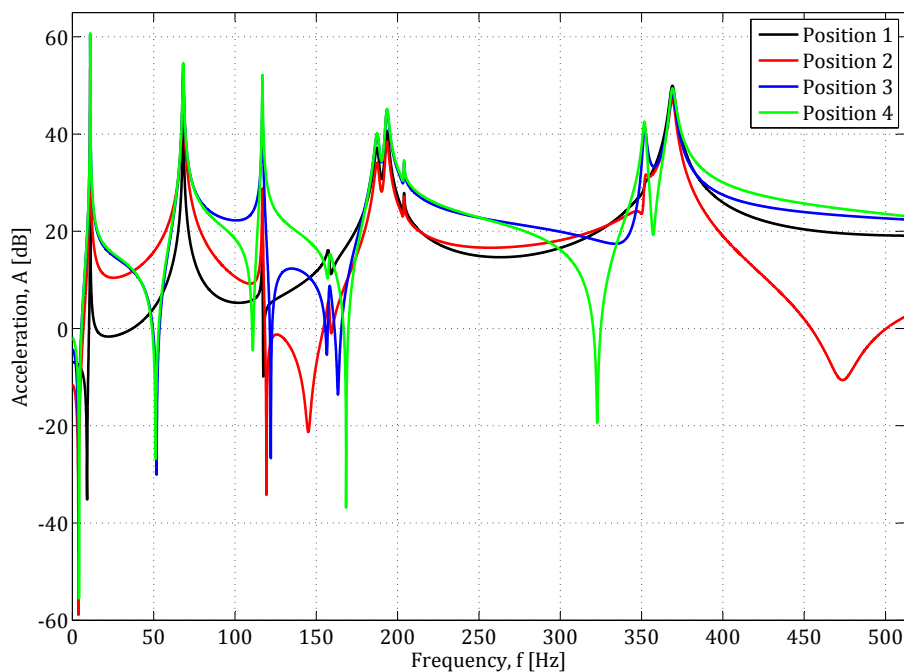


Figure 3.10: Acceleration, A in relation to frequency for all four accelerometers attached to the blade.

Table 3.2: Summary of results obtained during FRF analysis.

Mode	Frequency
1st Bending	10.993 Hz
2nd Bending	68.161 Hz
1st Torsional	116.869 Hz

The peaks seen in figure 3.10 correspond to the blade's various bending and torsional modes. The results were analysed with the assistance of TestLab's built-in modal analysis functionality. The results of which have been summarised in table 3.2. It should be noted that the 1st bending mode had a coherence of higher than 96 %. This indicates a very good correlation between the blade's response and the recreated signals seen in figure 3.10.

The results were verified using a visual inspection. By comparing the peaks pertaining to the individual accelerometers, it becomes possible to determine which bending mode is excited. As an example, when examining the first peak which lies at 10.993 Hz, one should note that all four accelerometers create a peak at this frequency. Furthermore, all four peaks lie in the positive region of the y-axis, which means that they are experiencing acceleration in the same direction. As a result it may be accepted that TestLab's assesment of the first bending mode is correct. The same analysis may be conducted on the first torsional mode. If one examines what happens at 116.869 Hz, it may be noted that the accelerations experienced by the accelerometers located at position 3 and 4 are equal in magnitude, but opposite in direction. These accelerometers are located at the same position relative to the x-axis defined in figure 3.9, but vary along the y-axis. It is therefore clear that they are experiencing torsional bending.

As discussed in section 3.5.1, it would require more accelerometers carefully arranged on the blade in order to identify higher bending modes, with reasonable certainty. This was considered to lie outside the scope of the investigation and has therefore not been performed.

Chapter 4

Vacuum Chamber Experiments

In order to quantify the aerodynamic portion of the total damping experienced by the blade, it was first necessary to determine the structural damping component. It would then be possible to measure the blade's total damping, from which the structural component could be subtracted and the aerodynamic damping component thereby determined. This was accomplished by designing and manufacturing a purpose-built vacuum chamber. The methodology utilized to isolate and determine the blade's structural damping is described in the sections that follow.

4.1 Experimental Setup

4.1.1 Vacuum Chamber

The vacuum chamber utilised during the course of the experimentation was purpose built for the fan blade under investigation and can be seen in figure 4.1. It consists of a 220 mm outer diameter pipe, which is 4 mm thick and 800 mm long. This pipe has had a pair of square flanges welded to each end, which have been laser-cut to fit over the pipe. This welded assembly, along with a pair of laser-cut end-caps and a number of seals, forms the vacuum chamber component of the experimental setup. It should be noted that the pipe in question was selected due to its inner diameter of 212 mm, which was wide enough to house the fan blade under investigation. The thickness of the pipe was not a pivotal factor in the design process, as the chamber was not intended to be a positive pressure vessel. The thickness of the pipe is a direct result of the internal diameter requirement, but it should be noted that a heavy setup was desired from the outset of the design process. It was hypothesised that by increasing the mass of the experimental setup, its resulting inertia would prohibit movement during the free vibration test.

The experimental setup is shown in figure 4.1. It was designed so that the fan blade would be orientated in a perpendicular fashion with regards

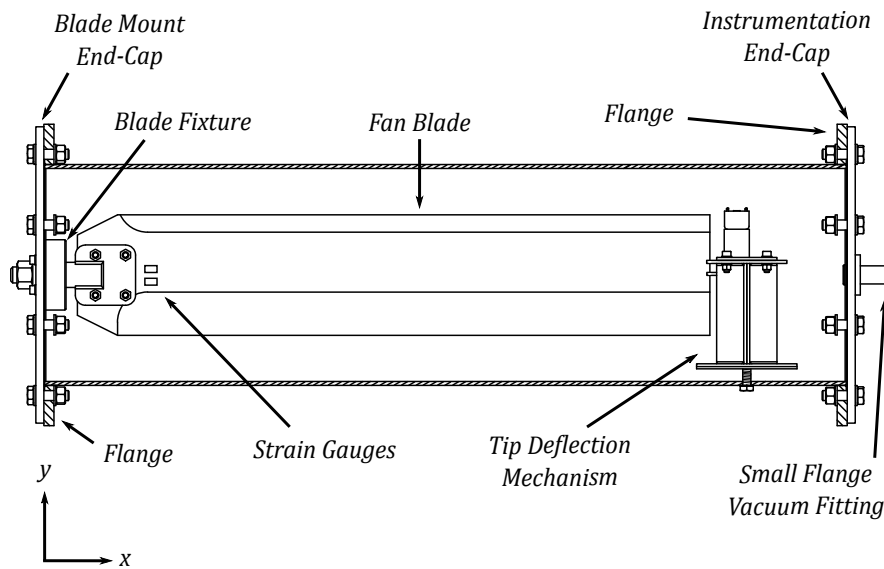


Figure 4.1: Detailed view of the experimental setup, with the walls of the vacuum chamber sectioned.

to the ground plane. The tip deflection mechanism would therefore bring about the blade's free vibration in the z -direction. This was done in order to remove the influence of any gravitational effects acting on the blade during free vibration and was accomplished using a digital inclinometer. The inclinometer was calibrated with regards to the floor on which the setup was resting and the fan blade was secured in the blade mount end-cap.

The threaded portion of the blade's shaft extends through to the outside of the chamber. The blade's retaining nut was tightened from outside the chamber, thereby allowing for easy adjustment of its orientation. Upon examination of figure 4.1, it becomes clear that the fan blade was in contact with the blade fixture, as well as the blade mount end-cap. The fixture serves a number of purposes, the most paramount of which is to provide an airtight seal between the fan blade and the chamber. In addition to the seal, the fixture provided the fan blade with a locating shoulder, thereby ensuring that there was no movement between the fan blade and the end-cap in which it was mounted. The airtight seal between the fan blade and the fixture was provided by means of two separate sealing mechanisms. The first was a 25 mm diameter o-ring, with a thickness of 3 mm, which was situated inside a groove in the blade fixture. The second was a gasket which was located between the fan blade's locating shoulder and the blade fixture. The blade fixture was fastened to the blade mount end-cap by means of four socket head nuts. In order to maintain the desired airtight seal, the fixture possesses a groove in which a 22 mm diameter o-ring is situated. The o-ring has a thickness of 3 mm, forming a seal between

the fixture and the blade mount end-cap. Figure 4.2 depicts an exploded view of the components mentioned in the above discussion.

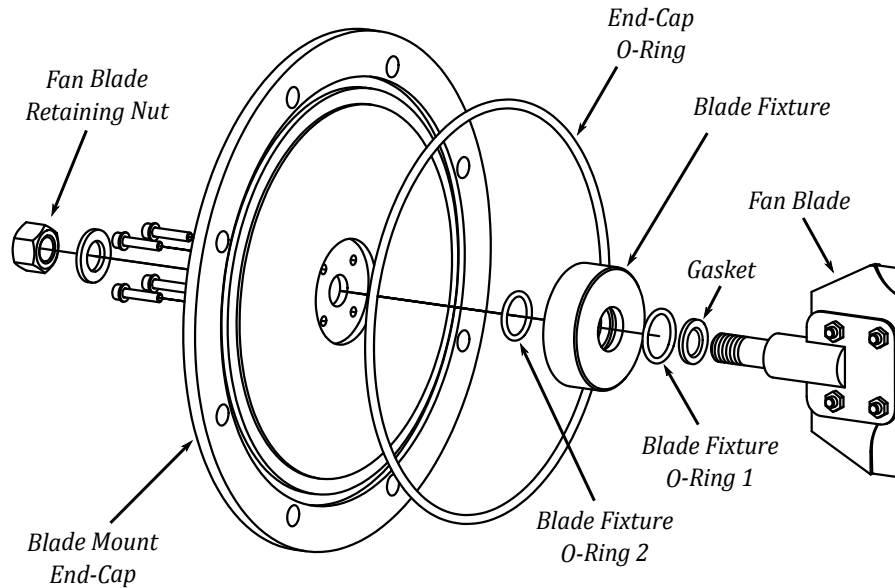


Figure 4.2: Exploded view of the blade mount end-cap assembly, illustrating the placement of the relevant seals and components.

The opposite end of the chamber was sealed using the instrumentation end-cap. This end-cap houses two separate screw-in fittings that are responsible for transmitting electrical signals into and out of the vacuum chamber. The fittings have been manufactured out of polyvinyl chloride (PVC), thereby ensuring that the electrical signals are not conducted by the mild steel end-cap in which they are screwed. The first PVC fitting is responsible for transmitting the electrical signal from the strain gauges to the data acquisition unit (DAQ), while the second provides the tip deflection mechanism's DC motor with a power source. In addition to the PVC fittings, the end-cap plays host to a small flange vacuum fitting.

Both end-caps have had grooves cut into their respective contact surfaces. A 230 mm diameter o-ring, with a thickness of 5 mm, fits in each of these grooves and provides an airtight seal between the end-caps and the flanges. It should be noted that both the flanges and the end-caps have been machined flat in order to ensure an airtight seal. The end-caps further possess a 212 mm diameter protrusion, which extends 2 mm from the flange contact surface. This protrusion is responsible for locating the end-caps, thereby ensuring a good seal when the end-caps are bolted to the flanges. Both the end caps and the flanges have had 8 equi-spaced holes laser-cut, about a pitch circle diameter

of 260 mm. The holes are 12 mm in diameter, thereby allowing the end caps to be secured to the flanges using M10 bolts.

4.1.2 PVC Fittings

As previously mentioned, the instrumentation end-cap contained two PVC screw-in fittings. These fittings were responsible for transmitting electrical signals, while maintaining a vacuum seal.

This was accomplished by drilling four holes in the first fitting and two in the second. The number of holes was determined by the number of individual wires required by the DC motor and the full bridge strain gauge arrangement. Raw copper wire strands were then carefully inserted in each of these holes, with approximately 20 mm extending on either side. An epoxy mixture was then mixed inside a syringe. A needle possessing a 1.5 mm diameter hole was attached to the syringe and the epoxy mixture was inserted into each of the holes. Care was taken to ensure that the holes surrounding the copper wire were entirely filled and that no air could pass through the holes. Once the epoxy had been given sufficient time to dry and it was clear that the copper wire paths were airtight, the relevant wires were soldered to both sides of each fitting and the connections were tested using a multimeter. The exposed wires were then covered using insulation tape.

Similarly to the end-caps, both fittings have had grooves machined into their contact surfaces. A 25 mm diameter o-ring with a thickness of 3 mm was inserted into each of these grooves, before the fittings were screwed into the instrumentation end-cap.

4.1.3 Blade Tip Deflection Mechanism

The tip deflection mechanism depicted in figure 4.1 may be viewed in greater detail in figure 4.3. It was used to bring the fan blade to a state of free vibration, which was accomplished by rotating the cam component, thereby deflecting the blade's tip in the process. Once the blade had been displaced to the maximum degree to which the cam is capable, the diameter of the cam reverted to its minimum diameter. The blade tip was then free of obstruction, allowing it to enter a state of free vibration.

The mechanism is comprised of a 10 mm thick base plate, four pieces of angle-iron forming the side walls and three rectangular pieces, which form the cross plate and the motor mount plate shoulders. With the exception of the base plate, the respective components have all been constructed out of 3 mm mild steel, which have been machined and welded together to obtain the desired form. In addition to machining the base plate to possess flat surfaces, the bottom edges have been further machined at an angle of 30° to the horizontal. This has been done in order to allow the base plate to sit securely inside the chamber. Additionally, the mechanism's base has a fastening groove. This

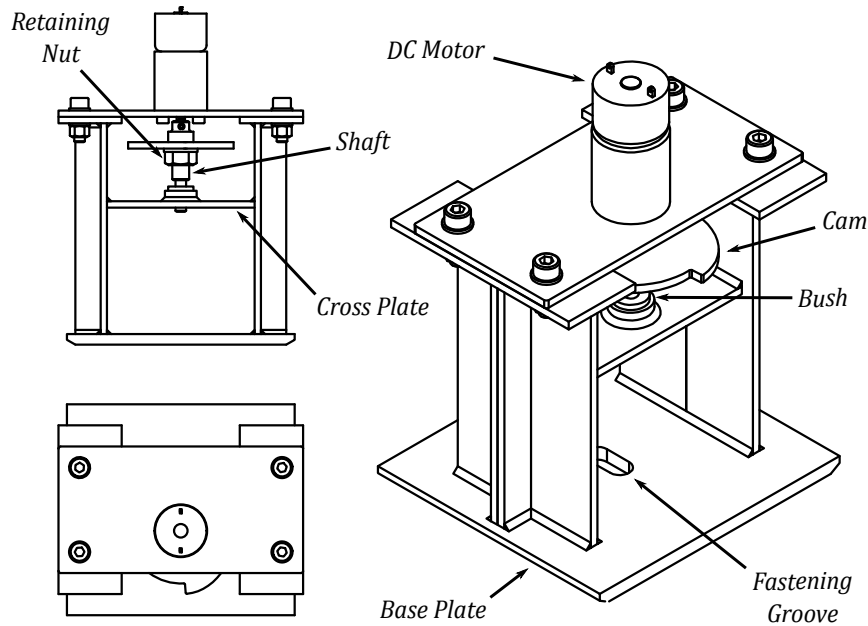


Figure 4.3: Tip deflection mechanism used to impart a state of free vibration on the fan blade.

is to allow for a M8 bolt, which has been welded to the chamber wall, to pass through and subsequently secure the mechanism by means of a retaining nut. The groove allows moderate adjustment of the mechanism position with regards to the fan blade.

In addition to the welded base assembly, the tip deflection mechanism consists of a 3mm thick plate, on which the motor is mounted. This plate has been laser-cut and is attached to the welded base assembly by means of four hexagonal head screws. The screws pass through grooves, which have been laser-cut into the plate, thereby allowing the motor-shaft assembly to be adjusted with regards to its bush. The brass bush in question is subsequently located by means of a hole that has been drilled through the thick section of the cross plate.

Before the motor's mount plate was attached to the welded base assembly, it was necessary to attach the motor. The 6V DC motor in question is rated at $1800 \text{ g} \cdot \text{cm}$ of torque and was fastened to the mount plate using two screws. Next, the shaft was attached to the motor's drive shaft. The shaft has a hole large enough to encompass the motor shaft, which is held in place by means of a location fit and a grub screw, tightened against the flat edge of the motor's shaft. Once secure, the cam was slid onto the square portion of the shaft. It is worth noting that the cam has been laser-cut and that its hole is square to eliminate the possibility of slip during operation. Once correctly orientated, the cam was located against the shaft's shoulder by means of a retaining nut. Finally, the mount plate and its assembly was attached to the welded base

assembly. The other side of the exciter shaft is located in the brass bush and is allowed to rotate owing to a running fit. The setup was operated, while the mount plate was secured, to ensure that it was correctly adjusted and that the cam could turn smoothly.

4.1.4 Data Acquisition

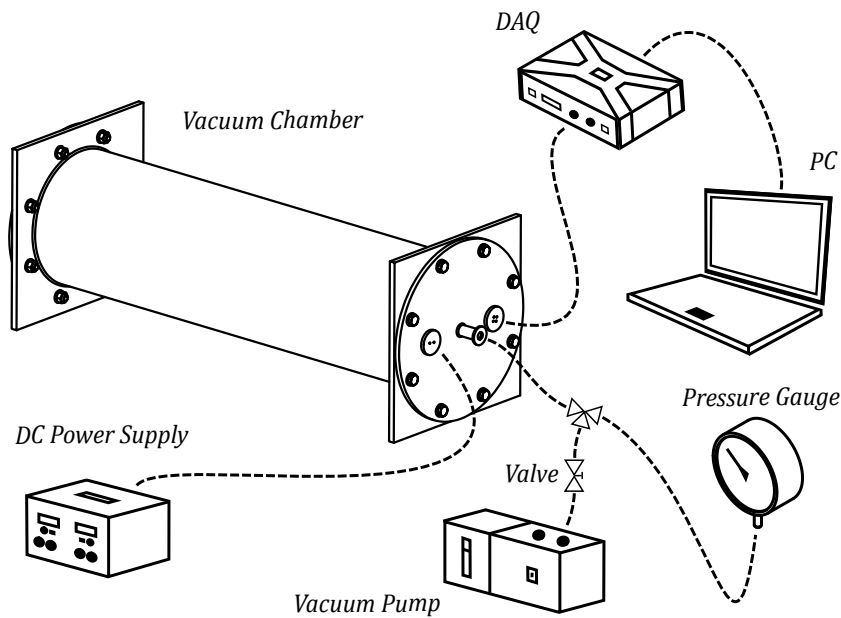


Figure 4.4: Configuration of equipment used during the vacuum chamber experiments.

The preceding sections describe the experimental apparatus associated with the vacuum chamber. The additional equipment used to conduct the experiments may be seen in figure 4.4.

A calibration pressure gauge was used to measure the gauge pressure inside the vacuum chamber. It was connected to a small flange T-piece vacuum fitting. The second branch of the T-piece was connected to the small flange vacuum fitting welded to the instrumentation end-cap. The final branch of the T-piece was connected to a valve, which was connected to the inlet port of the vacuum pump. This arrangement made it possible to measure the gauge pressure inside the chamber, while the vacuum pump was in the process of evacuating air from inside the chamber. The valve could then be closed and the connection leading to the vacuum pump subsequently disconnected.

An HBM Quantum MX410 data acquisition unit was used to record the blade's strain gauge measurements obtained during the experiment, which will be described in section 4.2. Upon deflection of the fan blade, the full bridge

strain gauge signals were transmitted to the DAQ. The DAQ was connected to a laptop and Catman Easy was the software used to record the data. The channel responsible for recording the strain gauge data was configured as a full bridge strain arrangement, with $120\ \Omega$ resistors. As a result, the recorded data had already been converted to $\mu\text{m}/\text{m}$.

4.2 Experimental Procedure

The experimental procedure was repeated three times in order to ensure that the captured data is repeatable. Figure 4.4 gives a detailed breakdown of all the equipment used during the course of the experimentation.

Before the blade could be put into a state of free vibration, the vacuum pump was used to evacuate as much air as possible from the vacuum chamber. The pressure inside the system was measured by means of a calibration dial gauge. The calibration gauge is capable of measuring a gauge pressure of up to $-100\ \text{kPa}$, in increments of $0.5\ \text{kPa}$ with an accuracy of $\pm 0.3\ \%$. The lowest gauge pressure that the vacuum pump was able to achieve was $-92.5\ \text{kPa}$. The atmospheric temperature and pressure was recorded and measurements commenced.

In the interest of being as thorough as possible, it was decided to conduct a total of 14 measurements. The reason for recording measurements in intervals was to identify a trend with regards to the vibrational properties of the blade relative to atmospheric pressure. The key area of interest was when the blade was vibrating at conditions approaching vacuum. As a result, the pressure intervals were reduced the closer the measurements were to the lowest achievable gauge pressure. The results of this investigation will be discussed in section 4.3.

Once the system was at the desired gauge pressure of $-92.5\ \text{kPa}$ or marginally lower, the valve was closed and the vacuum pump turned off. The valve was then disconnected from the vacuum pump, after which it was opened slightly. Air was allowed to slowly enter the system until the pressure gauge registered the $-92.5\ \text{kPa}$ desired for the first measurement and the valve was promptly closed. The DC power supply providing the excitation mechanism's motor with the necessary $6\ \text{V}$ was turned on and the data recording was started on the laptop. The motor in question was selected for its high torque to size ratio, as well as its low rotational speed of $11\ \text{rpm}$. This relates to a time of $5.45\ \text{s}$ to make a full revolution, thereby leaving sufficient time to start the data recording before the blade was once more deflected by the cam. Once the blade had been deflected and the cam had overcome the resistance provided by the blade, the DC power supply was turned off, thereby stopping the motor. The low rotational speed of the motor made it possible to turn off the DC power supply, before the blade was once more deflected by the cam. The blade was then free to vibrate and the free response was captured using the DAQ. The

blade was allowed to vibrate for a full minute, after which it was certain that the vibration of the blade had been sufficiently damped.

Care was taken to ensure that no external sources would influence the blade while under free vibration. As previously mentioned, the blade was orientated in a perpendicular fashion with regards to the ground plane. This not only negated the influence of gravity, but also reduced the sensitivity of the system to any potential vibration transmitted through the floor of the building. Once the measurement had been recorded, the valve was opened slightly once more and the pressure adjusted to the next desired gauge pressure. The above process was repeated until a total of 14 measurements were recorded and the entire procedure was repeated for a total of three data sets.

4.3 Results

4.3.1 Blade Free Response

Upon completion of the vacuum chamber experiments, it was possible to plot the blade's recorded strain relative to time. The resulting plots represent the free response of the blade, at various atmospheric conditions. This is true as it has been shown in section 3.3.3 that there is a linear relationship between the strain gauge measurement and the blade's tip displacement. A typical free response curve obtained during the course of the experimentation may be seen in figure 4.5. This particular free response has been filtered using the Kaizer window method as described in detail in appendix A.

The procedure used to analyse the strain gauge data was consistent for all 14 recorded measurements and over all 3 data sets. It was necessary to filter all the data under investigation, after which the respective free response curves could be plotted and analysed. The reason for using the filter was that the recorded data was subject to noise in the form of a 50 Hz signal, which was believed to be due to insufficient grounding of the measurement equipment. The first step in the data analysis was to locate the peak strain values and the corresponding time values. This was done for both the positive and negative peaks, the absolute values of which were plotted on the same axis. The reason behind this step was to ascertain whether the strain gauge channel had correctly been zeroed by the data acquisition software. Any offset between the trend lines drawn through the absolute positive and negative peak values would mean that the free response was effectively vibrating around an offset x-axis. This means that any vibrational properties determined from further data analysis would be subject to a loss in accuracy.

After confirming that the free response data had been correctly zeroed, the next step was to determine the period (T). The period is simply the time taken to complete one cycle of vibration and was calculated using the start and end times of a complete sine wave. In order to accomplish this, it was necessary to

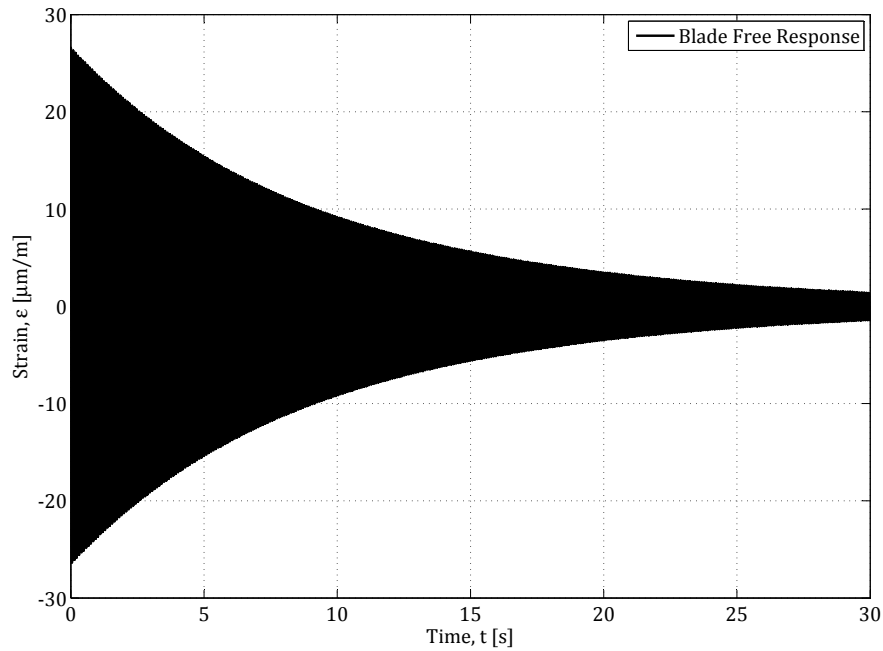


Figure 4.5: Blade free response measured at a gauge pressure of -90 kPa.

first locate the data points situated directly above and below the x-axis. The reason for this becomes clear when one considers that the sampling frequency was 1200 Hz. The discrete nature of the sampling frequency means that the captured data points near the x-axis do not necessarily have strain values equal to zero. In order to determine the times at which the response crosses the x-axis, it is necessary to interpolate the data points directly above and below the x-axis. The measured data points and the resulting interpolated points may be seen in figure 4.6. These new time values were then used to calculate T using

$$T = \frac{\sum_{n=1}^{N-1} (t_{n+1} - t_n)}{N - 1} \quad (4.1)$$

where N is the total number of interpolation points. It should be noted that the response peaks were not used to determine the period. Once again, this is due to the discrete nature of the recorded measurements, which renders it impossible to ensure that the peak values used to calculate the period are in fact the true peaks values.

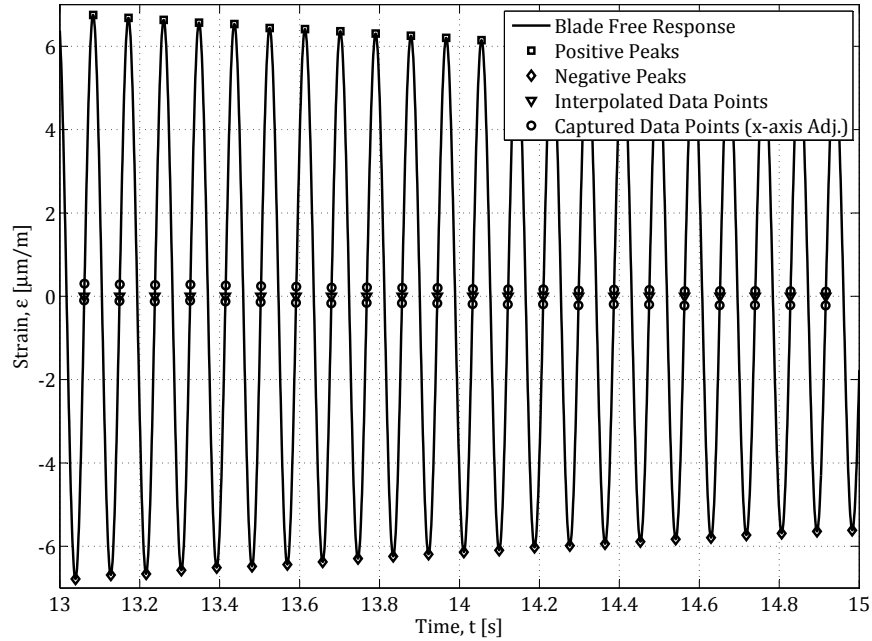


Figure 4.6: Detailed view of figure 4.5 taken 15 s from the start of free vibration and examined over a range of 2 s.

4.3.2 Damped Frequency

The periods which were calculated in section 4.3.1 were used to determine the damped frequency (f_d) experienced by the blade during free response. This was done for each of the 14 measurements performed during all three data sets. The results have been plotted in figure 4.7.

The first thing that may be noted is that the relationship between the damped frequency and the gauge pressure is linear in nature. All measurements were taken at a constant atmospheric pressure of 101.5 kPa. It may therefore be concluded that the damped frequency is directly proportional to the atmospheric pressure in which it is determined. This relationship may be expressed as

$$f_d = -0.502 \times 10^{-6} P_{atm} + 11.3255 \quad (4.2)$$

where P_{atm} is the atmospheric pressure in which the blade is operating. It should further be noted that the temperature was held constant over the course of the experimentation. This suggests that the damped frequency is more appropriately defined as being dependent on the air density.

The reduction of damped frequency relative to an increase in air density may be explained by the added mass effect of air, which has been described in chapter 2. The added mass due to the presence of a fluid is proportional to

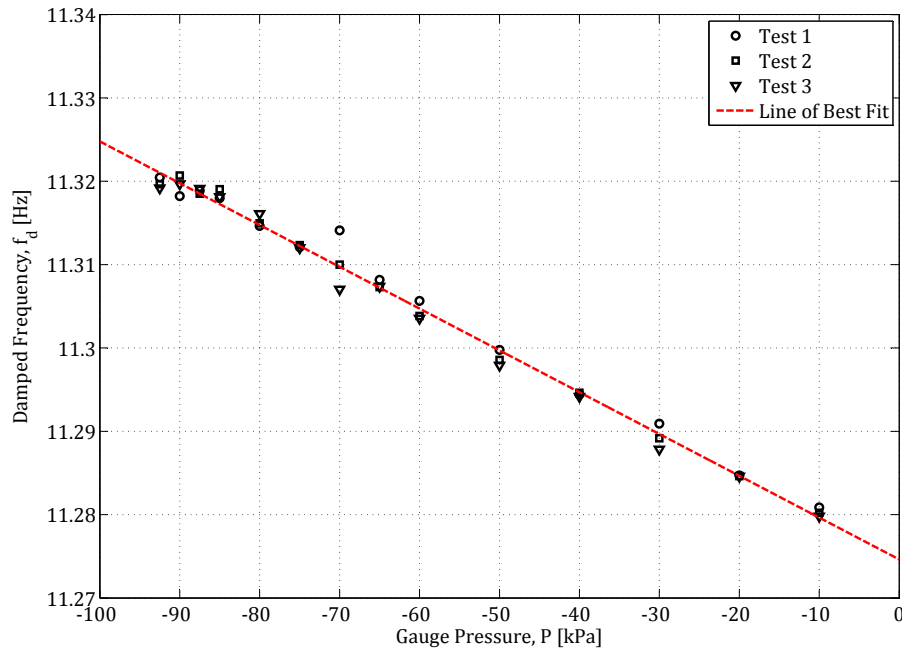


Figure 4.7: Damped frequency, f_d in relation to gauge pressure for three tests, with a line of best fit plotted through all resulting points.

the density of said fluid, while the blade's natural frequency is dependent on its mass. The natural frequency, along with the damping ratio of an object determines the object's damped frequency. The blade is expected to have a small damping ratio and as a result, the damped frequency is expected to become smaller with an increase in density. At this point in the discussion, the damping ratio is unknown, so this effect will be examined in greater detail later in the chapter.

4.3.3 Logarithmic Decrement and Damping Ratio

The logarithmic decrement of the blade's free vibration was analysed, in order to determine the blade's damping ratio (ζ). By taking the peak values which were determined in section 4.3.1 and converting them to the log scale, it was possible to plot a first order line of best fit through the data. An example of the resulting plot can be seen in figure 4.8.

It should be noted that the line of best fit was determined between the time interval 10 to 20 s. This was done as the data appeared to be linear in nature, with a slight deviation in linearity occurring consistently at the beginning of the recorded measurements. This was true for all 14 measurements, over all three data sets. It was noted that the deviation became progressively less

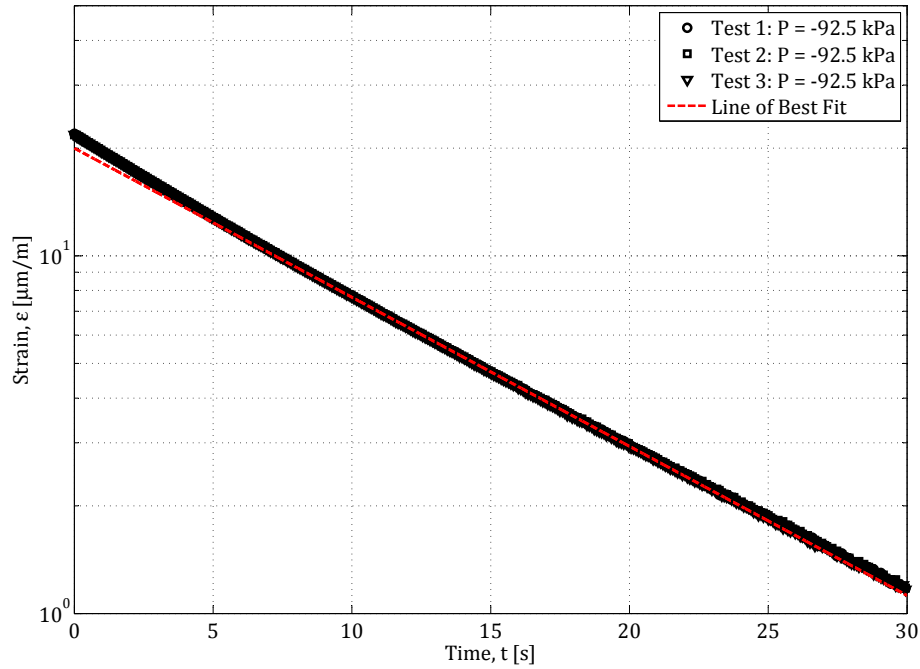


Figure 4.8: Positive peak strain values plotted on a semi-log scale relative to time, with a line of best fit plotted through the combined data sets.

pronounced as the pressure inside the chamber was reduced. This suggests that the non-linearity is due to the presence of air, an assumption which is supported by the research discussed in chapter 2. This change is illustrated in figure 4.9.

It has been shown that the influence of a fluid on a vibrating object is proportional to the fluid's density, as well as the squared velocity of the vibrating object. This offers some insight as to why the tests conducted at higher atmospheric pressures were subjected to larger initial deviations. As previously mentioned, the temperature was constant over the course of the experiments. It may therefore be concluded that the air density inside the chamber increased, as the measured pressure approached atmospheric conditions.

In addition to the air density, the pronounced initial deviation is believed to be as a result of the blade's velocity. Section B.1 of appendix B serves to illustrate this point. The blade's average velocity is dependent on the product of its tip displacement and natural frequency. This is logical as the damped frequency (f_d) of the blade was found to remain constant, while the chamber was at a fixed pressure. The time taken for the blade's tip to move from its maximum positive displacement to its maximum negative displacement is therefore constant, while the distance travelled is reduced every cycle. Simply

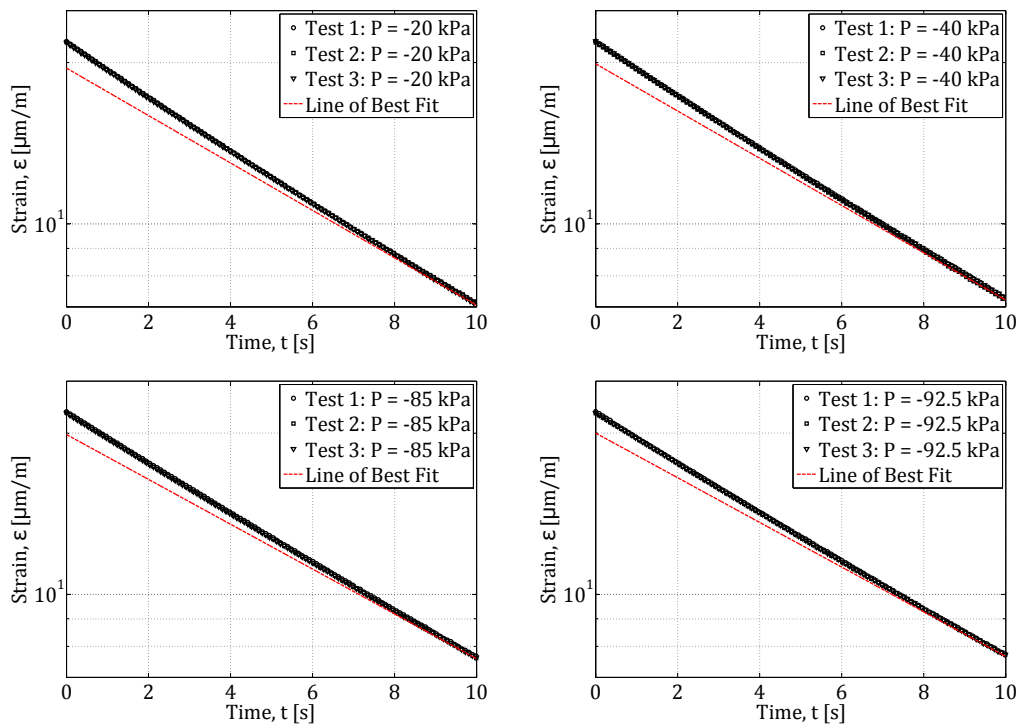


Figure 4.9: Series of plots illustrating the increasing linearity of the blades free vibration, during the first few seconds of recorded data.

put, the velocity of the blade is greatest at the start of free vibration and its influence is reduced as the amplitude of the tip deflection decreases. It should also be noted that the deviation appears to be second order in nature, further emphasising that the interaction of air with the blade is proportional to its velocity squared. The small value for the deflection imparted on the blade by the tip deflection mechanism was selected for this very reason.

Figure 4.10 offers a more detailed look at figure 4.8. It becomes clear that the line of best fit offers a clear representation of the linear logarithmic trend exhibited by the peaks. It also shows that there is a good correlation between the successive experiments, which indicates that there is repeatability of results.

As previously mentioned, the data appears to become increasingly linear in the semi-log scale as the chamber's pressure is lowered and the air density is reduced. This suggests that the aluminium blade is viscous in nature. It is therefore possible to determine the logarithmic decrement using

$$\delta = \ln \frac{x(t)}{x(t + T)} \quad (4.3)$$

and the damping ratio using

$$\zeta = \frac{\delta}{\sqrt{4\pi^2 + \delta^2}} \quad (4.4)$$

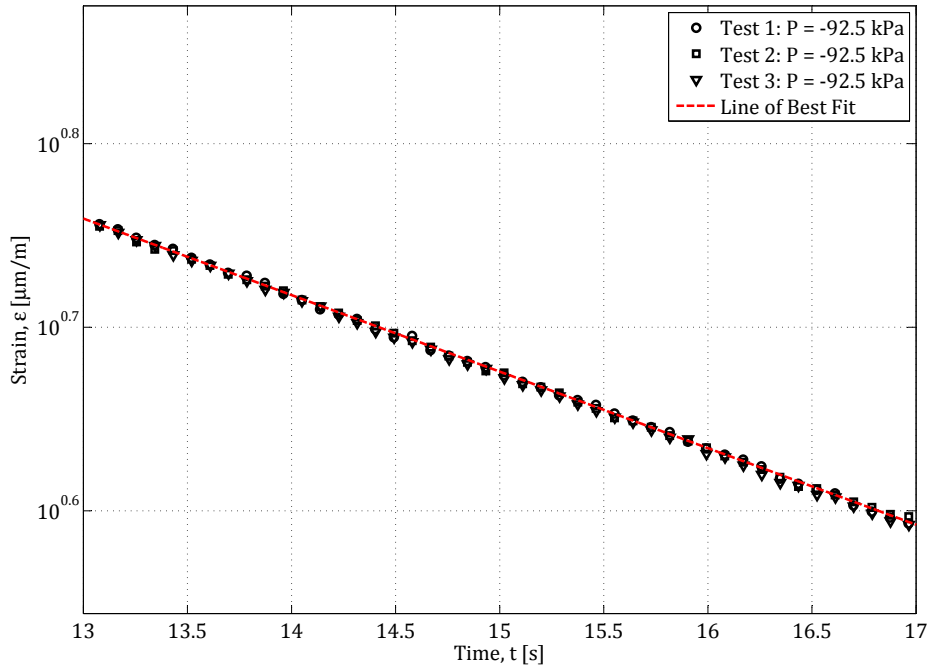


Figure 4.10: Detailed view of figure 4.8 taken 13s from the start of free vibration and examined over range of 4s.

A 1st order line of best fit was determined for the peak strain values plotted on a semi-log scale, as seen in the above figures. These lines of best fit were created using the values of T determined in section 4.3.2. It was therefore a simple matter to calculate δ for each of the experiments, using equation 4.3. The results can be seen in figure 4.11.

As the values of δ have been determined, it was possible to calculate the values of ζ using equation 4.4, the results of which may also be seen in figure 4.11. The values of ζ conform to the trend exhibited by that of δ . The reason for this becomes clear when one examines equation 4.4 and recalls that the values for δ are very small. It may be said that $\delta \ll 4\pi^2$, effectively making ζ proportional to 2π . As was the case with f_d , ζ exhibits a linear relationship with regards to the pressure in which it was determined. This relationship may be expressed as

$$\zeta = 1.3247 \times 10^{-9} P_{atm} + 1.3333 \times 10^{-3} \quad (4.5)$$

4.3.4 Vibrational Properties at Vacuum

The vacuum chamber experimentation took place at a constant atmospheric pressure of 101 500 Pa. By substituting a pressure of 0 Pa into equations 4.2

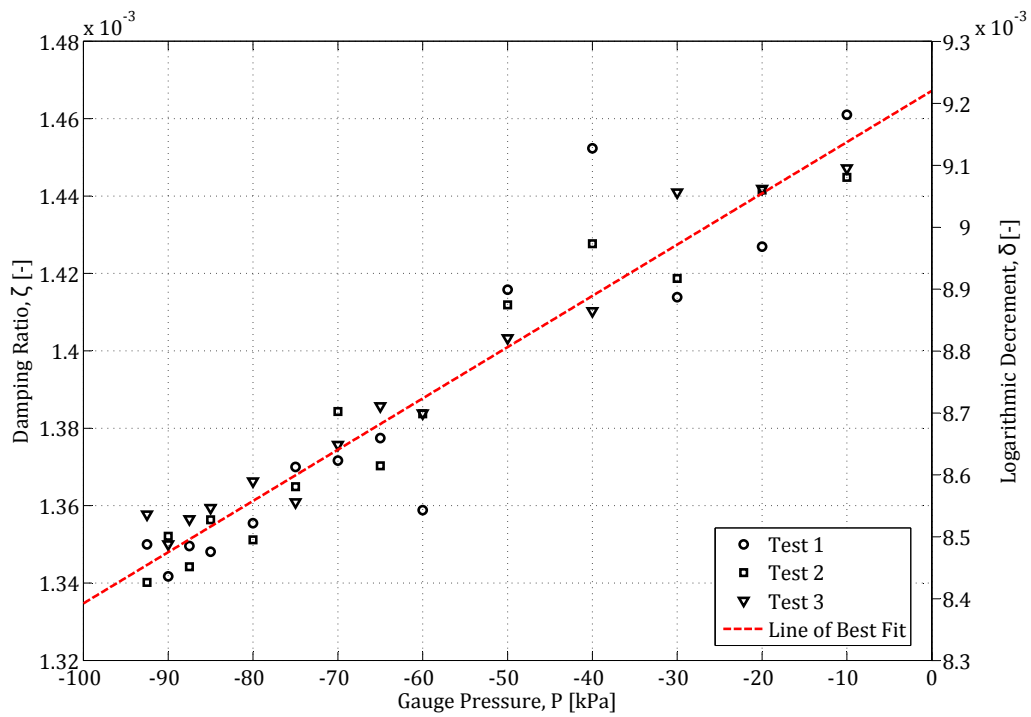


Figure 4.11: Combined plot depicting logarithmic decrement, δ and damping ratio, ζ relative to gauge pressure.

and 4.5, the damped frequency and the damping ratio of the blade may be determined.

The vibrational properties of the blade at vacuum describe the viscous material properties of the blade, absent of any outside interference. These properties may then in turn be used to calculate the natural frequency of the blade using

$$f_n = \frac{f_d}{\sqrt{1 - \zeta^2}} \quad (4.6)$$

By calculating the natural frequency in this manner, the true natural frequency of the blade is known. Any deviation from this value may be attributed to external stimuli influencing the vibrational properties of the blade. The results of the vacuum chamber experiments have been summarised in table 4.1.

Table 4.1: Summary of the fan blade's vibrational properties.

Vibrational Property	Value at Vacuum
f_d	11.3255 Hz
ζ	1.3333×10^{-3}
f_n	11.3255 Hz

Chapter 5

Wind Tunnel Experiments

Since the structural damping of the fan blade has been determined, the aerodynamic damping may be investigated with regards to the total damping experienced by the blade. The total damping was measured while the blade was subjected to a displacement base excitation. This was done as it was believed that the free vibration method employed in chapter 4 would not provide sufficient measurement time, as the anticipated aerodynamic damping would increase the rate of logarithmic decay. The investigation was conducted in a wind tunnel, with the blade's setting angle and the airflow velocity serving as variable parameters. All relevant information pertaining to the wind tunnel investigation may be found in the sections that follow.

5.1 The Wind Tunnel

The experiments discussed in this section were conducted in the large wind tunnel facility located in Stellenbosch University's Mechanical and Mechatronic Engineering Department. The test section of the wind tunnel possesses a length of 1.9 m, a width of 1.425 m and a height of 1 m. The height was of particular importance as it would have to provide sufficient space for the axial flow fan blade, as well as any additional experimental apparatus.

The facility is capable of reaching an airflow velocity of 100 m/s and may be categorized as a induced draft wind tunnel. The axial flow fan, which drives the air flow, is situated downstream of the test section, at the exit of the flow path. This means that the wind tunnel test section will experience a pressure below that of atmospheric.

The layout of the wind tunnel may be seen in figure 5.1. It is comprised of a large inlet area of 13.3 m, followed by a set of aluminium guide vanes. The guide vanes allow the airflow to smoothly make the transition from the inlet area through a 90° corner and in the direction of the test section.

Next, the air passes through a mesh screen, which prevents any unwanted debris from entering the test section and subsequently prevents any damage

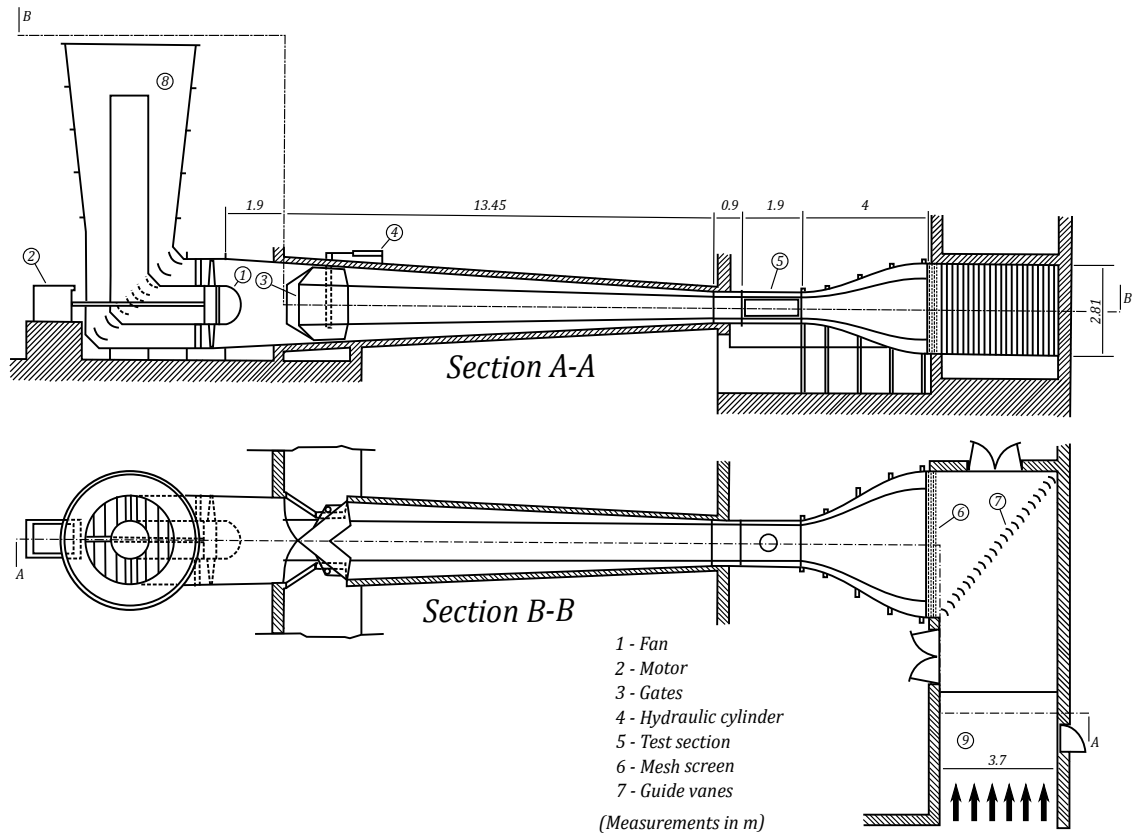


Figure 5.1: Stellenbosch large wind tunnel facility modified from Du Buisson (1988).

to the experimental apparatus under investigation, as well as the axial flow fan driving the airflow. The mesh further serves to ensure that flow is uniform before reaching the test section.

Once through the mesh, the cross-sectional area of the flow is reduced by a factor of 9.4, over a length of 4 m. The uniform airflow then enters the test section.

Once the flow has passed through the test section, it enters a diffuser, which has a total length of 13.45 m. A set of hydraulic gates are situated near the end of the diffuser, before the flow reaches the axial flow fan. The gates serve as an additional means of adjusting the rate of air flow. This method is utilized when the variable speed drive controlling the axial flow fan is unable to achieve the desired airflow velocity through the test section.

5.2 Experimental Setup

5.2.1 Base Excitation Mechanism

The experimental fan blade was mounted on top of a purpose-built mechanical actuation mechanism, seen in figure 5.2. Rotational motion is generated using a 0.37 kW AC motor, which is transmitted to the actuation mechanism by means of a V-belt. The V-belt in turn drives a pulley, which has been securely fastened to the mechanism's drive shaft using a taper-lock. The drive shaft is supported by a rectangular component, attached to the base plate and is located by two deep groove ball bearing units. The drive shaft seen in figure 5.2 has been manufactured out of a single piece of mild steel and includes a crank wheel. As a result, it may be thought of as being akin to a crank shaft.

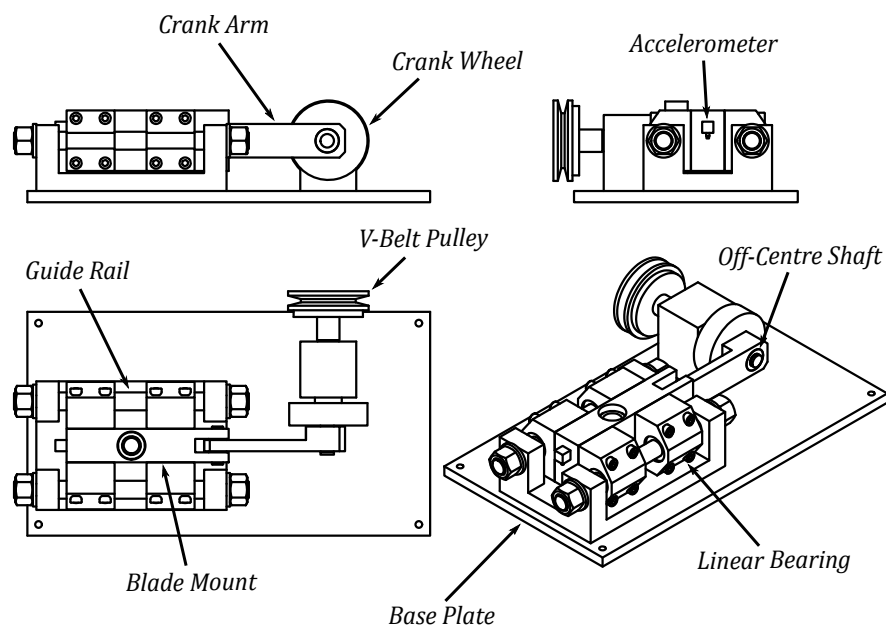


Figure 5.2: Mechanical actuation mechanism used to apply base excitation to the fan blade.

In addition to the crank wheel, an off-centre shaft has been machined out of the same piece of mild steel, thereby forming a single V-belt driven crank-shaft. This particular portion of the shaft has been machined at a 1 mm offset to the rest of the component in question and thereby creates a crank motion upon rotation. This crank motion is transmitted through the crank arm and brings about the horizontal motion of the blade mount. This is a direct result of the movement constraints imposed on the blade mount via the guide rails and linear bearings. The blade mount therefore translates a maximum of 2 mm before changing direction during the base excitation operation.

5.2.2 Wind Tunnel Test Section

The experimental setup located inside the wind tunnel test section can be seen in figure 5.3. The base excitation mechanism was attached to a 750 mm diameter board. The board was then placed in the wind tunnel test section, in the allotted position. The blade's setting angle (γ) could be adjusted by rotating the board, which would be locked in place by a series of bolts.

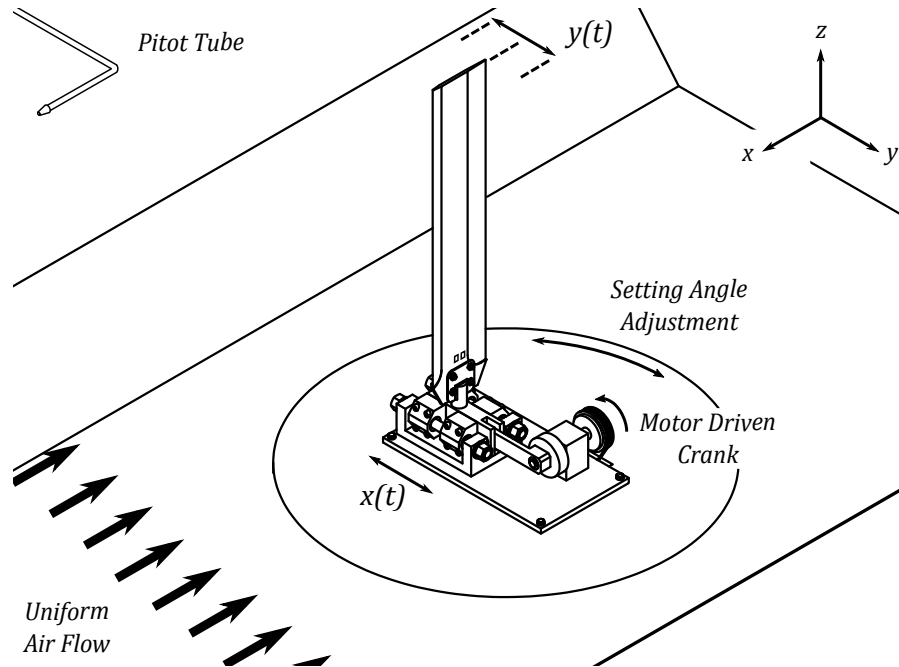


Figure 5.3: Experimental setup, at a setting angle of 0° , located inside the wind tunnel test section.

Once the fan blade was at the desired setting angle and the board was securely bolted to the test section, all panel gaps were sealed using duct tape. The holes through which the strain gauge and accelerometer wires passed, were sealed in a similar fashion. It was not possible to close off the narrow slit through which the V-belt passed and as a result, it was decided to orientate the system in the manner seen in figure 5.3. By positioning the slit downstream, the effect on the experimental setup would be minimal, as any resulting turbulence would be downstream of the fan blade.

A pitot tube was used in conjunction with a mercury barometer and a thermometer to accurately determine the speed of the airflow through the wind tunnel test section. The thermometer was placed in the centre of the mesh screen detailed in figure 5.1, thereby ensuring that the temperature used to calculate the velocity was accurate. The pitot tube was attached to the outside of the wind tunnel test section's side wall and was adjustable with regards to depth of the probe relative to the side wall. The pitot tube was

thus extended far enough into the free stream to ensure that the measured flow did not lie within the boundary layer. The method used to calculate the boundary layer thickness and therefore the positioning of the pitot tube is detailed in section C.3.2 of appendix C.

5.2.3 Data Acquisition

Section 5.2.2 describes the experimental setup located inside the wind tunnel test section. The external components of the experimental setup may be seen in figure 5.4. This external setup was primarily responsible for data acquisition during the experimental procedure, which was conducted using a HBM Quantum MX410 data acquisition unit (DAQ).

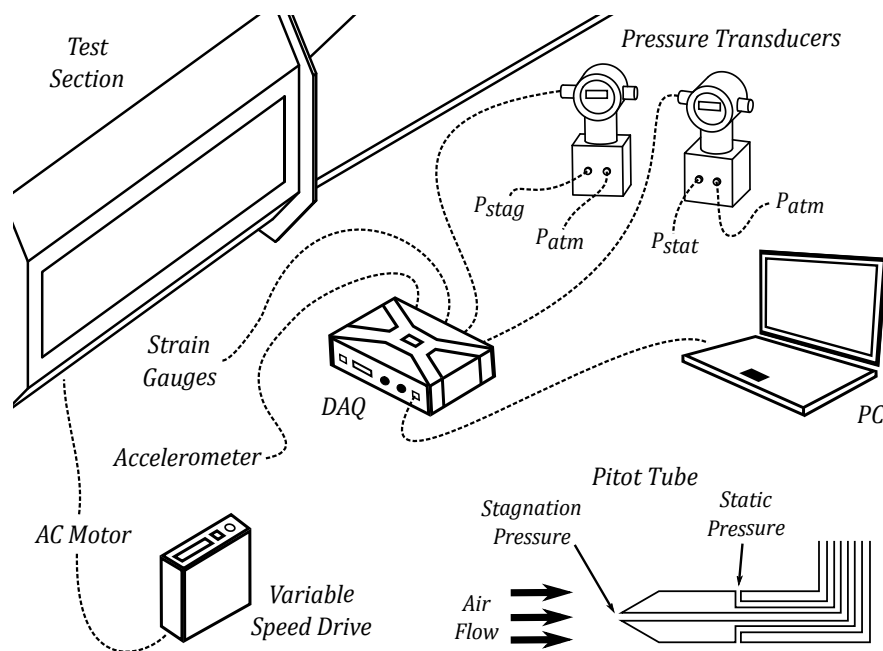


Figure 5.4: External wind tunnel experimental setup, depicting data acquisition layout.

The electrical signals were transmitted to the DAQ via four individual channels and were recorded on a laptop using Catman Easy. Each channel was configured for the specific measurement it would be recording.

Channel 1 was responsible for recording the strain gauge data and was configured as a full bridge arrangement, using $120\ \Omega$ strain gauges with units $\mu\text{m}/\text{m}$.

Channel 2 was configured using the sensitivity provided by the accelerometer's calibration certificate and was used to measure the acceleration experienced by the blade mount, in terms of gravitational acceleration g .

Channels 3 and 4 were used to record the electrical signals from the pressure transducers in terms of voltage (V). The positive terminals of the pressure transducers were connected to the pitot tube, while the negative terminals were open to atmospheric conditions. This meant that the measured pressures were effectively gauge pressures and needed to be used in conjunction with the mercury barometer, mentioned in section 5.2.2, in order to determine the absolute pressures.

5.3 Calibration

5.3.1 Pressure Transducer Calibration using a Betz Micromanometer

The pressure transducers used to determine the the airflow velocity trough the test section, produce an electrical voltage relative to the measured pressure. In order to convert the pressure transducer signals from V to kPa, it was necessary to first calibrate the pressure transducers. This was accomplished using a Betz Micromanometer 5000.

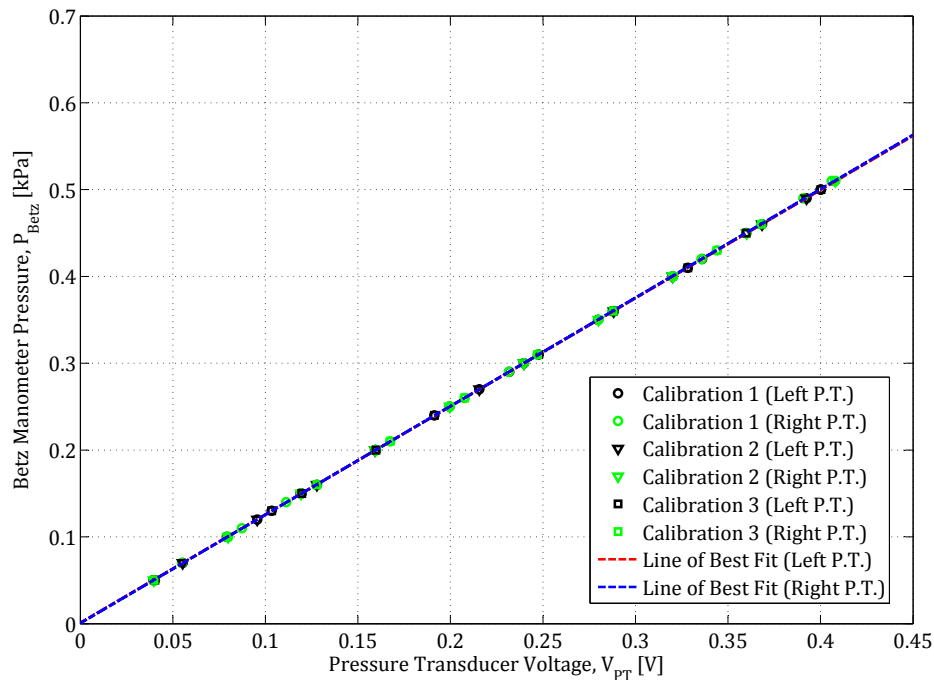


Figure 5.5: Betz manometer pressure, P_{Betz} relative to measured pressure transducer output voltage.

The positive terminals of both the micromanometer and the pressure transducer were connected by means of a T-junction to a single pipe. The pressure transducer in question was then zeroed, before proceeding to adjust the micromanometer's water level to the zero position. A positive pressure was then manually applied to the pipe, thereby exposing both the pressure transducer and the micromanometer to the same pressure. The pipe was then promptly sealed and the pressure was allowed to stabilize. Measurements of both devices were then recorded, before allowing a small portion of air to escape, thereby lowering the pressure. Measurements were then recorded once more and the process repeated until there was a total of 10 measurements. This entire process was then repeated another 2 times, before following the same process for the second pressure transducer. The results of both calibrations can be seen in figure 5.5.

5.3.2 Tip Displacement Calibration using a High Speed Camera

The strain gauge calibration conducted in section 3.3 is a reliable means of determining the applied moment experienced by the blade, from the measured strain. It is however believed that this calibration is not capable of accurately predicting the fan blades tip displacement relative to measured strain, under the proposed base excitation. This is supported by the variation in tip displacement experienced by the blade, during the two loading scenarios investigated in section 3.3. As a result, it became necessary to find another way to calibrate the tip displacement relative to measured strain, for the proposed method of base excitation.

Use of a high speed camera was selected as the additional calibration method. The camera in question was an Olympus i-Speed TR3 and was set up on a tripod upstream of the fan blade, in the wind tunnel test section. The setup can be seen in figure 5.6. It should be noted that at no time during the calibration process was the wind tunnel active, as the camera equipment could not be positioned in any way that would not interfere with the airflow. The camera could not be mounted outside the test section, as it was feared that the resulting refraction from the 10 mm thick perspex would result in a significant loss in accuracy.

Before the calibration process could begin, it was important to ensure that the camera was positioned correctly with regards to the fan blade. A digital inclinometer was used to ensure that the blade was parallel to the test section's mounting surface on which the blade excitation mechanism was attached. Next, both the blade and the camera's positions were measured relative to the side walls of the test section, thereby ensuring that the camera was pointed directly at the blade. Once satisfied that the camera was correctly positioned, a point of reference was needed to determine the blade's tip amplitude. This

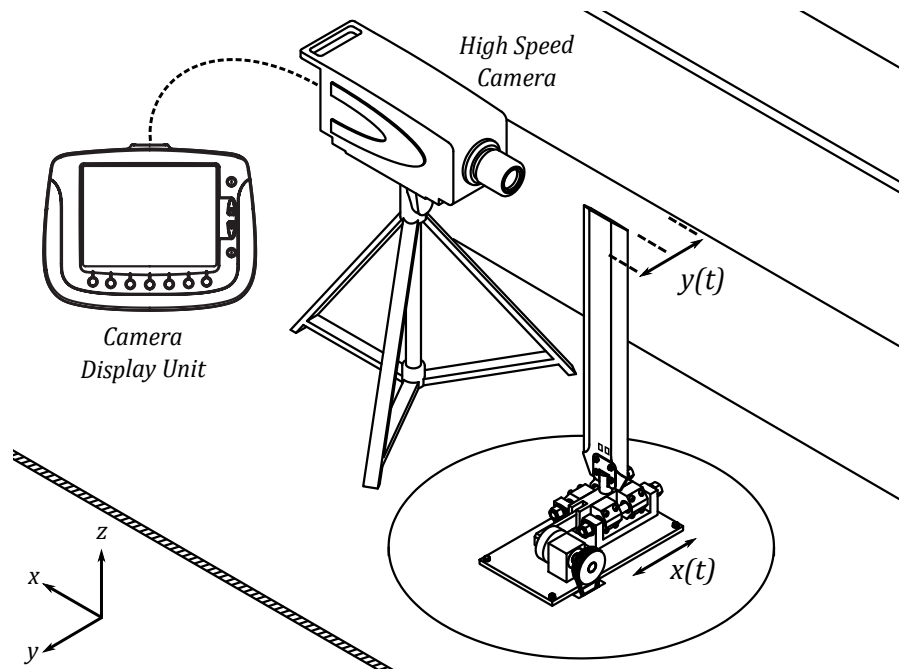


Figure 5.6: High speed camera calibration setup.

was accomplished by fastening a ruler to the blade, as shown in figure 5.7 and taking a short recording.

It should be noted that the recording was taken at a frame rate of 1000 fps and a resolution of 1280×1024 px, which was kept constant throughout the calibration process. The recording was then analysed using the software i-Speed Suite in the fashion shown in figure 5.7. Two points were chosen at a set distance apart and the software was used to determine the conversion factor in terms of pixels per millimetre. In the current configuration, the conversion factor was determined to be 3px/mm (this would need to be recalculated if the camera was moved to a different position). The chosen frame rate has a much higher frequency than the local three phase alternating current electricity supply, which operates at a frequency of 50 Hz. The facility in question is indoors and makes use of fluorescent lighting, which meant that any recording captured by the high speed camera at the specified configuration would only be lit once every 40 frames, as fluorescent lights operate at twice the frequency of the electricity supply. It was thus necessary to make use of LED lighting, which was localized at the blade's leading edge.

Once the conversion factor had been determined, the calibration procedure could begin. The first step was to adjust the base excitation to the desired frequency using the AC motor, which was controlled using a variable speed drive. The DAQ unit was used to record the signals produced by the full bridge strain gauge arrangement and the accelerometer. The accelerometer was used to accurately determine the base excitation frequency, as it was attached to the

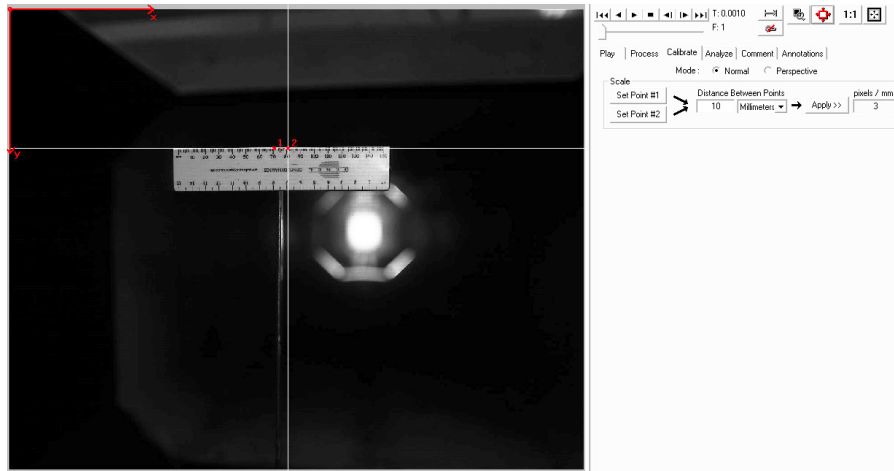


Figure 5.7: Screenshot detailing the process used to determine the pixel to millimetre conversion factor, using a reference image.

front of the blade mount, as depicted in figure 5.2. Once the data acquisition software had begun recording, the camera would be set to begin recording by means of the camera display unit (CDU). The base excitation frequency was varied both below and above the natural frequency of the blade, and a total of 8 measurements were taken, due to the lengthy video capture procedure.

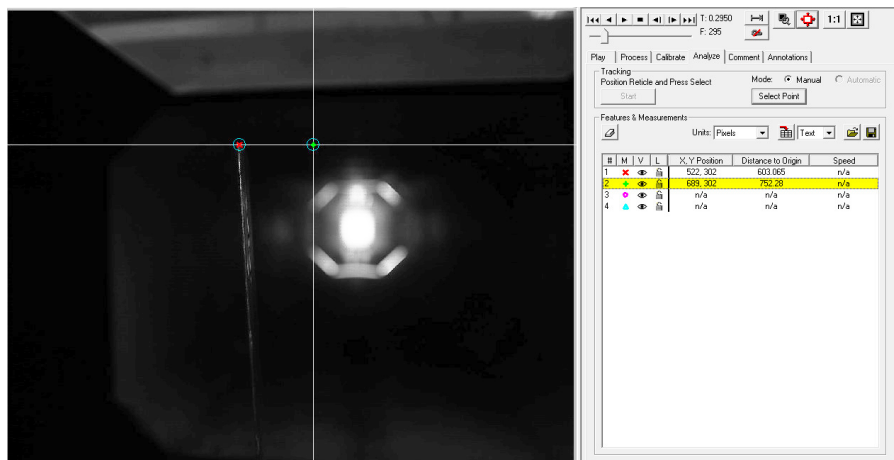


Figure 5.8: Screenshot detailing the process used to determine the blade tip amplitude, in pixels.

Upon completion of the data capturing procedure, the video recordings were examined using the analysis feature in the i-Speed suite. The recording was played back at a speed of 1 fps, which made it possible to clearly see when the fan blade was changing direction. The blade would slow down and linger at the zero velocity point of its motion for a number of frames, before beginning

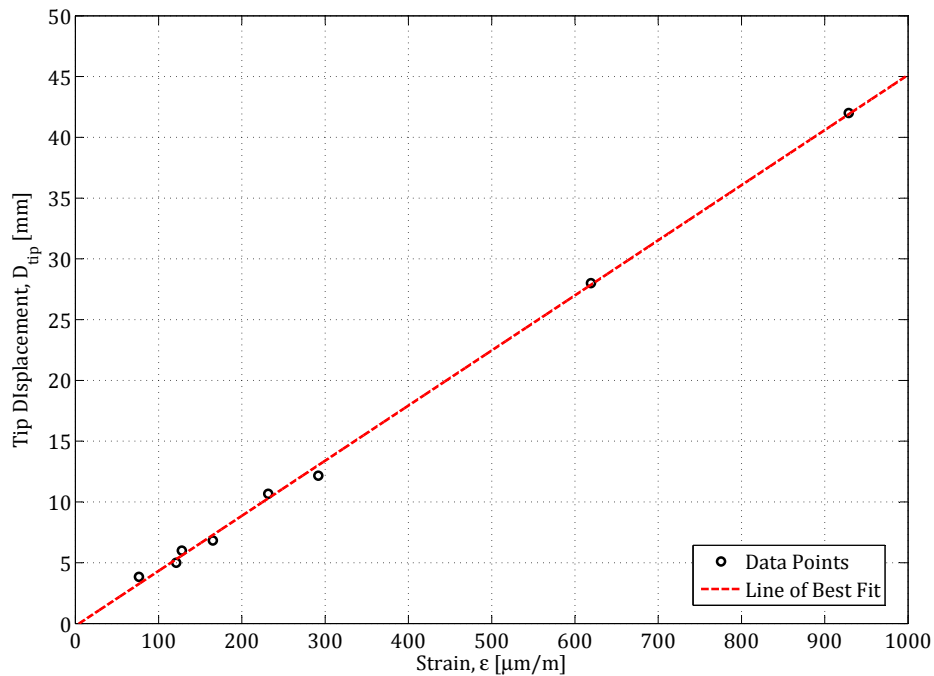


Figure 5.9: Tip displacement, D_{tip} relative to measured strain, determined by halving the calculated amplitude.

to move in the opposite direction. These stopping points were selected and their subsequent coordinates were recorded. As expected, their y-values were identical, confirming that the camera was orientated correctly with regards to the blade. These recorded points were then used to calculate the amplitude in pixels (px) which are indicated using the red and green markers shown in figure 5.8.

In order to relate the measured strain to a base excitation frequency, it was necessary to devise an accurate means of measuring the input base frequency of the excitation mechanism. The acceleration processing procedure will be discussed in detail in section 5.5.1. It should be noted that owing to the nature of the experiment, the blade tip amplitudes would be large when the base excitation frequency approaches the natural frequency of the blade. As a result, it was important to ensure that the base excitation frequencies elected for the high speed camera calibration were sufficiently close to the blade's natural frequency. A large difference between the natural frequency of the blade and the base excitation frequency would result in consistently small tip displacement amplitudes, thereby rendering the calibration ineffective. Additionally, the blade experiences both positive and negative strain during its vibration. The positive and negative strain peak values could therefore be located, after which

the average positive and negative strain value could be determined using the trapezoidal rule. The difference between the magnitudes of the average strain values was then determined, resulting in a strain value which is associated with the blade tip amplitude. Both the strain tip amplitude and the determined blade tip amplitude were halved and plotted in figure 5.9. The result is a linear relationship between the blade tip displacement and the measured strain values.

5.4 Experimental Procedure

5.4.1 Establishing a Baseline

The first step in the wind tunnel experiments was to establish a baseline. This baseline would have to be representative of how the blade would respond under base excitation, without any external factors contributing to the characteristic vibrational behaviour of the blade. This meant that the first test would take place in the wind tunnel test section, without the wind tunnel being active at the time.

An experimental procedure had already been determined in a series of stringent tests conducted prior to the final documented experiments and is shown in section C.2 of appendix C. The purpose of the experiments was to construct a set of motion transmissibility curves, from which all the necessary vibrational characteristics of the blade could be determined. This pre-experimentation process was iterative in nature and made it possible to zero in on the frequencies of interest. As a result, it was decided to take a total of 50 measurements during each experiment. In order to accurately graph the transmissibility curve in question, it was necessary to reduce the base excitation frequency interval the closer one came to the curve's peak. In this way it was ensured that the true peak was captured.

The first step in the experimental procedure was to zero the strain gauges and the accelerometer. This was accomplished by making use of the data acquisition software's functionality. Next, a zero reading was taken, from which it could be confirmed that the channels had indeed been zeroed. The AC motor was activated using the variable speed drive depicted in figure 5.4 and the speed of the motor was adjusted to the frequency necessary for the first measurement. Once satisfied that the mechanism was operating at the desired base excitation frequency, Catman Easy was used to record samples of the strain gauge and accelerometer signals. The measurement was saved to the hard disk of the laptop and the motor was adjusted to the next desired frequency, before repeating the process. This procedure was repeated until a total of 50 measurements had been recorded, ranging from approximately zero to twice the natural frequency of the blade.

5.4.2 Experiments at various Flow Velocities

Once the baseline test had been completed, the next step was to conduct the experimentation at various airflow velocities. The setting angle was held at a constant angle of 0° throughout this process and the desired airflow velocities were 10 m/s, 15 m/s and 20 m/s. The airflow velocity is dependent not only on the rotational speed of the wind tunnel's axial flow fan, but also on the ambient conditions. As a result, it was not possible to achieve the exact desired airflow velocities. This becomes apparent when one examines the manner in which the airflow velocity was calculated, as detailed in section C.3 of appendix C.

The experimental procedure followed during the variable airflow velocity portion of the investigation is identical to the procedure described in section 5.4.1. Before any one of the desired velocities could be investigated however, it was necessary to adjust the airflow using the facility's axial flow fan and hydraulic gates. As previously mentioned, the atmospheric pressure and air temperature were contributing factors towards the airflow velocity. These parameters were therefore recorded before and after every experiment. It should be noted that the facility was run for a few minutes prior to recording the temperature. This was due to the fact that the temperature measurement was taken near the inlet of the test section, while the air drawn into the system originated from outside the building. It was noted that the measured temperature would change, if the system had not been in operation for some time. By running the system prior to recording the temperature, the facility would be given a chance to adjust to the actual temperature experienced during operation and a more accurate flow velocity could be determined.

From these recorded values it was possible to determine the air density and then subsequently the required dynamic pressure, in order to achieve the desired flow velocity. The facility would then be activated and the pressure allowed to stabilize. The flow would then be adjusted by altering the position of the hydraulic gates, until the desired dynamic pressure was measured by the pressure transducers. Once satisfied that the correct flow velocity had been achieved, the axial flow fan was deactivated and the temperature was checked once more in order to ensure that the recorded value had not changed and was in fact correct.

Finally, the experimental procedure could begin. The DAQ channels were zeroed, after which a measurement was taken in order to ascertain whether they had in fact been correctly zeroed. Next, the axial flow fan was activated and sufficient time was allowed for the flow to stabilize. Once it was clear from the pressure transducers that the flow had become stable, a second zero reading was recorded. The reason for this measurement will become clear when analysing the results. The measurement procedure detailed in section 5.4.1 was followed, resulting in a total of 50 recorded measurements, for each airflow velocity investigated. Once the investigation of a desired velocity had been completed, the variable speed drive was used to adjust the axial flow fan, to

what was approximately the next desired airflow velocity. The hydraulic gates were used to zero in on the desired velocity and the procedure was repeated. There were three airflow velocities which were to be investigated and as a result, a total of three data sets were recorded for each experimental setup.

5.4.3 Experiments at various Setting Angles

The third and final component of the experimental investigation was to repeat the procedure described in section 5.4.2 at various setting angles. This procedure was simplified by the fact that the fan blade under investigation is symmetric in profile and would therefore respond identically with regards to a clockwise or anti-clockwise change in angle. This is supported by the static load tests conducted in section 3.3, which showed that the blade's tip deflection relative to measured strain was identical in magnitude and opposite in sign.

The experiments were therefore conducted on the fan blade at the following setting angles; 5°, 6°, 7°, 8° and 9°. It was decided not to investigate the setting angles between the region of 0° and 5°, as it was noted during the course of preliminary experiments that the difference in motion transmissibility between the angles in question were negligible. This will be illustrated in section 5.5. Additionally, it should be noted that it was decided not to investigate setting angles beyond 9°. This decision was made upon close examination of the results obtained from the tests conducted at 9°, where it was noted that the vibrational characteristics of the fan blade were beginning to act in an unpredictable manner.

5.5 Results

5.5.1 Data Processing

The process used to acquire the raw data during the experimental phase of the investigation has been detailed in the preceding sections. This section will discuss the overarching methodology utilized during the course of the data processing stage.

During the course of preliminary testing, it became clear that the experimental setup was subject to a 50 Hz interference. It was further noted that the interference was located outside the frequency range of interest, as determined by the motion transmissibility curves. After extensive investigation, it was concluded that the source of the interference could not be removed. The first step in the data processing stage was therefore to eliminate the interference from the data by making use of the low-pass (LP) filter described in appendix A. It should be noted that no frequencies below 23 Hz were altered, as the base excitation frequency ranged between 0 Hz and 22.64 Hz.

Upon examination of LP filter theory, it becomes clear that the smaller the difference between the selected passband and stopband frequencies, the longer it takes for the filtered data to stabilize. This stabilization time is associated with an overshoot, where the magnitude of the filtered data is momentarily greater than the stabilized filtered data. The explanation of this phenomenon lies outside the scope of the investigation. It is worth noting however, as the examination of this unstable portion of the data would lead to false peak detection. As a result, the next step was to exclude the first few seconds of recorded acceleration and strain gauge data. The filtered data was plotted relative to time, from which it could be seen that the first 0.6s of data should be excluded. As an added precaution, it was decided to exclude the first 2s of data, which formed a relatively small portion of the total time taken to record each individual data measurement.

The resulting data was then analysed using Matlab's "findpeaks" function. The function called for an input describing the minimum peak distance, in addition to the data to be examined. The implication being that if correctly defined, smaller peaks which were in close proximity to a large local peak would be ignored. This minimum distance was calculated by conducting a simple Fast Fourier Transform (FFT) on the data in question and using the resulting frequency in conjunction with the known sampling frequency to determine the approximate time between peaks. This value was then rounded-down, as it represented the minimum peak distance. The frequency associated with the FFT was considered to be approximate, as it has been determined from past investigations, that any frequencies determined in this manner possess insufficient resolution. It should also be noted that the Matlab subroutine written to locate these peaks using "findpeaks" was written prior to the implementation of the LP filter. It was decided to continue using it in the current configuration as the data measured at low base excitation frequencies showed signs of external vibrational influence. As a result the data processing stage needed to be extremely thorough, with every measurement checked to ensure that false peaks were not located and recorded. Once satisfied with the peak detection, an average value was determined for both the positive and negative peaks, which in turn was used to shift the data relative to the x-axis.

As the acceleration and strain gauge data had been shifted relative to the x-axis, it became possible to determine the actual base excitation frequency. This was done by conducting a search on the acceleration data and recording the data points above and below the x-axis. Owing to the high sampling frequency, the y-distance between the points in question could be considered to be small. It was therefore decided to determine the crossing point by means of interpolation. This resulted in the time values associated with a strain gauge value of zero, which was used to calculate the period of successive peaks. These periods were then averaged and the resulting average was inverted to determine the base excitation frequency of the measurement in question.

As the peak values of the strain gauge data had already been determined

and then subsequently adjusted with regards to the x-axis, it was a simple matter to determine the amplitude of the blade tip displacement. This was achieved by calculating the average positive and negative peak strain gauge values, after which the resulting magnitudes were added together. As the strain amplitude was now known, the blade tip displacement calibration data determined in section 5.3.2 was used to convert the amplitude from $\mu\text{m}/\text{m}$ to mm. Finally, the motion transmissibility ratio could be determined by dividing the blade tip amplitude by the base excitation amplitude. The frequency ratio was determined in a similar manner, by dividing the base excitation frequency by the natural frequency of the blade.

5.5.2 Motion Transmissibility Curves

Section 5.2.3 served as an explanation of how the motion transmissibility curves were constructed from the recorded raw data. This section will focus on the analysis of the resulting curves and will discuss any differences noted between experiments conducted at varying setting angles or at different airflow velocities.

It should be noted that each of the motion transmissibility graphs, examined in this section, focus on the complete experiment performed at a specific setting angle, γ . That means that it represents all three of the airflow velocities under investigation, at the value of γ in question. Additionally, each graph further depicts a baseline motion transmissibility curve, as described in section 5.4.1. The first of these curves can be seen in figure 5.10. Figure 5.10 examines the effect of the induced airflow on the fan blade's vibrational response, at various airflow velocities, while γ is kept at a constant value of 0° . The experiments conducted at this γ offer significant insight, as the only external factor influencing the vibrational response of the setup is the induced airflow inside the wind tunnel test section.

The first thing that one notes when examining figure 5.10 is that the motion transmissibility ratio decreases as the airflow velocity is increased, for frequency ratios approaching 1. This is expected, as it is understood that the motion transmissibility ratio is directly affected by the damping experienced by the object under investigation. It can therefore be noted that the total damping experienced by the fan blade is increased as the airflow velocity is increased, an observation which holds true regardless of the value of γ .

It should further be noted that the curves pertaining to different values of γ start and end with the same motion transmissibility ratios, with the change occurring when the base excitation frequency approaches the natural frequency of the fan blade. This fact further illustrates that the change in the respective curves is due to a change in the total damping experienced by the blade and not due to an outside influence, as the curves would exhibit different profiles. As previously stated, the influence of air on the blade is proportional to the squared velocity of the blade. As shown in section B.1 of appendix B,

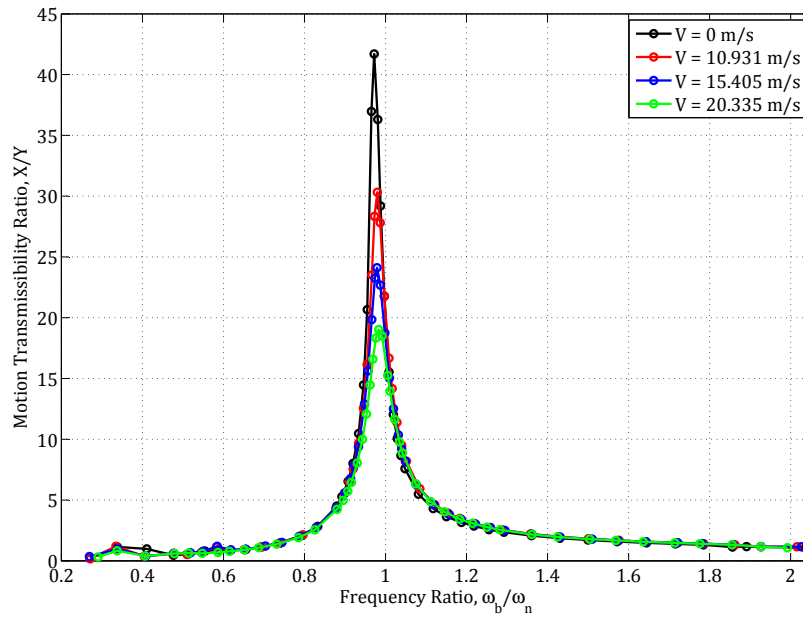


Figure 5.10: Motion transmissibility ratio, X/Y relative to frequency ratio, for fan blade tested at γ of 0° .

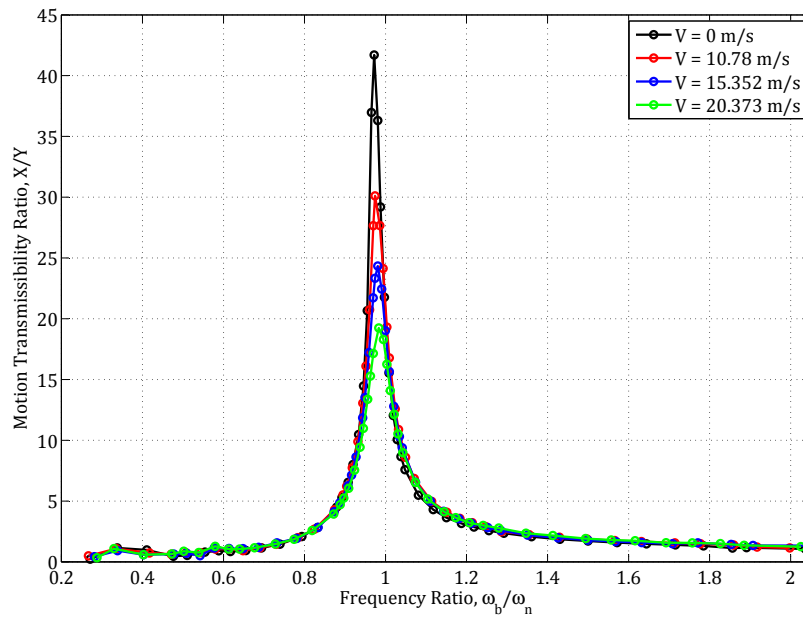


Figure 5.11: Motion transmissibility ratio, X/Y relative to frequency ratio, for fan blade tested at γ of 5° .

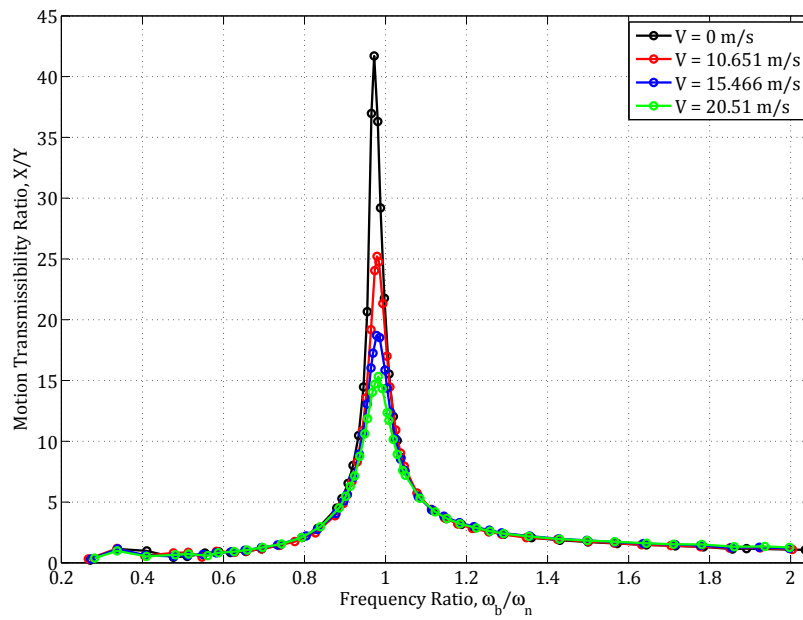


Figure 5.12: Motion transmissibility ratio, X/Y relative to frequency ratio, for fan blade tested at γ of 6° .

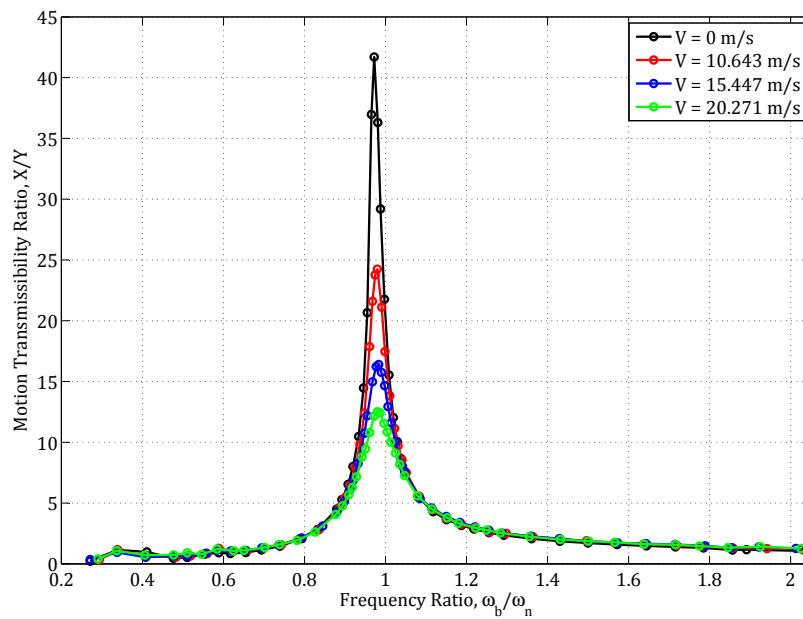


Figure 5.13: Motion transmissibility ratio, X/Y relative to frequency ratio, for fan blade tested at γ of 7° .

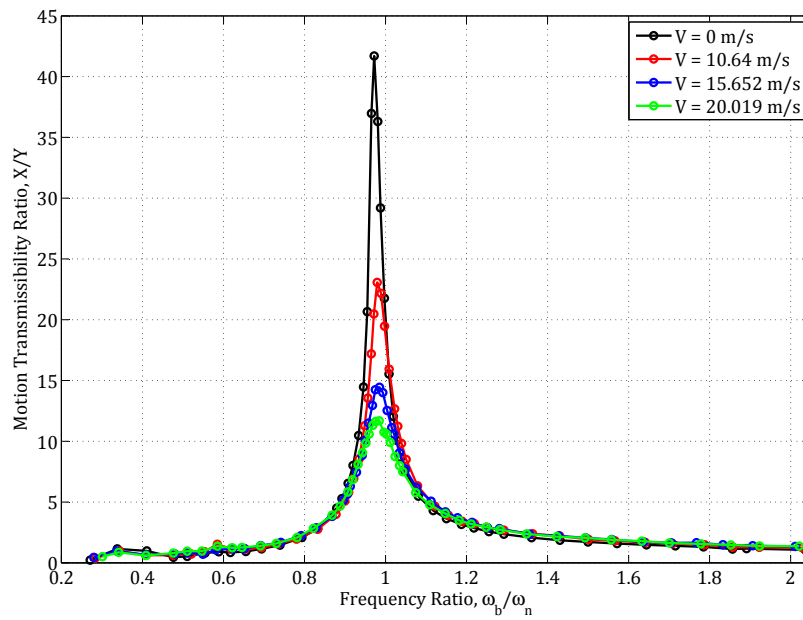


Figure 5.14: Motion transmissibility ratio, X/Y relative to frequency ratio, for fan blade tested at γ of 8° .

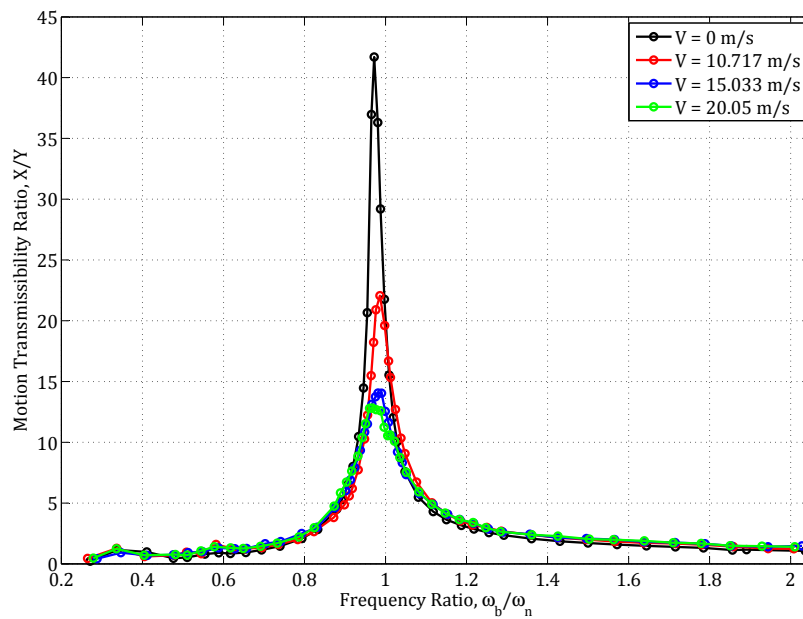


Figure 5.15: Motion transmissibility ratio, X/Y relative to frequency ratio, for fan blade tested at γ of 9° .

the velocity of the blade is proportional to its deflection. Additionally, the air damping component of the total damping experienced by the blade is directly proportional to the amplitude of the blade. These two facts suggest that the further the frequency ratios of the respective curves are from a value of 1, the more similar the transmissibility ratios will be.

Upon close examination of the respective motion transmissibility curves, it becomes apparent that the peaks do not occur at the expected frequency ratio of 1. This phenomenon is consistent regardless of the γ under investigation, with the peak occurring at a frequency ratio of 0.972. The reason behind this shift is explained by the fact that the natural frequency used to calculate the frequency ratio was determined for vacuum conditions. The natural frequency of the blade, while in the presence of air, is smaller than the value determined under vacuum conditions. This is due to the added mass effect that the air has on the blade, as described in section 2.3 of chapter 2. This fact is illustrated by means of a sample calculation in section B.3.1 of appendix B, in which the added mass is calculated for the baseline experiment and subsequently used to determine the adjusted natural frequency (ω'_n) of the blade. The adjusted natural frequency was calculated to be 10.954 Hz, which corresponds to an adjusted frequency ratio (i.e. $r' = \omega'_n/\omega_n$) of 0.967. The difference between the measured frequency ratio and the adjusted frequency ratio corresponds to an error of 0.514 %.

At the lower end of the frequency ratio spectrum, the motion transmissibility curves exhibit what may be described as localized perturbations. These small perturbations result in a spike in the transmissibility ratio, but fortunately are only present at very low base excitation frequencies. As a result, they do not affect the key area of interest, namely the transmissibility peaks, which occur when the frequency ratio approaches 1. As previously discussed, the data was not filtered below 23 Hz and as a result, these perturbations could not be removed. During the experimentation, it was noted that the motor driving the excitation mechanism was subject to movement during operation. This movement was minimized using straps, but the movement could not be eliminated altogether. The motor was noted to be primarily subject to movement at low base excitation frequencies, after which it remained unaffected. The perturbations are therefore believed to be as a result of the harmonic excitation of the motor-strap interaction.

Figure 5.15 examines the experimentation conducted at a γ of 9°. It is interesting to note that the characteristics observed in figures 5.10 to 5.14 do not hold true for this particular experimental setup. This may not be obvious at first glance, but when one examines it in relation to figure 5.14, this observation becomes more clear. The first thing to note is that the green curves, representing the intended airflow velocity of 20 m/s, do not follow the pattern exhibited in the previous figures. Figures 5.10 to 5.14 show that the total damping experienced by the fan blade increases as γ is increased. This is not true for the green curve seen in figure 5.15. The total damping experienced by

the blade at this airflow velocity is actually less than its counterpart seen in figure 5.14. It should also be noted that the motion transmissibility curves have become less predictable at an γ -value of 9° and no longer peak at consistent frequency ratios. It is suspected that the fan blade may be experiencing flow separation, which would account for the unpredictable and inconsistent nature of the vibrational characteristics. It was therefore decided not to investigate values of γ exceeding 9° and it is suggested that a fluid-structure-interaction analysis of the fan blade be conducted in the future, to better understand what may be occurring at high angles of attack.

5.5.3 Examination of the Blade's Damping Ratio

The motion transmissibility curves discussed in section 5.5.2 have been analysed using the single-degree-of-freedom system analysis outlined in appendix D. The resulting total damping ratios have been plotted relative to the relevant airflow velocity and can be seen in figure 5.16.

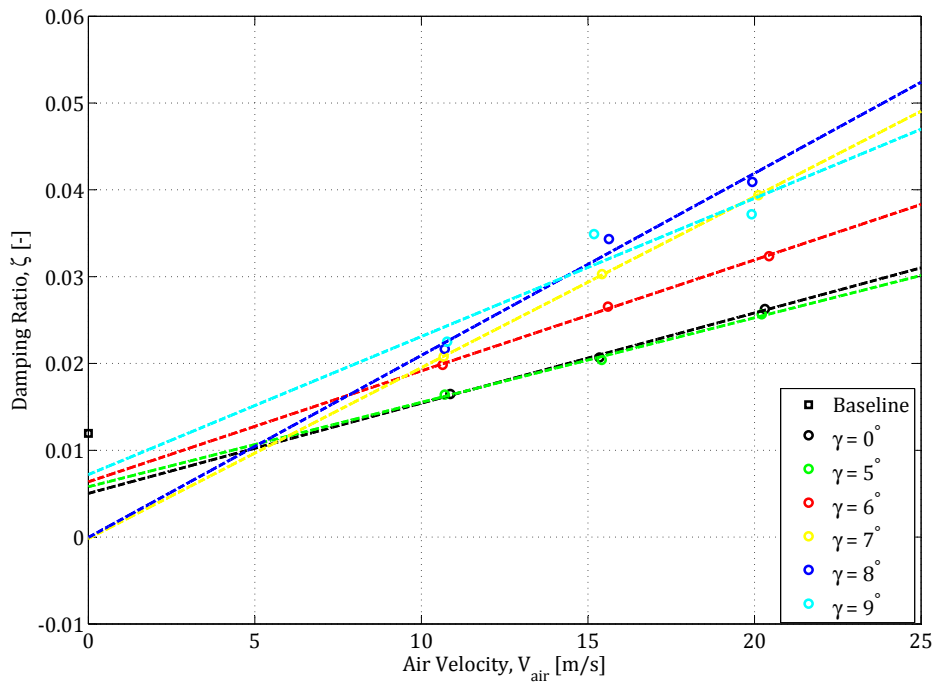


Figure 5.16: Total Damping Ratio, ζ relative to airflow velocity, for the setting angles under investigation, with a line of best fit plotted through each data set.

Figure 5.16 further illustrates the behaviour outlined in section 5.4.3. The total damping experienced by the fan blade increased, as the airflow veloc-

ity in the wind tunnel test section was increased. Additionally, the damping experienced by the fan blade increased as γ was increased. Furthermore, the relationship between the damping ratio and airflow velocity appears to be linear in nature, the only exception occurring when γ is increased beyond 7° . At this point the relationship is approximately linear, with significantly greater error present between the line of best fit and the measured data points. This is further emphasised by the fact that the line of best fit, associated with γ equal to 9° , intersects the line of best fit associated with γ equal to 8° . This is unprecedented as the overall trend suggests that this should not be the case and the line of best fit associated with γ equal to 9° should lie above all the other lines. This is supported by the fact that the two damping ratios determined at the lower airflow velocities are situated above the line of best fit for γ equal to 8° , while the final damping ratio is situated below the line of best fit for γ equal to 7° . As mentioned in section 5.4.3, these inconsistencies are suspected to be due to the presence of flow separation.

It has also been mentioned that the investigation did not include values of γ between 0° and 5° . As discussed, the reason for this omission was due to the relatively small differences noted during preliminary testing. This statement is illustrated in figure 5.16, which shows a relatively insignificant difference between the trend lines constructed for the investigations conducted at values of γ equal to 0° and 5° . This is emphasised by the fact that the differences between investigations conducted at values of γ above 5° are notably greater than the difference between the investigations conducted at 0° and 5° .

The damping ratio calculated for the baseline test was expected to be the point of convergence for the first order trend lines produced in figure 5.16. It should be mentioned that airflow velocities below 10 m/s could not be achieved by the wind tunnel, at the time of investigation. The under prediction of the trend lines could thus not be investigated. From research and the results obtained in chapter 4, it is suspected that the aerodynamic damping component acting on the blade at low velocities is primarily dependent on the squared velocity of the air relative to the blade, making the trend line second order in nature.

The linear nature of the trend lines suggest that the experimentation is repeatable and illustrates that there is a relationship between the airflow velocity and the total damping experienced by the fan blade. This is important, as the nature of the experimentation makes it difficult to show repeatability. The reason for this fact becomes clear when one considers that the vibrational characteristics of the fan blade are directly influenced by the ambient conditions in which it is investigated. With no means of keeping factors such as the atmospheric pressure and temperature constant, figure 5.16 serves as a good indication that the results are repeatable. The three separately conducted experiments form linear trends regardless of the varying ambient conditions, which resulted in different airflow velocities.

5.5.4 Examination of the Blade's Average Displacement

It has been mentioned in section 5.4 that a secondary zero measurement was recorded. This was done after the fan blade had been exposed to the induced airflow in the test section, but before the base excitation was applied to the experimental setup. The reason for this measurement was to compare the average tip deflection, experienced by the fan blade during base excitation, to the tip deflection brought about by the airflow alone.

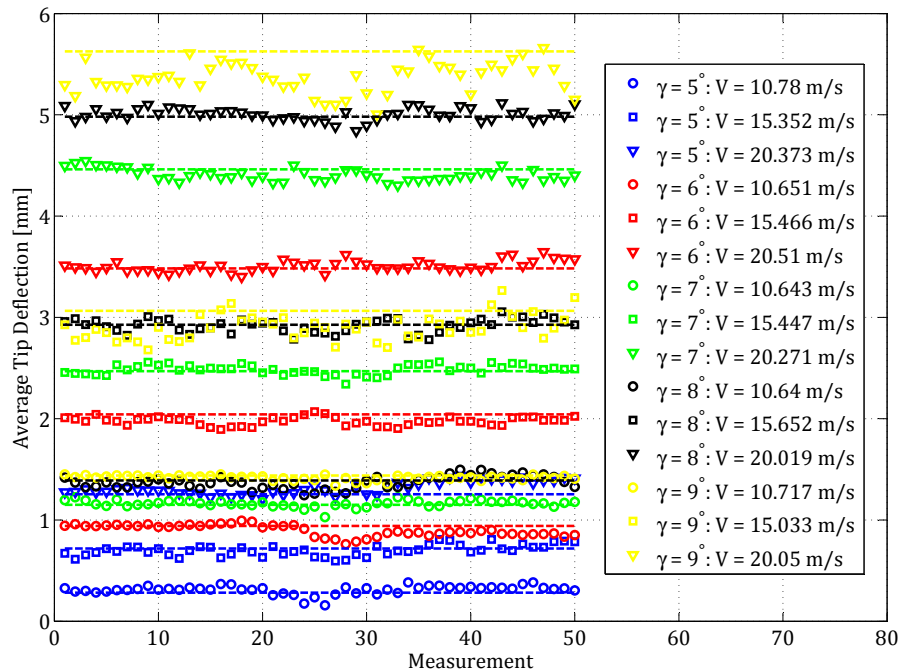


Figure 5.17: Average blade deflection relative to the recorded measurement, with the average deflection prior to base excitation plotted as a dashed line.

Figure 5.17 sums up the findings of the investigation. The average tip deflection was determined for each of the 50 recorded measurements associated with each experimental setup, which were plotted relative to a dashed line. It should be noted that this dashed line represents the blade tip deflection brought about by the airflow, absent of any base excitation. It can be seen that the recorded measurements, regardless of the base excitation frequency, experience roughly the same tip deflection over the course of an experimental setup. It is interesting to note that this deflection is consistent with the deflection experienced by the fan blade prior to the application of any base excitation. What this effectively means is that the blade deflects when it is

initially exposed to airflow in the test section. It then remains at this average tip deflection (dashed line) over the course of the variable base excitation, thereby effectively becoming the x' -axis about which the variable tip deflection amplitude propagates.

Once again, the measurements recorded at the highest tested airflow velocity, associated with γ equal to 9° , do not exhibit the same characteristics as the rest of the measurements. As previously mentioned, this could be as a result of flow separation. This analysis attempts to provide support to this claim. It appears as if the x' -axis about which the variable tip deflection amplitude propagates has effectively shifted to a lower tip deflection. The blade begins in a deflected state and then under the influence of the base excitation, deflects even further, before travelling in the opposite direction. What may not be clear at first glance, is that the blade could potentially be deflecting further in one direction, than in the other. Due to the nature of the angle of attack attributed to the setup, one direction will effectively be airflow assisted, while the other would be opposed.

Section B.2 of appendix B explores the effective angle of attack (α), which varies with regards to the length of the blade and time. It should be noted that the change of α is greatest at the blade's tip, where its velocity is greatest. It is at this point that the change in α has been quantified in section B.3.2. Table B.1 summarises the change in α and upon close examination, a trend may be found. Firstly, the greatest change with regards to the α is exhibited at low airflow rates. The reason being that the blade velocity is greater in magnitude relative to the airflow component acting in the same direction. It may further be noted that this change in α , regardless of the airflow velocity, becomes smaller as γ is increased. It is therefore unlikely that the rate of change of α is the reason for the instabilities experienced at high values of γ . A potential cause may however be determined when examining the maximum α of the blade. Even though the change in α becomes smaller as γ is increased, the maximum α does increase along with γ . It is suspected, that at lower values of γ , the blade did not achieve a maximum α great enough to bring about flow separation, while at high values of γ it did. The required α would only occur while the blade was airflow assisted, as α would be greater than the instance when the blade was airflow opposed. It is suspected that at maximum values of α , flow separation occurs if the magnitude of α is large enough. This flow separation would in turn bring about altered amplitude vibrations, which would not be experienced while the blade was airflow opposed and thereby bring about the shift in the average tip deflection measured at a specific value of γ . As a final point, it should be noted that at high values of α , the blade may even be entering a state of stall.

Chapter 6

Numerical Evaluation

It was shown in chapter 5 that the blade exhibited a large aerodynamic damping component, while subject to a free stream airflow. It was further noted the aerodynamic damping component was dependent on the blade's initial setting angle and the velocity of the free stream. The reasons for the aforementioned phenomenon has been discussed in section 5.5.3 and will be evaluated in the sections that follow.

6.1 Modelling Beam Vibration

6.1.1 Dynamic Euler-Bernoulli Beam Formulation

At the outset of the numerical evaluation, it was decided to employ the Euler-Bernoulli formulation of transverse beam vibration. The reason being that a single-degree-of-freedom system would not be able to account for the variable lift and drag forces experienced along the length of the blade. This point will be discussed in greater detail in section 6.1.4.

Equation 6.1 describes the displacement of a beam ($y(x, t)$) at location x and at time t , assuming that the beam has a constant cross-sectional area and that the it is undamped (Timoshenko *et al.*, 1974).

$$0 = EI \frac{\partial^4 y(x, t)}{\partial x^4} + m \frac{\partial^2 y(x, t)}{\partial t^2} \quad (6.1)$$

The constants E , I and m in equation 6.1 represent the beam's Young's Modulus, area moment of inertia and mass per unit length respectively. The product of E and I is commonly referred to as the flexural stiffness.

Equation 6.1 may be expanded to include a viscous damping component (C), resulting in it taking the form

$$0 = EI \frac{\partial^4 y(x, t)}{\partial x^4} + m \frac{\partial^2 y(x, t)}{\partial t^2} + C \frac{\partial y(x, t)}{\partial t} \quad (6.2)$$

Equation 6.2 describes the transverse displacement of the blade under both free vibration and base excitation, assuming that the blade is not exposed to external forces (e.g. air).

6.1.2 Boundary Conditions

Before equation 6.2 may be solved, it is necessary to define the boundary conditions of the system. Equations 6.3a to 6.3c define the boundary conditions to equation 6.2 for both free vibration and base excitation cases. They describe the physical properties of the blade, indicating that it is not subject to a slope at the fixed-end ($x = 0$) and that both the bending moment and shear stress at the free-end ($x = L$) are equal to zero.

$$\frac{\partial y}{\partial x} = 0 \Big|_{x=0} \quad (6.3a)$$

$$\frac{\partial^2 y}{\partial x^2} = 0 \Big|_{x=L} \quad (6.3b)$$

$$\frac{\partial y^3}{\partial x^3} = 0 \Big|_{x=L} \quad (6.3c)$$

The displacement boundary condition at the fixed-end ($x = 0$) is different for the free vibration and base excitation cases and may be described by the inequality

$$y = \begin{cases} 0 \Big|_{x=0}, & \text{for free vibration case} \\ 0.001 \sin(\omega_b t) \Big|_{x=0}, & \text{for base excitation case} \end{cases} \quad (6.4)$$

The transverse displacement of the beam's fixed-end is zero for the free vibration case and sinusoidal for the base excitation case.

6.1.3 Variable Angle of Attack

The blade's setting angle (γ) and the effective angle of attack (α) of the flow over the blade have been mentioned many times in the preceding chapters. This section serves to elaborate on the explanations offered thus far and details the implications on the numerical model.

It has been mentioned that the blade is subject to an effective angle of attack. In the context of the investigation, γ refers to the blade's setting angle relative to the flow direction of the wind tunnel. The need for α becomes apparent when the blade is subject to vibration and therefore possesses a velocity of its own. The implication is that there is a relative velocity effect of air in relation to the blade. When the blade has an γ which is not equal to zero, it experiences a greater change in relative airflow velocity in one direction, than in the other. Figure 6.1 serves to illustrate the preceding discussion.

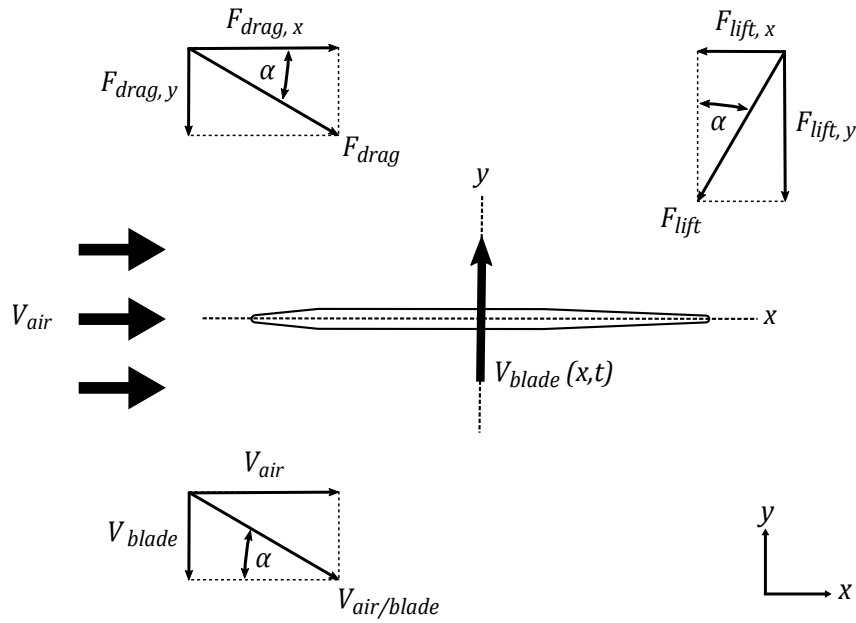


Figure 6.1: Blade angle of attack (α) during vibration and in the presence of a uniform airflow, while at a setting angle $\gamma = 0^\circ$.

It should also be apparent that the blade experiences an α which is dependent on position and time. The reason being that the blade's velocity varies along its length, which means the velocity of the air relative to the blade varies along with it.

The blade's absolute velocity may be described by

$$V_{blade} = V_{blade}(x, t)\underline{j} \quad (6.5)$$

where \underline{j} is the direction parallel to the plane of vibration (i.e. y).

The absolute velocity of the airflow may be described by

$$V_{air} = V_{air} \cos(\gamma)\underline{i} + V_{air} \sin(\gamma)\underline{j} \quad (6.6)$$

where \underline{i} is the direction perpendicular to the plane of vibration (i.e. x).

The velocity of the air relative to the blade may be obtained from the expression

$$V_{air} = V_{air/blade} + V_{blade} \quad (6.7)$$

the result of which is

$$V_{air/blade} = V_{air} \cos(\gamma)\underline{i} + V_{air} \sin(\gamma)\underline{j} - V_{blade}(x, t)\underline{j} \quad (6.8)$$

It is then possible to calculate the blade's effective angle of attack at a specific position along its length and at a point in time using

$$\alpha(x, t) = \tan^{-1} \left(\frac{V_{air} \sin(\gamma) - V_{blade}(x, t)}{V_{air} \cos(\gamma)} \right) \quad (6.9)$$

6.1.4 Modelling Lift and Drag Forces

The drag force imparted on the blade under static atmospheric conditions may be calculated using equation 2.1. The blade's coefficient of drag (C_d) for this scenario may be determined from the drag curve in figure E.1 ($\alpha = 90^\circ$). The coefficient remains constant, as there is no change in angle of attack.

The drag force exerted on the blade does however vary with regards to the distance from the fixed-end. As discussed in section 6.1.3, the blade's velocity per unit length varies along the length of the blade. The drag force may therefore be thought of as the product of $\frac{1}{2}C_d\rho_{air}A$ and $V_{blade}^2(x, t)$.

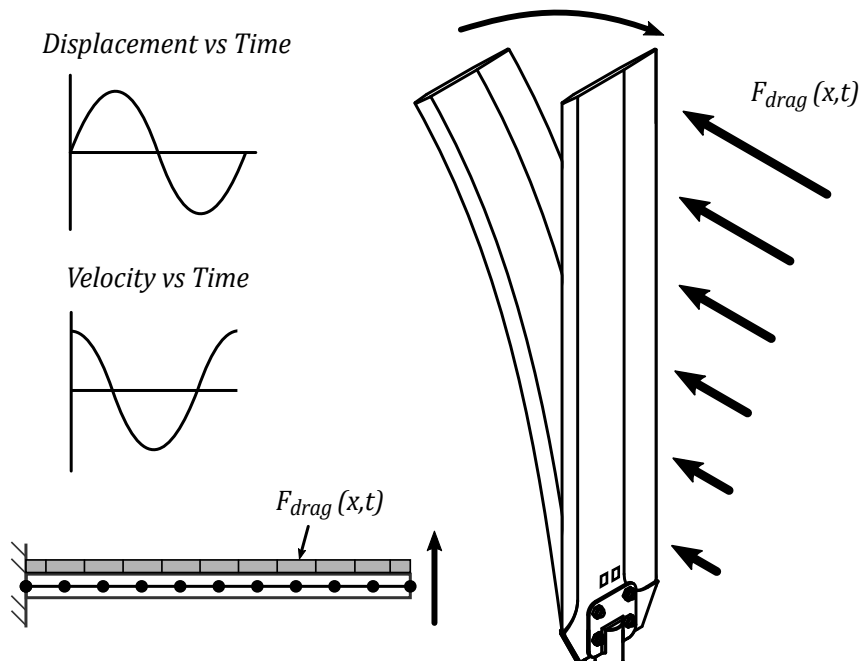


Figure 6.2: Drag force imparted on vibrating blade, under static atmospheric conditions.

The dynamic behaviour of the blade while subject to a uniform airflow may not be determined in this manner. As described in section 6.1.3, the blade experiences a change in its effective angle of attack. As a result, $V_{blade}^2(x, t)$ is not the only parameter that changes with regards to position and time. The lift and drag coefficients vary with regards to α .

The drag force acting on the blade in the direction of vibration may therefore be determined using

$$F_d(x, t) = \frac{1}{2}C_d(\alpha)\rho_{air}AV_{air/blade}^2(x, t) \sin(\alpha) \quad (6.10)$$

Similarly, the lift force acting on the blade in the direction of vibration is determined using

$$F_l(x, t) = \frac{1}{2} C_l(\alpha) \rho_{air} A V_{air/blade}^2(x, t) \cos(\alpha) \quad (6.11)$$

6.2 Discretization Method and Solver

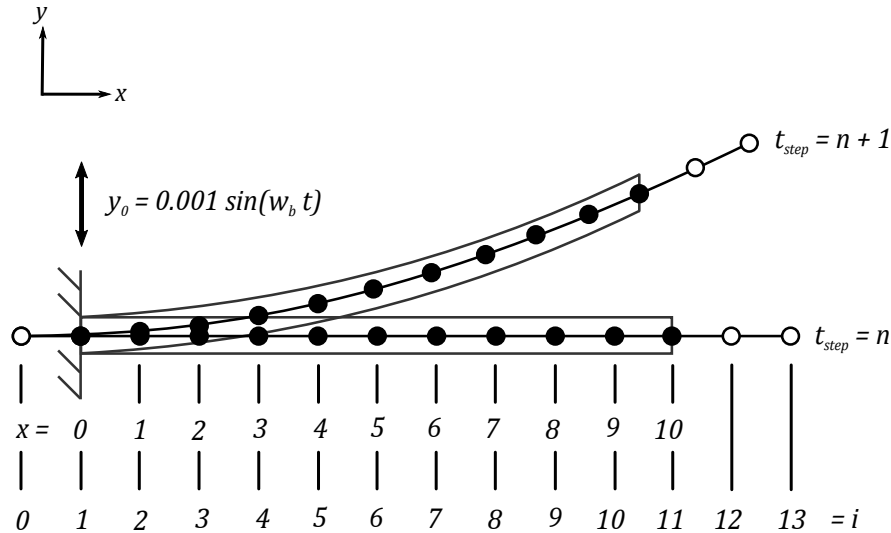


Figure 6.3: Schematic illustrating the discretization of the blade, for the case in which it has been split into 10 equal segments and the boundary condition at $i = 1$ corresponds to the base excitation variation of equation 6.4.

6.2.1 Method of Lines

The method of lines (MOL) is a technique developed to solve partial differential equations (PDE). The method utilizes the discretization of all but one variable, thereby making it possible to utilize general-purpose methods of integration developed for ordinary differential equations (ODE).

The method of lines, within the context of the investigation, refers to the construction of a numerical method in which only the spatial derivative term (i.e. $\partial^4 y(x, t) / \partial x^4$) is discretized and the time variable is left continuous. The discretization of the spatial derivative term results in the expression

$$\frac{\partial^4 y}{\partial x^4} = \frac{y_{i-2} - 4y_{i-1} + 6y_i - 4y_{i+1} + y_{i+2}}{\Delta x^4} \quad (6.12)$$

which has in turn been used to solve equation 6.2 as an initial value problem.

Sadiku and Obiozor (2000) describes the advantages of using the MOL, the most notable of which is its computational efficiency, resulting from the compact algorithm needed to formulate the semi-analytical approach. The method has also been known to exhibit numerical stability, owing to the fact that space and time have been separated. As an added advantage, well documented and reliable ODE solvers may be utilized to solve the PDE in question.

This was the approach taken for the numerical evaluation in this investigation. The selected ODE solver will be outlined in section 6.2.2.

6.2.2 Ordinary Differential Equation Solver

The ODE solver selected for the numerical evaluation was Matlab's 'ode45', which uses a variable step size Runge-Kutta method to solve differential equations numerically. It is based on an explicit Runge-Kutta formula known as the Dormand-Prince method, which uses six function evaluations to calculate fourth and fifth order accurate solutions (Dormand and Prince, 1980).

6.3 Modelling Cases

6.3.1 Case 1: Free Vibration

By accounting for the discretization of equation 6.2, the transverse displacement of each beam node may be calculated using

$$-[\mathbf{F}]_{drag} = \left(\frac{EI}{\Delta x^4} \right) [\mathbf{A}]\underline{y} + m \frac{\partial^2 \underline{y}}{\partial t^2} + C \frac{\partial \underline{y}}{\partial t} \quad (6.13)$$

where \mathbf{A} is a sparse matrix of the form

$$\mathbf{A} = \begin{bmatrix} 0 & 0 & 0 & 0 & \cdots & \cdots & \cdots & 0 & 0 \\ 0 & 7 & -4 & 1 & \ddots & & & & 0 \\ 0 & -4 & 6 & -4 & 1 & \ddots & & & \vdots \\ 0 & 1 & -4 & 6 & -4 & 1 & \ddots & & \vdots \\ \vdots & \ddots & \ddots & \ddots & \ddots & \ddots & \ddots & \ddots & \vdots \\ \vdots & & \ddots & \ddots & \ddots & \ddots & \ddots & \ddots & 0 \\ \vdots & & & \ddots & 1 & -4 & 6 & -4 & 1 \\ 0 & & & & \ddots & 1 & -4 & 5 & -2 \\ 0 & 0 & \cdots & \cdots & \cdots & 0 & 2 & -4 & 2 \end{bmatrix} \quad (6.14)$$

It should be noted that \underline{y} is a vector of the form

$$\underline{y} = [y_1 \quad y_2 \quad \cdots \quad y_i \quad y_{i+1}]' \quad (6.15)$$

where i is the number of blade segments.

The free vibration takes place in constant static atmospheric conditions. The blade is therefore expected to experience a constant drag coefficient. The drag force is dependent on the blade's vibrational velocity ($\underline{\dot{y}}$), which may be calculated using

$$[\mathbf{F}]_{drag} = C_d \rho_{air} A \begin{bmatrix} 0.5 & 0 & \cdots & 0 & 0 \\ 0 & 1 & \ddots & & 0 \\ \vdots & \ddots & \ddots & \ddots & \vdots \\ 0 & & \ddots & 1 & 0 \\ 0 & 0 & \cdots & 0 & 0.5 \end{bmatrix} \text{sgn}(\underline{\dot{y}}) \underline{\dot{y}}^2 \quad (6.16)$$

6.3.2 Case 2: Base Excitation in Static Atmospheric Conditions

Base excitation may be modelled using equation 6.13 once more by replacing the free vibration boundary condition, with the base excitation boundary condition described in equation 6.4. The boundary condition alters the discretized form of the equation by adding a time dependent vector which accounts for the base excitation. The resulting expression is

$$-\left(\frac{EI}{\Delta x^4}\right) [\mathbf{E}] - [\mathbf{F}]_{drag} = \left(\frac{EI}{\Delta x^4}\right) [\mathbf{A}]\underline{y} + m \frac{\partial^2 \underline{y}}{\partial t^2} + C \frac{\partial \underline{y}}{\partial t} \quad (6.17)$$

where \mathbf{E} is the time dependent vector of the form

$$[\mathbf{E}] = \left(\frac{EI}{\Delta x^4}\right) \sin(\omega_d t) [6 \quad -4 \quad 1 \quad 0 \quad \cdots \quad 0]' \quad (6.18)$$

Once again, the drag force exerted on the blade is expected to remain dependent solely on the blade's vibrational velocity. \mathbf{F}_{drag} may therefore be calculated using equation 6.16.

6.3.3 Case 3: Base Excitation in Moving Air

For this particular case, the blade is exposed to moving air and is expected to experience variable lift and drag forces. Equation 6.17 may then be modified to include a lift force, which then becomes

$$-\left(\frac{EI}{\Delta x^4}\right) [\mathbf{E}] - [\mathbf{F}]_{drag} - [\mathbf{F}]_{lift} = \left(\frac{EI}{\Delta x^4}\right) [\mathbf{A}]\underline{y} + m \frac{\partial^2 \underline{y}}{\partial t^2} + C \frac{\partial \underline{y}}{\partial t} \quad (6.19)$$

As described in section 6.1.4, the system describing the base excitation of the blade in moving air may not simply be modelled using constant lift and drag

coefficients. These coefficients are dependent on the effective angle of attack, as well as the squared velocity of each blade node.

\mathbf{F}_{drag} and \mathbf{F}_{lift} are similar in form to equation 6.16. The C_d constant in equation 6.16 however becomes a vector which may be described by either $C_d(\boldsymbol{\alpha})$ or $C_l(\boldsymbol{\alpha})$. What this means is that the respective coefficients are node dependent and are calculated using the α for the blade in question. Additionally, \mathbf{F}_{drag} and \mathbf{F}_{lift} must be broken into their respective components corresponding to the blade's direction of vibration, which may be clarified by consulting equations 6.10 and 6.11.

6.4 Results

6.4.1 Mesh Independence

The dependence of the solution on the number of blade divisions was investigated prior to the simulation of the results seen in the sections that follow. It should be noted that the outcome of the simulations associated with both the base excitation and free vibration numerical evaluations are not dependent on the number of blade divisions, for case studies conducted under ideal conditions. What this means is that for the investigated cases in which there is no air present, the solutions are independent of the number of blade divisions. This is as a result of the drag and lift forces experienced by the blade being dependent on the localized velocity of each blade segment. It was therefore necessary to conduct an investigation into the numerical model's mesh dependency, for a case in which the blade was subject to non-linear forces.

The mesh independence study was conducted for the base excitation case, which was executed in the presence of static atmospheric conditions. This particular case was selected, as the base excitation case is more complex than the free vibration case and was therefore believed to be more dependent on the number of blade divisions.

The base excitation frequency was elected to be equal to the blade's natural frequency, thereby resulting in the maximum possible transmissibility ratio. It is at this excitation frequency that the system is subject to the greatest sensitivity, making it the ideal place to monitor subtle changes. The number of blade divisions was increased from 5 to 40 and the motion transmissibility ratio was extracted from the resulting tip displacement sinusoid. The transmissibility ratio was then used to calculate the total damping experienced by the blade using equation D.48, as was done in chapter 5.

The results may be seen in figure 6.4. From the results, it was decided to divide the blade into 15 segments, as the damping ratio is the property of interest and it remains constant beyond 15 divisions. The computational expense involved in utilizing more divisions was therefore not justified.

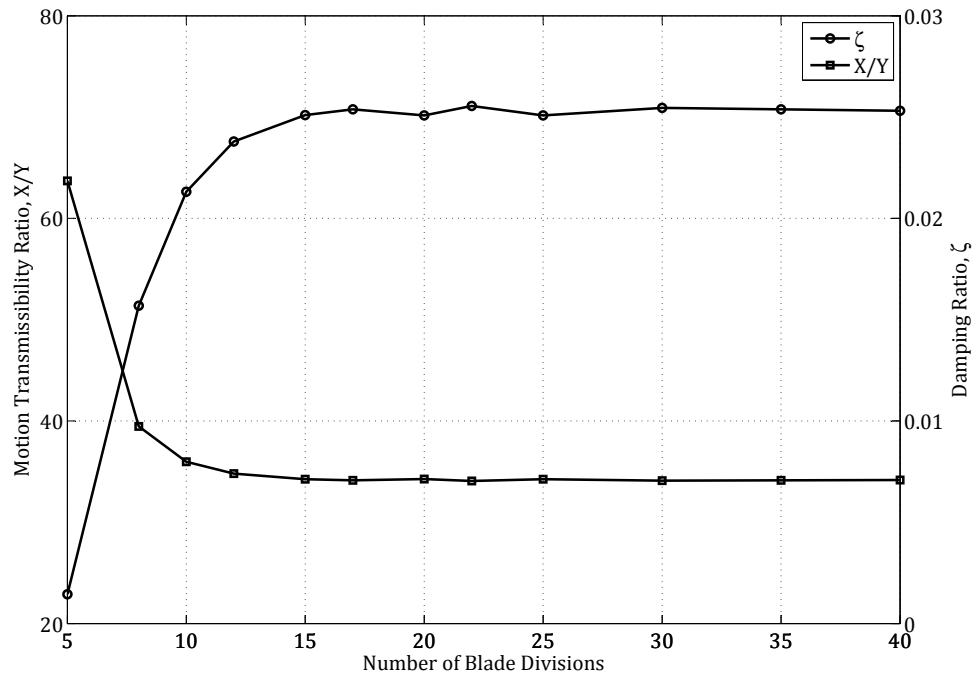


Figure 6.4: Combined plot depicting transmissibility ratio, X/Y and damping ratio, ζ relative to number of blade divisions.

6.4.2 Case 1: Free Vibration

Figure 6.5 shows the results obtained over the course of the numerical evaluation of the blade subjected to free vibration.

In order to evaluate whether the model was working as desired, a simulation was first conducted at the atmospheric conditions pertaining to one of the recorded data sets. The data set in question was recorded at a gauge pressure of -90 kPa and the simulation was configured accordingly. The results may be seen in figure 6.5 (a). It may be concluded that the simulation was working as desired, as the free response of the simulated blade followed the same trend as the recorded data. It should however be noted that the numerical free response experiences a variation in its tip deflection profile, which may be characterized as being 'wavy' in nature. This is due to the fact that the Euler-Bernoulli beam model used to model the blade is vibrating at multiple bending modes. The measured data does not appear to show the same trend in the figure. The reason for this difference is due to the fact that the measured data has been filtered to remove frequencies above its first bending mode. This was done due to the presence of a 50 Hz disturbance which does not correspond to any of the blade's higher bending modes. The measured data in figure 6.5 (a) thus

pertains solely to the blade's first bending mode.

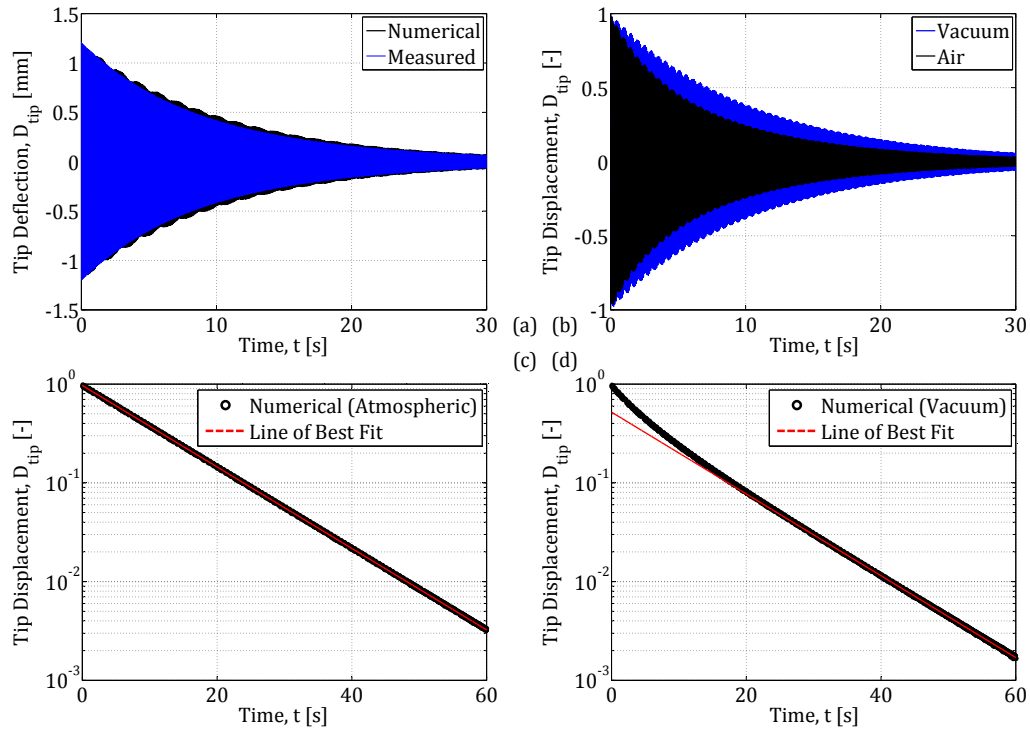


Figure 6.5: Results obtained during numerical free vibration evaluation.

Next, the free response of the blade was simulated at an initial tip deflection of 10 mm, at both vacuum and atmospheric conditions. These simulations serve to provide evidence to the explanation offered in section 4.3.3, regarding the non-linear free response profile seen at the outset of the vacuum chamber measurements. The atmospheric test was conducted at an air density of 1.2 kg/m^3 and the results were normalized with regards to the initial tip displacement. The results may be seen in figure 6.5 (b).

As expected, the blade's free response decays at an elevated rate, while in the presence of air. In order to more clearly illustrate this statement, the peak values have been plotted in a semi-logarithmic scale and may be seen in figure 6.5 (c) and (d). Figure 6.5 (c) shows the free response profile obtained under vacuum conditions, while figure 6.5 (d) shows the free response curve obtained at atmospheric conditions. It may therefore be concluded that the non-linearity at the outset of the results presented in section 4.3.3 were in fact due to the presence of air.

6.4.3 Case 2: Base Excitation in Static Atmospheric Conditions

The base excitation of the blade while in static atmospheric conditions was investigated at a constant air density of 1.2 kg/m^3 . Once again, the key area of interest pertains to the blade's damping ratio, which was calculated from the maximum transmissibility ratio (i.e. $\omega_b = \omega_n$). For this reason, the number of data points was limited to seven for each data set. A simulation was conducted in order to determine each of the data points in question.

As a point of comparison, the simulation was conducted at vacuum conditions. The results of the two air density cases may be seen in figure 6.6.

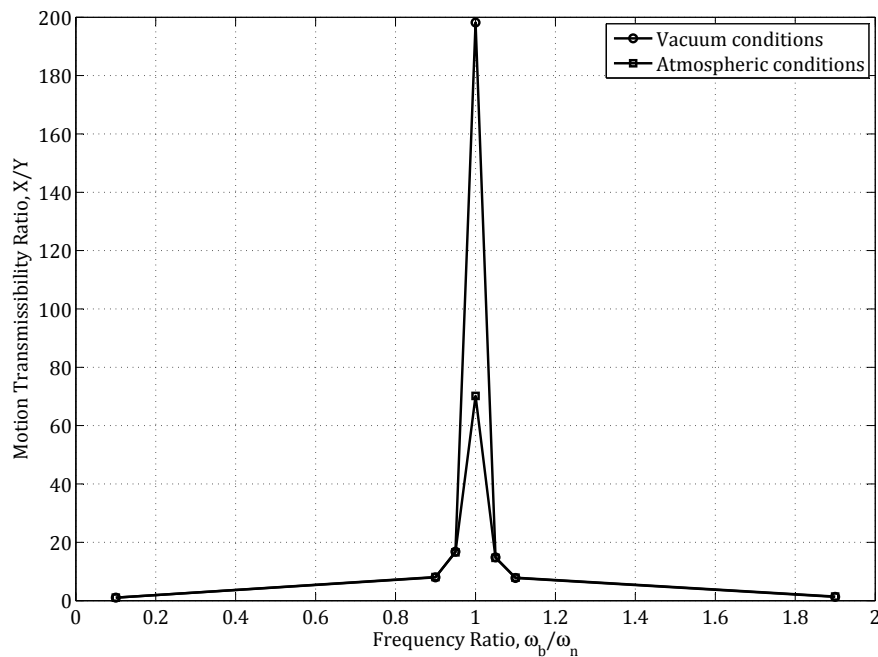


Figure 6.6: Numerically determined motion transmissibility ratio, X/Y relative to frequency ratio, for a blade at atmospheric and vacuum conditions.

It may be noted from the results that the presence of air has a dramatic effect on the dynamic behaviour of the blade. If one calculates the blade's damping ratio for each simulation using equation D.48, it may be seen that there is an increase in the presence of air. The damping ratios are 7.123×10^{-3} and 2.523×10^{-3} respectively. This is equivalent to a factor of 2.823 increase in damping. This phenomenon accounts for the change in the blade's damping ratio determined in chapter 5 (airflow velocity of 0 m/s) and the damping ratio calculated at vacuum conditions, as determined in chapter 4.

6.4.4 Case 3: Base Excitation in Moving Air

The blade was next simulated using equation 6.19 and the air density was once more set to a constant value of 1.2 kg/m^3 . It was hypothesised at the outset of the numerical evaluation that the elected modal would not be able to account for the complex fluid-structure interaction between the uniform airflow and the vibrating blade. It was therefore decided to investigate the blade at a setting angle (γ) equal to 0° and determine if there was a noticeable change in damping between the elected airflow velocities. The results of this investigation may be seen in figure 6.7.

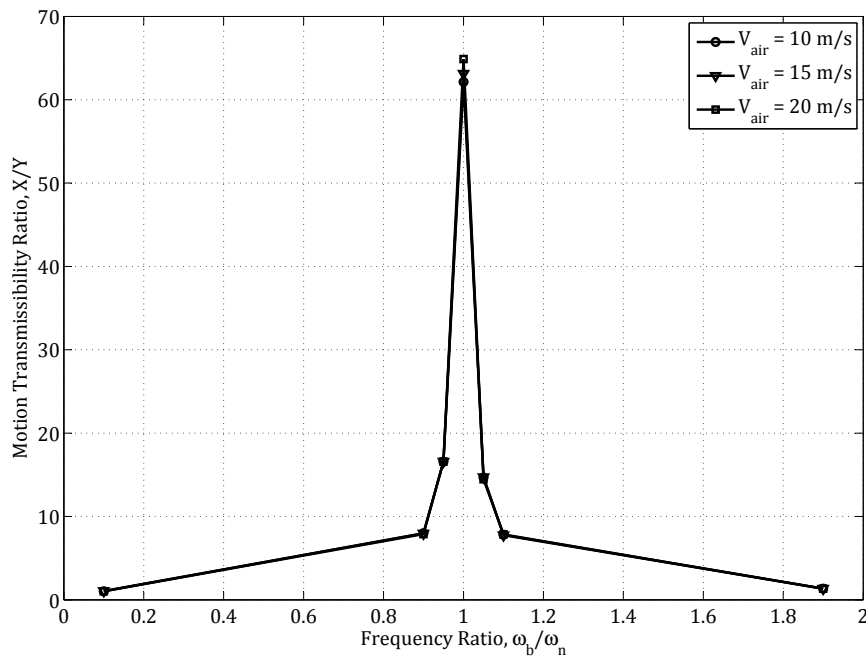


Figure 6.7: Numerically determined motion transmissibility ratio, X/Y relative to frequency ratio, for base excitation of the blade at various airflow velocities ($\alpha = 0^\circ$).

It was shown in chapter 5 that the blade experiences a dramatic increase in damping, when it is exposed to a uniform airflow velocity. Additionally, it was shown that this damping effect is dependent on the velocity of the airflow in question and increases along with the airflow velocity. As seen in figure 6.7, this effect is not evident in the simulation's results. In fact, the damping remains relatively constant. There is however an increase in the blade's damping, when compared to the static atmospheric conditions simulated in section 6.4.3. This is expected, as the blade is subject to a variable lift and drag force, instead

of the constant drag force imparted on the blade under static atmospheric conditions.

When one considers the blade's effective angle of attack experienced during the measured vibration, it may be shown from equation 6.9 that the experienced angle of attack is great enough to cause the blade to stall. This may be better understood by studying figure E.1. The blade stalls at angles as low as 16° . It is therefore reasonable to assume that there is flow separation taking place. The model utilized during this numerical evaluation is not equipped to incorporate complex fluid phenomena such as vortex shedding. The simulation thus serves as evidence that the lift and drag forces imparted on the blade are not solely responsible for the change in the blade's damping. It is likely that the blade is being excited by the shedding of vortices, which is bringing about a damping effect on the vibrational behaviour of the blade.

6.5 Advantages and Limitations of the Numerical Model

The model developed for the numerical evaluation is superior to single-degree-of-freedom (SDOF) systems typically used to replicate vibrating objects. By discretizing the spatial beam component, it was possible to model the variable drag and lift experienced along the length of the blade.

The only way the variable lift and drag could be included in a SDOF system would be to average the blade's velocity along its length, for every time step. This would not be an accurate method of modelling the phenomenon in question, as the portion of the blade near its free-end would experience larger velocities than the portion located near the fixed-end. As discussed in section 6.1.3, the effective angle of attack of the blade varies along its length, owing to the localized velocity of each blade segment. The drag and lift forces imparted on the blade are proportional to the respective lift (C_l) and drag coefficients (C_d), as well as the velocity of the air relative to the blade squared ($V_{air/blade}^2$).

Section 2.5 discusses the implications of vortex induced vibration. Although the above model succeeds at incorporating many of the phenomena that influence the dynamic response of the blade during vibration, it does not include vortex induced vibration. The only way that its influence on the blade may be examined would be to conduct a full-scale fluid structure interaction (FSI) analysis.

Chapter 7

Conclusions and Recommendations

The objective of this study was to investigate and characterize the effect of aerodynamic damping on an experimental axial flow fan blade. The investigation would serve as a starting point to a larger study into the dynamic behaviour of axial flow fans and has identified numerous areas of interest, in which future studies may be conducted. By determining the structural and dynamic properties of the fan blade in question, a fluid structure interaction (FSI) analysis may be performed in the future.

7.1 Quantifying the Structural Properties of the Fan Blade

Before experiments could be conducted, it was necessary to determine the structural properties of the fan blade. A series of static deflection tests were performed for a single load and multi-load configuration. The results demonstrated that the blade's deflection is dependent on the manner in which it is loaded, while its applied moment was shown to be independent. A calibration equation for the applied moment imparted on the blade was determined from the results, which were subsequently used to iteratively determine the blade's Young's Modulus. The process involved calculating the anticipated deflection for a range of loads, for both the single-load and multi-load configurations. Published data suggests that aluminium 5083 possesses a Young's Modulus between 70 and 80 GPa. Starting at 70 GPa, the Young's Modulus was increased until the calculated results from both the single-load and multi-load cases matched the measured results. The Young's Modulus was determined to be 74 GPa.

7.2 Vacuum Chamber Experiments

It was decided that in order to quantify the aerodynamic effects acting on the blade, it was first necessary to determine its vibrational properties absent the influence of air. A vacuum chamber was designed and manufactured for the purposes of the investigation. The chamber housed a mechanical assembly responsible for deflecting the blade's tip and bringing it into a state of free vibration. The vacuum-pump was however unable to achieve absolute vacuum. It was therefore decided to record the blade's free response incrementally between the lowest achievable pressure and atmospheric conditions. In this manner it was possible to map the change in the blade's vibrational properties relative to air density. The results showed a linear trend between the blade's damped frequency and the air density in which it was measured. This was also true for the damping ratio, with the damping ratio decreasing as the pressure approached vacuum and the damped frequency increasing. It was further possible to use the resulting trend to predict the blade's properties absent of the influence of air. The blade's damping ratio and natural frequency were determined to be 1.3333×10^{-3} and 11.3255 Hz, at vacuum conditions.

7.3 Wind Tunnel Experiments

The blade's aerodynamic damping was investigated by exciting the blade in the presence of a uniform airflow. The blade was excited by means of a base excitation mechanism, which was capable of imparting a constant translational displacement on the blade. The base excitation frequency was adjusted using a variable speed drive and was measured using an accelerometer. The blade's angle of attack was investigated and the airflow velocity was varied for each setting angle under investigation. The base excitation frequency was varied for each setup, from which it was possible to construct motion transmissibility curves. The results were compared to a test conducted at stagnant atmospheric conditions and it was shown that the total damping experienced by the blade increased when it was subject to a uniform airflow. Additionally, it was noted that the damping ratio increased along with the airflow velocity. Furthermore, the total damping imparted on the blade was shown to remain constant at setting angles between 0° and 5° . Higher angles showed an increase in the total damping. As the setting angle approached 9° however, the trends exhibited in the average blade displacement and total damping ratio relative to airflow velocity plots suggest that the blade was undergoing stall. The transmissibility curves further illustrated the results obtained during the vacuum chamber experiments, as the natural frequency of the blade was noted to be lower than the value determined for vacuum conditions.

7.4 Numerical Evaluation

The numerical evaluation served to provide evidence to the phenomenon exhibited by the blade over the course of the investigation. A dynamic formulation of the Euler-Bernoulli beam equation was modified to include variable drag and lift forces applied to the blade. The equation was solved numerically by utilizing the method of lines and discretizing the spatial component of the equation. The time component was then solved using a Matlab solver which utilizes a variable step size explicit Runge-Kutta formula. Simulations were performed for free vibration, base excitation in static atmospheric conditions and base excitation in moving air. The results obtained from the free vibration simulations illustrate the effect of air on the blade's vibration. The free vibration's logarithmic decay was shown to be non-linear, when the blade is in the presence of air. The simulations conducted in atmospheric conditions further show that the blade experiences a higher damping ratio while in the presence of air. The simulations conducted in moving air were however unable to recreate the damping trend exhibited during the wind tunnel experimentation. The simulation did however show that there would be an increase in the total damping, due to the change in lift and drag experienced by the blade in moving air. The results suggest that there are complex aerodynamic phenomena affecting the damping characteristics of the blade.

7.5 Recommendations for Future Work

Over the course of the investigation, there have been signs that complex fluid phenomena are at work when the blade is vibrated in the presence of moving air. It is suspected that the blade is succumbing to vortex induced vibration. It is therefore suggested that a series of fluid structure interaction simulations be conducted in order to isolate and evaluate the extent that the phenomena affects the vibrational properties of the blade.

The blade's variable angle of attack during vibration and while in the presence of a uniform airflow has been discussed at length. A computational fluid dynamic investigation into flow separation of the blade at variable blade positions would provide valuable insight into the fluid effects influencing the blade's dynamic behaviour.

The viability of a particle image velocimetry investigation should be evaluated. If possible, the investigation could potentially capture some of the fluid effects affecting the blade during the wind tunnel experimentation.

Appendices

Appendix A

Low Pass Filter Design

A.1 Kaiser-Bessel Window

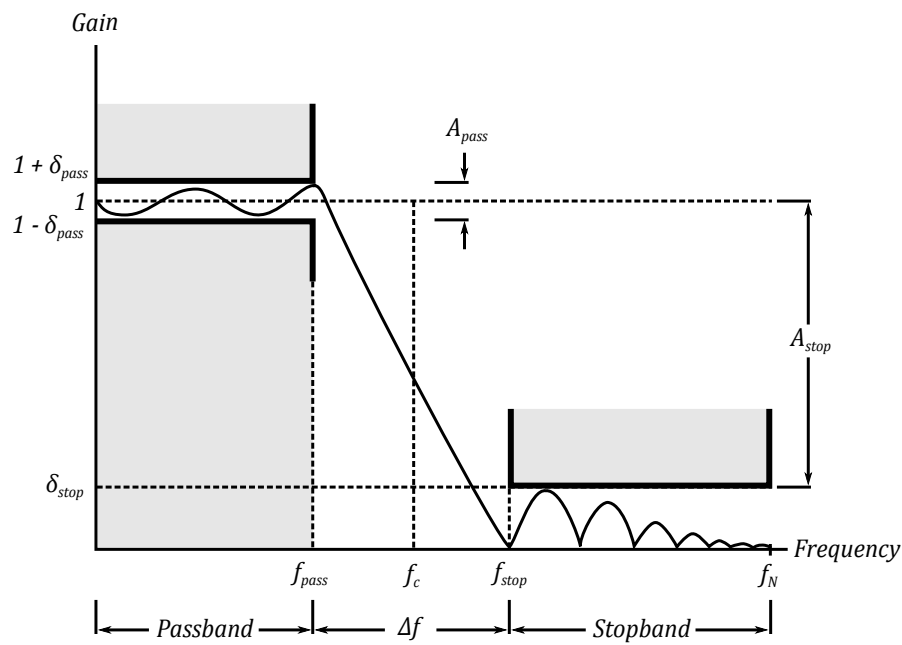


Figure A.1: Low-pass filter design.

The Kaiser window is a single-parameter window function employed in digital finite impulse response (FIR) filter design and is defined by the formula

$$w[nT] = \begin{cases} \frac{I_0\left(\beta\sqrt{1-\frac{4n^2}{(N-1)^2}}\right)}{I_0(\beta)}, & \text{for } |n| \leq \frac{N-1}{2} \\ 0 & \text{otherwise,} \end{cases} \quad (\text{A.1})$$

where N is the length of the sequence, T is the sampling period and β is the independent control parameter, also referred to as the shape parameter. I_0 is the zero-order Modified Bessel Function and may be defined as

$$I_0(x) = 1 + \sum_{k=0}^{\infty} \left(\frac{\left(\frac{x}{2}\right)^k}{k!} \right)^2 \quad (\text{A.2})$$

A FIR low-pass filter that satisfies the specifications indicated in figure A.1 can be designed using a procedure detailed by Kaiser. This procedure will be highlighted below and has been adapted from (Antoniou, 2007).

The first step is to determine the impulse response $h(nT)$ using a Fourier series analysis and assuming an idealized frequency response

$$H(e^{jwT}) = \begin{cases} 1, & \text{for } |w| \leq w_c \\ 0, & \text{for } w_c < |w| \frac{w_s}{2} \end{cases} \quad (\text{A.3})$$

where w_s is the angular sampling frequency in rad/s, obtained by using

$$\begin{aligned} w_s &= 2\pi f_s \\ f_s &= \frac{1}{T} \end{aligned} \quad (\text{A.4})$$

where f_s is the sampling frequency in Hz.

The angular cutoff frequency (w_c) can then be determined using the pass-band (f_{pass}) and stopband (f_{stop}) frequencies

$$\begin{aligned} f_c &= \frac{1}{2}(f_{pass} + f_{stop}) \\ w_c &= 2\pi f_c \end{aligned} \quad (\text{A.5})$$

Next, the common ripple (δ) must be chosen so that the calculated passband attenuation (A_{pass}) and stopband attenuation (A_{stop}) are both less than the specified values. A suitable value for δ may be taken as the minimum of the passband ripple (δ_{pass}) and the stopband ripple (δ_{stop})

$$\delta = \min(\delta_{pass}, \delta_{stop}) \quad (\text{A.6})$$

where δ_{pass} and δ_{stop} are calculated using

$$\begin{aligned} \delta_{pass} &= \frac{10^{0.05A_{pass}} - 1}{10^{0.05A_{pass}} + 1} \\ \delta_{stop} &= 10^{-0.05A_{stop}} \end{aligned} \quad (\text{A.7})$$

The attenuation of δ in dB can then be calculated using

$$A = -20 \log_{10} \delta \quad (\text{A.8})$$

which in turn is used to choose a suitable shape parameter using the inequality

$$\beta = \begin{cases} 0, & \text{if } A < 21 \\ 0.5842(A - 21)^{0.4} + 0.07886(A - 21), & \text{if } 21 \leq A \leq 50 \\ 0.1102(A - 8.7), & \text{if } A > 50 \end{cases} \quad (\text{A.9})$$

Next, the filter order (N) is determined with

$$N = \begin{cases} \frac{A-7.95}{2.285\pi\Delta f'}, & \text{if } A > 21 \\ \frac{5.79}{\pi\Delta f'}, & \text{if } A \leq 21 \end{cases} \quad (\text{A.10})$$

where $\Delta f'$ is the dimensionless transition width. The transition width can be calculated and then subsequently normalized using

$$\begin{aligned} \Delta f &= f_{stop} - f_{pass} \\ \Delta f' &= \frac{\Delta f}{f_N} \end{aligned} \quad (\text{A.11})$$

It should be noted that f_N is known as the Nyquist frequency and is defined as half the sampling frequency

$$f_N = \frac{1}{2}f_s \quad (\text{A.12})$$

and that the cutoff frequency may be normalized in a similar fashion to equation, A.11

$$f'_c = \frac{f_c}{f_N} \quad (\text{A.13})$$

Finally, equation A.1 may be formed and then in turn used in conjunction with the infinite duration impulse response $h_d[nT]$ to determine the filter impulse response

$$h[nT] = h_d[nT]w[nT] \quad (\text{A.14})$$

where $h_d[n]$ can be determined using

$$h_d[n] = \frac{\sin[\pi f'_c(n - \frac{N}{2})]}{\pi(n - \frac{N}{2})} \quad (\text{A.15})$$

A.2 LP Filter Implementation and Evaluation

The data analysis conducted during the course of the vacuum chamber experimentation detailed in chapter 4 required the use of a low-pass filter in order to eliminate all unwanted noise from the measured data sets.

Figure A.2 examines a portion of a typical data set obtained over the course of the experimentation. The blade has been given sufficient time to damp the

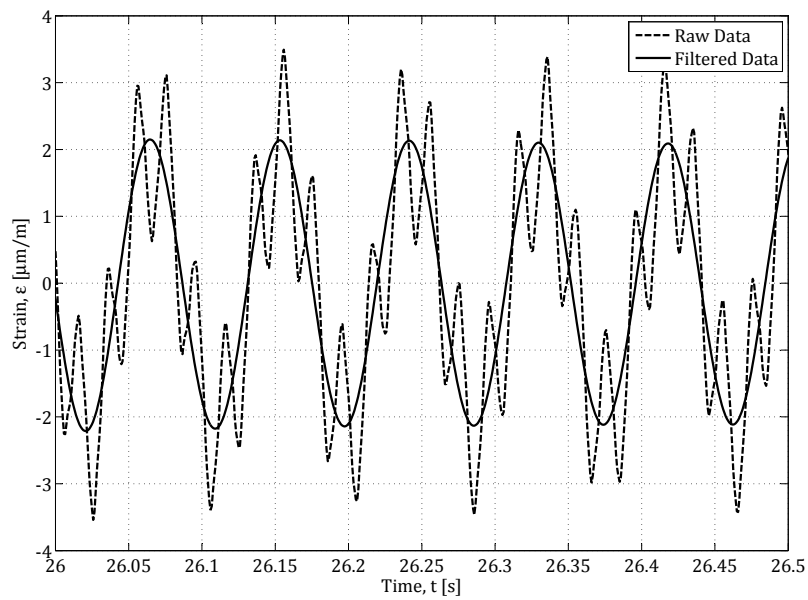


Figure A.2: Comparison between the raw data and filtered data of the blade, while in a state of free response. The data was obtained during the course of the vacuum chamber experimentation described in chapter 4, at a gauge pressure of -90 kPa.

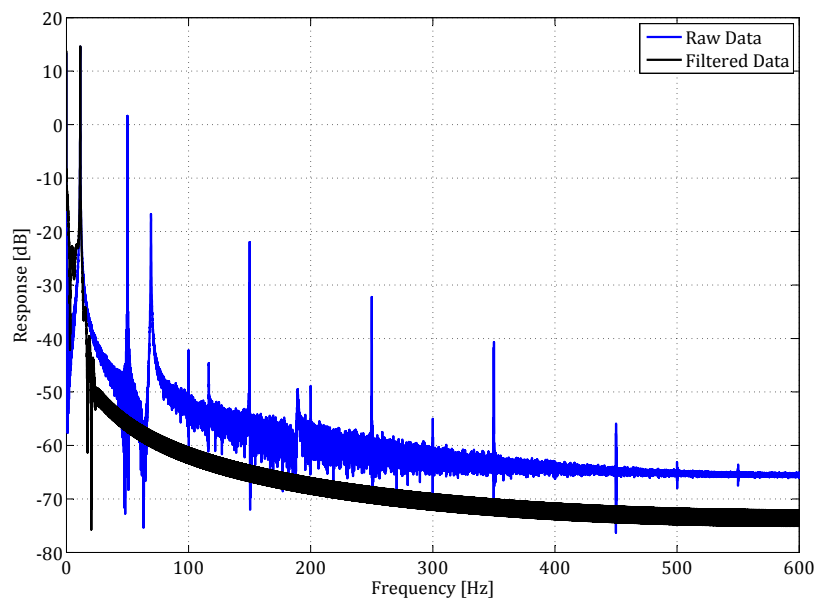


Figure A.3: Evaluation of filter performance using a FFT analysis of the data depicted in figure A.2.

majority of its amplitude response. The figure shows that any data analysis conducted on the raw data would result in the location of false peaks or additional data points on the x-axis. This means that any period determined using either method of peak detection would result in an inaccurate measurement of the blade's damped frequency. This is also true for the calculation involving the logarithmic decrement of the blade's amplitude response, which would subsequently result in an inaccurate representation of the blades damping ratio.

Figure A.3 examines the performance of the low-pass filter and shows that there has been a notable reduction of unwanted frequencies influencing the measured data. It can thus be concluded that the filter is working as desired and that the relevance of the analysed results has been improved.

Appendix B

Analytical Evaluation of Blade Dynamics

B.1 Blade Velocity

In order to develop a greater understanding of the blade's behaviour, it was decided to derive an expression for its average velocity during vibration. For the purposes of this discussion, it will be assumed that the blade's maximum tip deflection is known.

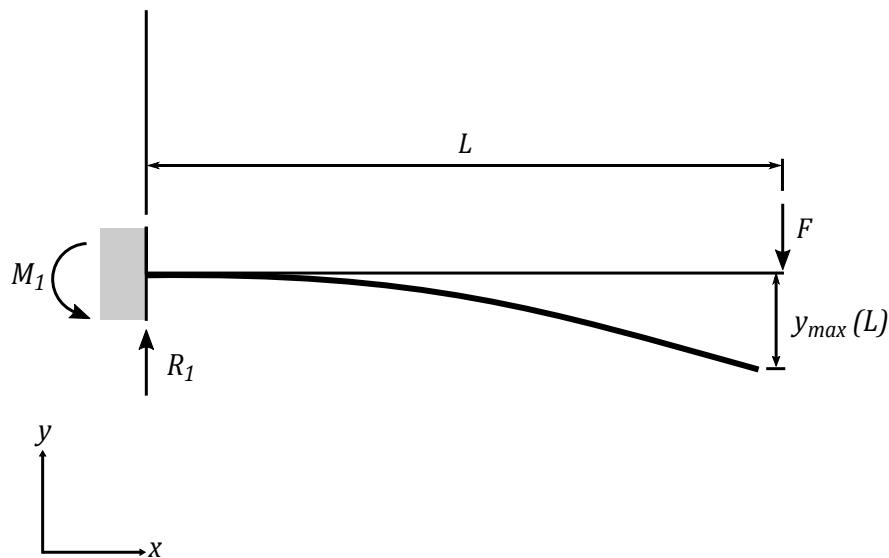


Figure B.1: Cantilever beam subject to an end load.

Figure B.1 depicts a typical cantilever beam, which will be used to model

the fan blade. The beam deflection, y is a function of both x and t . It may be represented by the expression

$$y(x, t) = y_{max}(x) \sin(\omega_n t) \quad (\text{B.1})$$

where y_{max} is the maximum deflection the beam is subjected to, at the distance x from the fixed point. This expression may then be differentiated to obtain the blade's velocity

$$V_{blade}(x, t) = y_{max}(x) \omega_n \cos(\omega_n t) \quad (\text{B.2})$$

Equation B.2 describes the velocity of the blade at an instant in time, for a segment of the blade located at distance x from the fixed point. The key area of interest with regards to the blade's velocity pertains to the aerodynamic damping, which is accepted to be proportional to V_{blade}^2 . It is therefore convenient to calculate the average squared velocity using

$$\bar{V}(x)^2 = \frac{1}{T} \int_0^T V(x, t)^2 dt \quad (\text{B.3})$$

the result of which is

$$\bar{V}(x)^2 = \frac{1}{2} y_{max}(x)^2 \omega_n^2 \quad (\text{B.4})$$

The above expression offers significant insight, but varies with regards to the distance x . It would therefore be of value to calculate the average velocity with regards to length as well. Before this can be done however, it is necessary to determine an expression which describes the blade's deflection with regards to the distance x and the maximum tip deflection $y_{max}(L)$.

Owing to its constant cross-sectional area, the blades tip deflection may be calculated using

$$y_{max}(x) = \frac{F x^2}{6EI} (x - 3L) \quad (\text{B.5})$$

where F is a point load, E is the Young's Modulus and I is the area moment of inertia of the blade. It is a simple matter to determine the maximum tip deflection, which may be described as

$$y_{max}(L) = -\frac{FL^3}{3EI} \quad (\text{B.6})$$

Equations B.5 and B.6 were manipulated in order to make E , I and F the subject of the respective formulas. The equations were then subsequently equated and the resulting expression for blade deflection was obtained

$$y_{max}(x) = -\frac{y_{max}(L)}{2L^3} (x^3 - 3Lx^2) \quad (\text{B.7})$$

Equation B.7 was then substituted into equation B.4 resulting in the expression

$$\bar{V}(x)^2 = \frac{y_{max}(L)^2}{8L^6} (x^6 - 6Lx^5 + 9Lx^4) \omega_n^2 \quad (\text{B.8})$$

The blade's overall average squared velocity (\bar{V}^2) could then be determined by integrating the time averaged squared velocity over the length of the blade

$$\bar{V}^2 = \frac{1}{L} \int_0^L \bar{V}(x)^2 dx \quad (\text{B.9})$$

which resulted in the expression

$$\bar{V}^2 = \frac{33}{280} y_{max}(L)^2 \omega_n^2 \quad (\text{B.10})$$

B.2 Angle of Attack

The setting angle (γ), within the context of the study, is defined as the angle measured between the line of the blade's chord and the absolute airflow velocity, while the blade is in a static state. The purpose of this section will be to explore the effect of the blade's deflection on the angle of attack (α), as a result of the induced base excitation. Figure B.2 has been added to aid in the discussion and depicts the cross-sectional blade profile orientated at a setting angle relative to a uniform airflow.

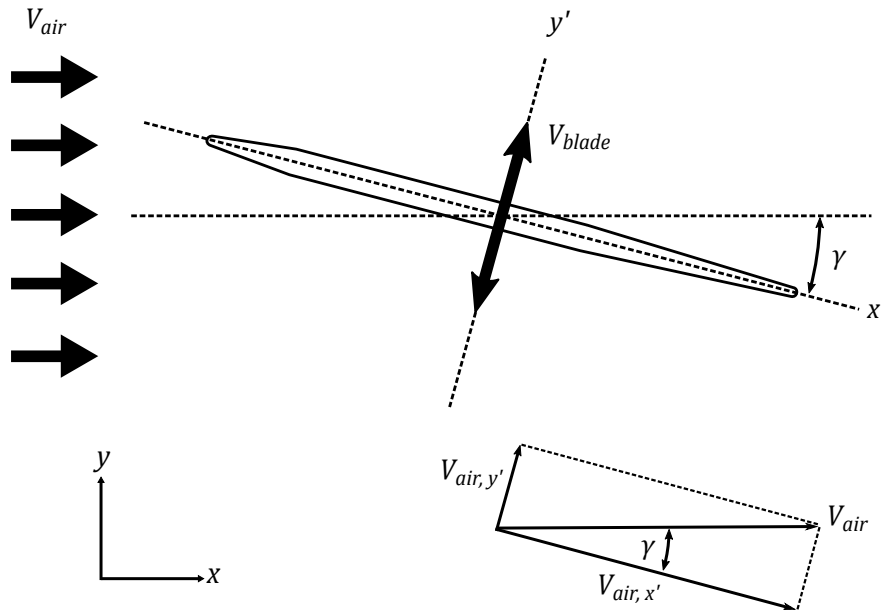


Figure B.2: Blade setting angle.

The airflow velocity may be broken up into its components defined by the x' and y' - axes

$$V_{air,y'} = V_{air} \sin(\gamma) \quad (\text{B.11})$$

$$V_{air, x'} = V_{air} \cos(\gamma) \quad (\text{B.12})$$

From these expressions and with the help of figure B.2 it is possible to define the relative velocity in component form

$$V_{rel, x'} = V_{air, x'} \quad (\text{B.13})$$

$$V_{rel, y'}(x) = V_{air, y'} - V_{blade}(x, t) \quad (\text{B.14})$$

The blade's angle of attack during vibration may be calculated from the relative velocity components. This is accomplished using simple trigonometry and results in the expression

$$\alpha(x) = \arctan \left(\frac{V_{air} \sin(\gamma) - y_{max}(x)\omega_n \cos(\omega_n t)}{V_{air} \cos(\gamma)} \right) \quad (\text{B.15})$$

where α is the changing angle of attack. From this expression it is clear that α is proportional to the maximum blade deflection at a distance x . An observation may therefore be made that the blade's instantaneous angle of attack varies with regards to the distance from the attachment point. The blade deflection is greatest at the tip, making it the location of the greatest change in angle of attack. These observations may thus be summarised in the equation

$$\alpha(max, min) = \arctan \left(\frac{V_{air} \sin(\gamma) \pm y_{max}(L)\omega_n}{V_{air} \cos(\gamma)} \right) \quad (\text{B.16})$$

B.3 Sample Calculations

B.3.1 Added Mass Effect of Air on the Blade

Section 5.5.2 of chapter 5 discusses the implications of subjecting the blade to a base excitation, under atmospheric conditions. The sample calculation that follows serves as evidence to the explanation.

The added mass effect imparted on a moving object in a fluid has been discussed in section 2.3 of chapter 2. Equation 2.2 is used to calculate the added mass imparted on the blade, while it undergoes base excitation in atmospheric conditions. The equation takes the form

$$m_a = \rho_{air} \pi a^2 \quad (\text{B.17})$$

where m_a is the added mass due to air, ρ_{air} is the air density and a is half the width of the blade, as detailed in figure 2.1. The blade possesses a width of 0.12m and if the air density is assumed to be 1.184 kg/m³, the added mass per unit length imparted on the blade is equal to 0.013 kg/L.

The blade possesses a uniform cross-sectional area and its stiffness (k_{blade}) may therefore be calculated using the expression

$$k_{blade} = \frac{3EI}{L^3} \quad (\text{B.18})$$

The constants E , I and L have been discussed in chapter 3. They are 74 GPa, $829.35 \times 10^{-12} \text{ m}^4$ and 0.572 m respectively. The blade's stiffness may then be shown to be equal to 983.79 N/m.

The natural frequency of the blade, absent of the influence of air, was determined in chapter 4 to be 11.3255 Hz. This value, along with the stiffness may be used to calculate the mass per unit length of the blade (m_{blade}), by rearranging $\omega_n = \sqrt{\frac{k_{blade}}{m_{blade}}}$ to form

$$m_{blade} = \frac{k_{blade}}{\omega_n^2} \quad (\text{B.19})$$

The value for m_{blade} is therefore equal to 0.194 kg/L.

As the mass of the blade during base excitation is expected to increase by 0.013 kg/L, it is logical to assume its natural frequency must become smaller. The blade's adjusted natural frequency (ω'_n) may be calculated using

$$\omega'_n = \sqrt{\frac{k_{blade}}{m_{blade} + m_a}} \quad (\text{B.20})$$

which results in a value of 10.954 Hz.

This adjusted natural frequency is 0.369 Hz lower than the natural frequency of the blade in vacuum conditions. The shift in the transmissibility curves discussed in section 5.5.2 may therefore be attributed to this phenomenon.

The transmissibility ratio of the base excitation curve has been shown to be a maximum at a frequency ratio of 0.972. Using ω'_n , the adjusted frequency ratio (r') may be calculated using

$$r' = \frac{\omega'_n}{\omega_n} \quad (\text{B.21})$$

which results in a value of 0.967. The difference between the measured frequency ratio and the adjusted frequency ratio corresponds to an error of 0.514 %.

As an added note, the adjusted natural frequency coincides with the 1st bending mode measured during the FRF analysis discussed in section 3.5 of chapter 2. The FRF analysis, like the baseline wind tunnel experiment, was conducted at atmospheric conditions and was therefore subject to the influence of air.

B.3.2 Effective Angle of Attack of the Blade during Vibration

Section B.2 has analytically explored the blade's changing angle of attack, while subject to vibration. This sample calculation examines the blade's changing effective angle of attack for the wind tunnel experiments examined in section 5.5 of chapter 5.

Table B.1: Summary of the blade's effective angle of attack exhibited during wind tunnel experiments, while subject to base excitation.

γ	V_{air}	α (max)	α (min)	$\Delta\alpha$ (max)	$\Delta\alpha$ (min)
0°	10.931 m/s	10.804°	-10.804°	10.804°	10.804°
	15.405 m/s	6.146°	-6.146°	6.146°	6.146°
	20.335 m/s	3.682°	-3.682°	3.682°	3.682°
5°	10.78 m/s	15.663°	-6.018°	10.663°	11.018°
	15.352 m/s	11.141°	-1.258°	6.141°	6.258°
	20.373 m/s	8.683°	1.276°	3.683°	3.725°
6°	10.651 m/s	15.048°	-3.356°	9.048°	9.356°
	15.466 m/s	10.686°	1.232°	4.686°	4.768°
	20.51 m/s	8.912°	3.057°	2.912°	2.943°
7°	10.643 m/s	15.677°	-2.01°	8.677°	9.01°
	15.447 m/s	11.110°	2.816°	4.110°	4.184°
	20.271 m/s	9.401°	4.574°	2.401°	2.426°
8°	10.64 m/s	16.235°	-0.579°	8.235°	8.579°
	15.652 m/s	11.568°	4.369°	3.568°	3.651°
	20.019 m/s	10.264°	5.711°	2.264°	2.289°
9°	10.717 m/s	16.792°	0.859°	7.792°	8.141°
	15.033 m/s	12.598°	5.329°	3.598°	3.671°
	20.05 m/s	11.446°	6.520°	2.446°	2.480°

The blade's maximum and minimum effective angle of attack was calculated using equation B.16, for each of the experiments conducted in the wind tunnel. The results may be found in table B.1, where $\Delta\alpha$ refers to the difference between γ and either the maximum or minimum α . It should be noted that the change in the effective angle of attack was limited to the resonant base excitation frequency (i.e. $r = 1$), as the maximum transmissibility ratio would result in the greatest variation in effective angle of attack.

Appendix C

Wind Tunnel Experiments - Additional Information

C.1 Base Excitation Analysis and Modification

The base excitation mechanism described in section 5.2.1 was originally designed and used by a final year student. It was therefore necessary to perform a detailed analysis prior to any experimentation in order to ascertain whether the apparatus was working in the desired manner.

An accelerometer was attached to the front of the blade mount, as indicated in figure 5.2 and the base excitation mechanism was operated at a number of different frequencies. The signal produced by the accelerometer was recorded relative to time and a typical response of one of these measurements may be seen in figure C.2 (a). The signal reflects that the input was sinusoidal in nature, but it is also clear that there is a considerable amount of noise present in the signal. More importantly, the peaks of the sinusoid are exaggerated relative to the rest of the signal. It was hypothesised that the blade mount was subjected to a number of impulse-like forces. Noise on the signal could be filtered out in order to determine the frequency of the base excitation, but the presence of impulses could potentially influence the vibrational response of the blade itself. It was therefore necessary to locate the source of the impulses and mitigate its effect on the blade mount.

Upon examination, it was determined that the crank arm, seen in figure C.2, was insufficiently located. The arm was able to move in the y-direction and although it was unclear from a cursory examination, it was suspected that the arm was insufficiently located in the x and z-directions as well. This theory was tested by operating the base excitation mechanism at a constant frequency and temporarily constraining the crank arm in various directions, by applying a force in the direction in question. It should be noted that the base excitation frequency was unaltered during the process and the resulting curves can be seen in figure C.1. Figure C.1 (b) shows the acceleration of the blade mount with

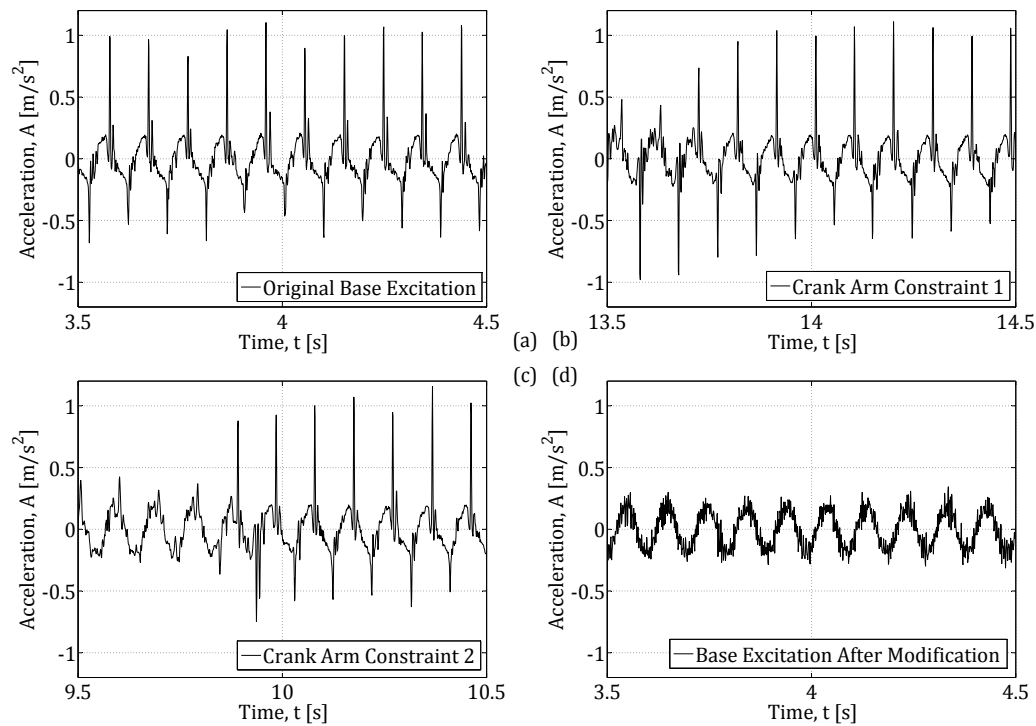


Figure C.1: Series of acceleration-time graphs depicting a portion of the time measurements taken, emphasising the improvement of the base excitation mechanism.

the crank arm constrained in the x-direction and after approximately 13.75 s the constraining force was altered to act in the z-direction. Figure C.1 (c) shows the signal produced with the crank arm constrained in the y-direction, in addition to the x and z-directions. Once more, in order to help illustrate the difference, the constraints were abandoned after approximately 9.9 s.

It was therefore determined that the hypothesised source of the impulses was correct and a number of modifications were made to the base excitation mechanism assembly. The needle bearings which were located in the crank arm were replaced with new slightly larger bearings. This allowed the holes in which the needle bearings were located to be counter-bored to a finer tolerance, thereby eliminating any movement in the x and z-directions. In order to eliminate the movement in the y-direction, phosphor bronze bushes were manufactured and added to the assembly in the locations indicated in figure C.2. The bushes were manufactured out of phosphor bronze owing to the high strength and toughness of the material, along with its low coefficient of friction.

The result of these modifications are illustrated in figure C.1 (d). It can be seen that the impulses acting on the peaks of the sinusoids have been eliminated and there is an overall improvement in the shape of the sinusoids.

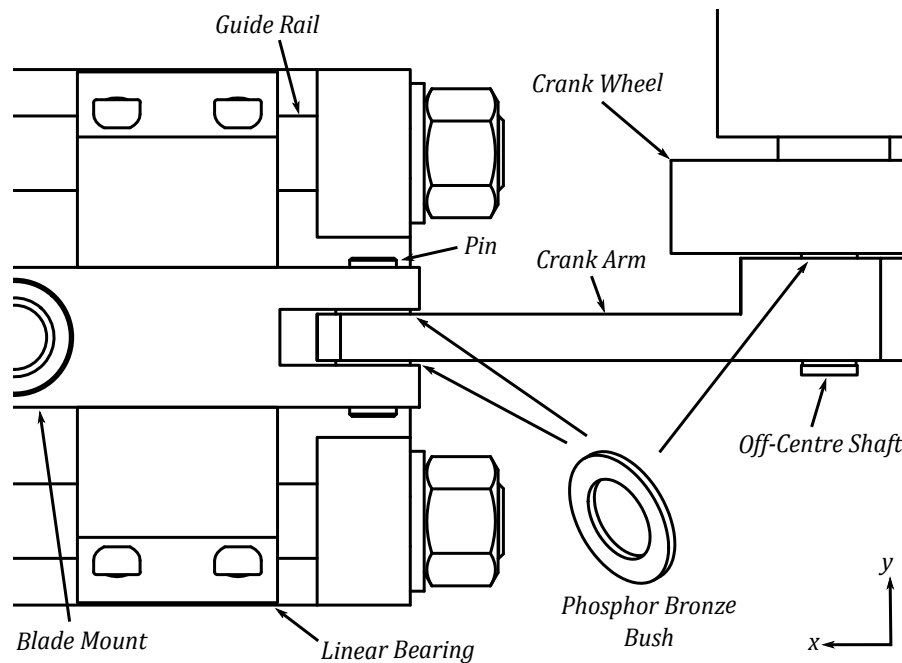


Figure C.2: Detailed look at the base excitation mechanism, with the location of the phosphor bronze bushes emphasised.

C.2 Determining Measurement Intervals

The baseline refinement mentioned in section 5.4.1 will now be examined in detail. The baseline motion transmissibility curves, resulting from the iterative process in question, have been plotted in figure C.3. The curves were constructed in the same manner described in chapter 5, but differ in terms of the number of recorded measurements, as well as with regards to the base excitation frequency interval between the respective measurements.

The importance of refining the proposed base excitation frequencies becomes apparent when one compares the first three baselines. There is a significant difference between not only the magnitude of the individual peaks, but also in their widths. These characteristics have been used to determine the total damping experienced by the blade and are therefore of paramount importance. The final baseline will be considered later in this section.

The baseline curves were constructed one after the other and the resulting motion transmissibility curves carefully examined. From the examination it was possible to determine potential areas of interest, such as the location of the peak. It was then possible to refine the number of data points in the specific area of interest, before conducting the next test. It should be noted that significantly more measurements were recorded in the area surrounding the peak and careful attention was paid to determining the exact frequency at which the motion transmissibility was a maximum. The peak was located by examining the strain in real time, while slowly altering the base excitation

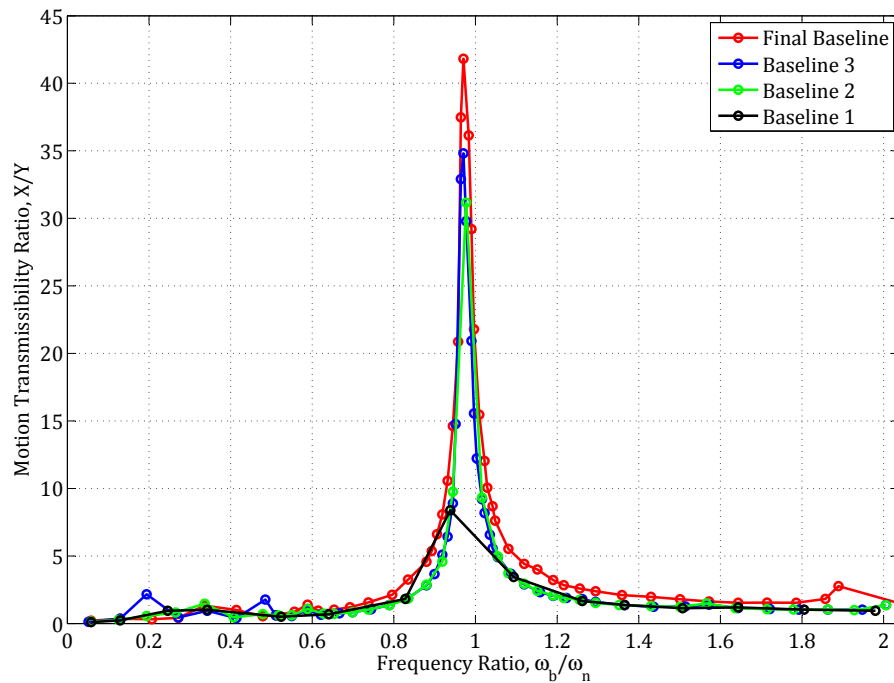


Figure C.3: Comparison of baseline motion transmissibility ratios.

frequency until the maximum strain amplitude was achieved. It may be interesting to note that it was possible to audibly detect when the blade was vibrating at its natural frequency.

As previously mentioned, the final baseline has been included in figure C.3. There is a significant difference between the final baseline and the iterative baselines used to refine the measurement frequencies. The reason for this is that there was a flaw in the base excitation mechanism's blade mount design, which was discovered during preliminary testing. It was determined that the blade was unable to securely locate in the blade mount, which brought about structural damping. The problem was rectified prior to the final experimentation responsible for the results seen in section 5.5. This topic will be discussed in section C.4.

C.3 Flow Calculations

C.3.1 Reynolds Number

Before any experimentation could occur, it was necessary to determine the expected Reynolds number (Re) using

$$Re = \frac{\rho V h_d}{\mu} \quad (\text{C.1})$$

where ρ is the air density, V is the free stream velocity, h_d is the hydraulic diameter and μ is the dynamic viscosity.

It was decided to conduct the experiments at velocities of 10 m/s, 15 m/s and 20 m/s. As discussed in chapter 5, the air flow velocities could not precisely be controlled and as a result, the actual velocities were expected to be marginally above or below the intended values. It was thus necessary to determine the Reynolds number at the limits of the intended air flow velocity range, which were conservatively estimated to be 5 m/s and 25 m/s.

Before the Reynolds number could be calculated, it was necessary to determine the hydraulic diameter of the wind tunnel's test section using

$$h_d = \frac{2ab}{a+b} \quad (\text{C.2})$$

The parameters a and b are the width and height of the test section and h_d was calculated to have a value of 1.175 m.

The remaining terms required to calculate Re were assumed to be at a pressure of 1 atm and a temperature of 25°C. The values used for μ and ρ were 1.849×10^{-5} kg/ms and 1.184 kg/m³ respectively. These parameters in conjunction with the conservatively selected velocity range, resulted in the calculated minimum and maximum Reynolds numbers of 0.377×10^6 and 1.881×10^6 .

C.3.2 Boundary Layer Thickness

In order to determine the distance the pitot tube needed to be placed from the wall, it was necessary to calculate the expected boundary layer thickness. The boundary layer thickness (δ) was determined for both of the expected Re values determined in section C.3.1.

The boundary layer thickness was approximated using the Blasius solution for flow over a flat plate. The test section surface through which the pitot tube passed was flat and wide, the solution for a flat plate would serve as a reasonable approximation. The lower of the two calculated Reynolds numbers possessed a value which was less than 5×10^5 , suggesting that the intended

flow would be laminar in nature. The boundary layer was therefore calculated using

$$\delta_{lam} = \frac{4.91x}{\sqrt{Re}} \quad (C.3)$$

It should be noted that x is the distance downstream from the start of the test section to where the pitot tube was located and was taken as 0.75 m. The boundary layer thickness was determined to be 6.004×10^{-3} m.

Next δ was determined for the larger of the two calculated values for Re . As the Re in question possessed a value greater than 5×10^5 , it was reasoned to be entering the transitional region. In the interest of being conservative, δ was determined for both the laminar and turbulent instances, the latter of which was calculated using

$$\delta_{turb} = \frac{0.382x}{Re^{\frac{1}{5}}} \quad (C.4)$$

The resulting boundary layer thickness's were 2.685×10^{-3} m and 0.016 m, for the laminar and turbulent instances respectively.

The pitot tube was thus set sufficiently far away from the test section wall at a distance of 200 mm, which would ensure that it would reside in the free stream velocity, regardless of the velocity or nature of the measured air flow.

C.3.3 Air Density

In order to determine the velocity of the air flow through the test section, it was necessary to determine the air density. It was thus necessary to record the ambient conditions over the course of the experimentation.

The air temperature (T_{air}) at the inlet to the wind tunnel test section was noted, as well as the atmospheric pressure (P_{atm}). The gas constant (R) was accepted as 0.287 kJ/kgK, from which it was possible to determine the air density using

$$\rho = \frac{P_{stat}}{RT_{atm}} \quad (C.5)$$

where P_{stat} is the static pressure measured inside the test section, using the pitot tube.

The air density was calculated at the beginning and end of each test conducted in the wind tunnel, with the average being used as the working density. This working density was used in the flow velocity calculation which follows. It should be noted that the differences in density at the beginning and end of each individual test were negligible, as the tests were only conducted at times when there were no significant changes in temperature or atmospheric pressure.

C.3.4 Flow Velocity

Once the density of the air in the test section has been calculated, it becomes possible to determine the air flow velocity by applying Bernoulli's equation to the pitot tube.

Bernoulli's equation states

$$P_{stag} = P_{stat} + P_{dyn} \quad (C.6)$$

where P_{dyn} is the dynamic pressure and P_{stag} is the stagnation pressure. The dynamic pressure is defined as

$$P_{dyn} = \frac{\rho V^2}{2} \quad (C.7)$$

which may be rearranged to calculate the flow velocity

$$V = \sqrt{\frac{2P_{dyn}}{\rho}} \quad (C.8)$$

C.4 Blade Mount Failure and Modification

The results associated with the initial stages of experimentation may be described as inconsistent. This was noted from careful analysis of the resulting transmissibility curves and will be described in detail later in this section. Upon close examination it was determined that the blade mount design was flawed. This section serves to highlight the manner in which it was flawed and describes the actions taken to rectify the problem.

Failure occurred while the excitation mechanism was configured at a setting angle, γ equal to 9° . This event occurred while a measurement was in the process of being recorded at a base excitation frequency of 10.18 Hz, which approaches the natural frequency of the blade. Upon failure, the experiment was immediately halted and the source of failure located. The recorded signal can be seen in figure C.4 and provides some insight into the problem.

It was determined that the means by which the blade attaches to the blade mount was problematic. In order to clarify this explanation, figure C.5 will be considered. Figure C.5 depicts the means by which the fan blade is attached to the blade mount, after the corrective actions have been taken. The blade was fastened in a similar manner prior to the corrective actions, but did not utilize the blade spacer. When one considers this fact, a number of potential pitfalls come to mind. Firstly, the fan blade screws into the blade mount. This means that the orientation of the blade relative to the blade mount is dictated by the distance that the blade has been screwed into the blade mount. This fact is further illustrated when one considers that the thread on the fan blade's shaft is designated as M16, which has a pitch of 2 mm. This means that for every

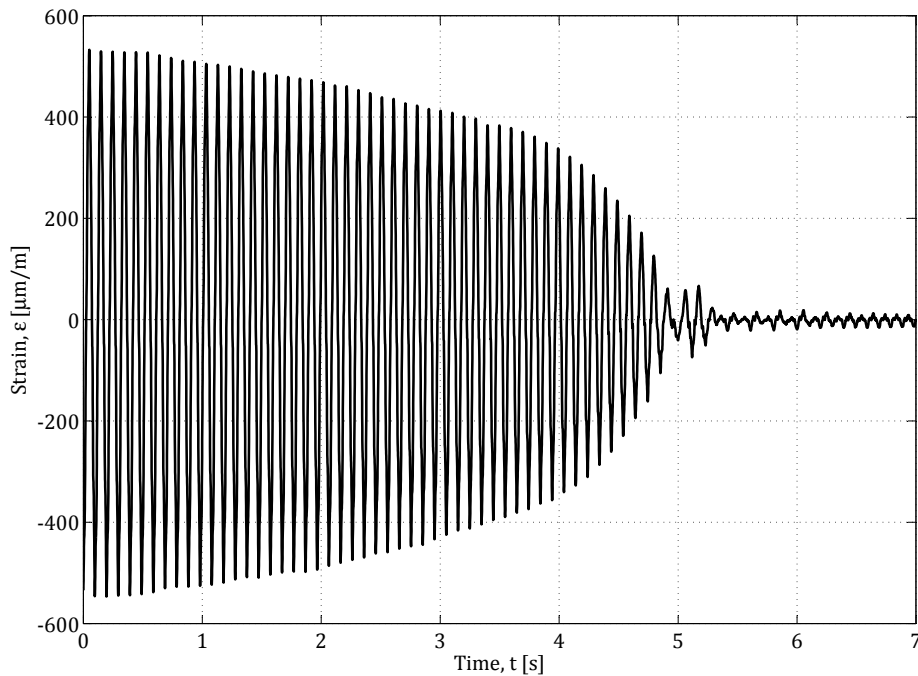


Figure C.4: Recorded strain vs time curve of the fan blade, for a base excitation of 10.18 Hz, emphasising the point of failure.

full rotation of the blade, while screwing it into the blade mount, the blade's locating shoulder will translate 2 mm closer to the blade mount.

The next thing to consider is that the start of the thread was not indicated upon manufacture of the blade mount. As a result, the fan blade could not simply be screwed into the blade mount until all of the thread had been utilized, thereby making the blade orientation self-correcting. This means that the desired orientation seen in figure 5.3 could only be achieved by screwing the fan blade into the blade mount until the fan blade's leading edge was perpendicular to the side of the blade mount. It is at this point in the discussion that the final pitfall of the design must be considered. The threaded portion of the fan blade's shaft does not extend to the locating shoulder, which means that the original assembly would look very similar to the one seen in figure C.5. Even without the presence of the blade spacer, the fan blade could not screw in any further into the blade mount, as there was less than 2 mm of thread left before the non-threaded portion made contact with the blade mount's thread. It was therefore not possible for another full rotation to occur, thereby achieving the desired blade orientation. It then becomes clear that the original configuration failed because the fan blade was only held in place by the small portion of the fan blade's shoulder, which extended into the blade mount. The

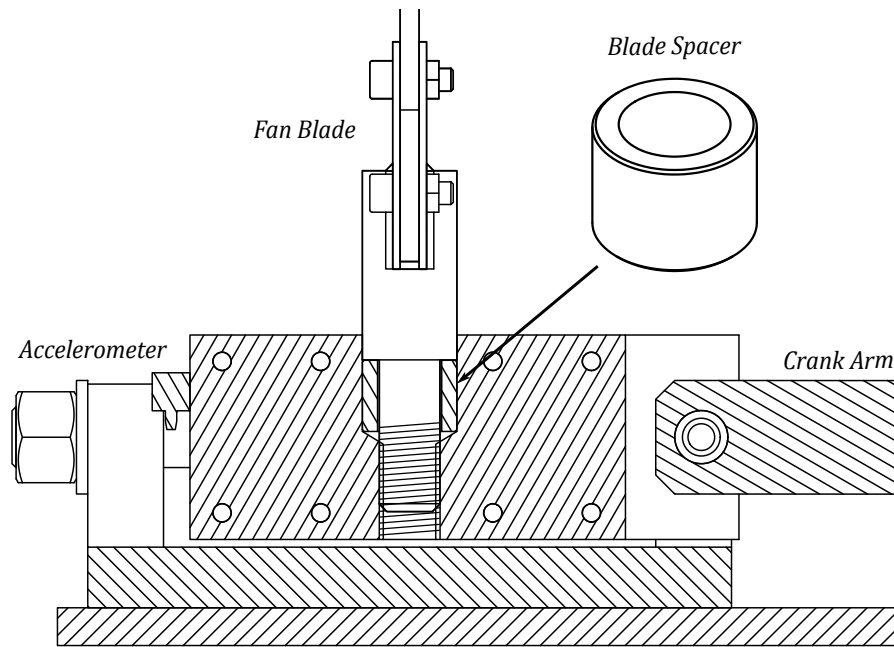


Figure C.5: Sectioned view of base excitation mechanism assembly and un-sectioned fan blade, illustrating fan blade locational fit.

threaded portion of the fan blade was screwed into the blade mount and a grub screw was screwed through the side of the blade mount, thereby tightening the interlocking screw thread.

Thread is not a suitable form of locating an object and the grub screw, on its own, would not be sufficient to act as a supplement in this regard. It was therefore determined that the grub screw must have loosened during the course of the extensive testing, which occurred prior to failure. The aluminium blade mount's thread was then free to wear, resulting in the fan blade's connection to the blade mount becoming progressively more loose. This continued until there was almost no transmission of the induced base displacement to the tip of the blade, thereby damping the blade by means of crude structural damping.

The threaded portion of the blade mount was then re-tapped and the fan blade was screwed in as far as possible. The desired orientation could not be achieved and the fan blade was then screwed anti-clockwise to the last depth at which the orientation had been achieved. The depth of the fan blade's locating shoulder into the blade mount was noted and the length of the proposed blade spacer was calculated. In order to account for potential compression and deflection, the aluminium spacer was manufactured approximately 1.5 mm longer than needed. The fan blade was then screwed in as far as possible and the angle of the blade noted. The remaining length of the spacer, required to screw the fan blade the distance associated with the blade's angular offset, was then shaved off the spacer.

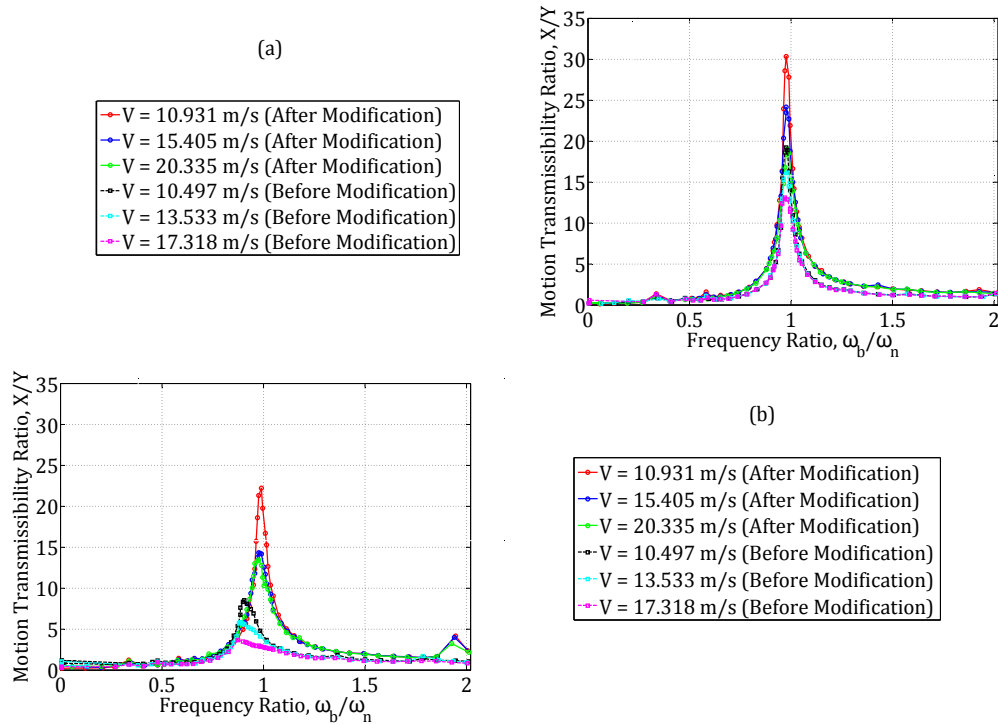


Figure C.6: Comparison of motion transmissibility curves before and after blade mount modification for (a) $\gamma = 0^\circ$ and (b) $\gamma = 9^\circ$.

Figure C.6 illustrates the difference in the blade's vibrational response before and after the alterations to the blade mount has been made. Figure C.6 (a), above shows a difference in the width and height of the motion transmissibility curves. This difference indicates a significant increase in the total damping experienced by the fan blade. Figure C.6 (b), below provides evidence that this effect is not only consistent, but more pronounced at higher setting angles. The curves have actually shifted away from the natural frequency and have traits consistent with systems in which large non-linearities are present. It should also be noted that the curves produced at γ equal to 9° after the modification to the blade-mount interaction are consistent with the curves seen at all other investigated values of γ .

Appendix D

Determining The Damping Ratio

The trend presented in section 5.5.3 of chapter 5 was discovered by analysing the motion transmissibility curves discussed in section 5.5.2. Before figure 5.16 could be plotted, it was necessary to first derive an expression which could be used to calculate the blade's total damping ratio from a transmissibility curve. This was accomplished by modelling a damped single-degree-of-freedom (SDOF) system and then subsequently determining its analytical solution, using the methodology outlined in Meirovitch (2001). The solution could then be used to derive an expression for the motion transmissibility ratio, which would be a maximum when the system's frequency ratio possesses a value of 1. This process is detailed in the appendix which follows below.

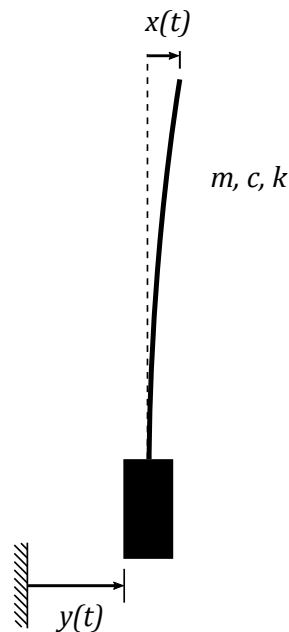


Figure D.1: SDOF system subject to base excitation.

D.1 Common Vibration Parameters

There are a number of common parameters associated with systems which are subject to viscous damping. They have been briefly outlined below for convenience.

The undamped natural frequency of a body or structure is dependent on its equivalent mass (m) and stiffness (k). From these properties it is possible to determine the undamped natural frequency using

$$\omega_n = \sqrt{\frac{k}{m}} \quad (\text{D.1})$$

The damping ratio (ζ) characterizes the response of the system in question and is determined from

$$\zeta = \frac{c}{c_r} \quad (\text{D.2})$$

where c is the viscous damping coefficient and c_r is the critical damping coefficient. The critical damping coefficient is defined as

$$c_r = 2m\omega_n \quad (\text{D.3})$$

The damped natural frequency (ω_d) refers to the frequency at which a body or structure vibrates, when it is subject to a damping force and may be characterized as

$$\omega_d = \omega_n \sqrt{1 - \zeta^2} \quad (\text{D.4})$$

D.2 Base Excitation of a Viscously Damped Cantilever Beam

The blade seen in figure D.1 is subject to base excitation and is modelled as a SDOF mass-spring-damper system. By making use of Newton's second law, the governing equation of motion may be described as

$$m\ddot{x} + c\dot{x} + kx = -m\ddot{y} \quad (\text{D.5})$$

Using the parameters discussed in section D.1, equation D.5 may then be expressed as

$$\ddot{x} + 2\zeta\omega_n\dot{x} + \omega_n^2x = -\ddot{y} \quad (\text{D.6})$$

Equation D.6 may be solved in order to determine the blade's tip displacement, $x(t)$. The analytical solution is obtained by solving for the complimentary ($x_c(t)$) and particular ($x_p(t)$) solutions, the sum of which results in the desired expression for $x(t)$ i.e.

$$x = x_c + x_p \quad (\text{D.7})$$

D.2.1 Complimentary Solution

In order to solve the complimentary solution of equation D.6, the forcing function is made equal to zero. This results in the equation of motion taking the form

$$\ddot{x}_c + 2\zeta\omega_n\dot{x}_c + \omega_n^2x_c = 0 \quad (\text{D.8})$$

Equation D.8 may then be satisfied by the complimentary solution

$$x_c = a_1e^{\lambda_1t} + a_2e^{\lambda_2t} \quad (\text{D.9})$$

The constants a_1 and a_2 are complex numbers and therefore represent a total of four unknowns. Similarly, λ_1 and λ_2 are also complex numbers and may be expressed as

$$\lambda_1 = -\zeta\omega_n + \omega_dj \quad (\text{D.10})$$

$$\lambda_2 = -\zeta\omega_n - \omega_dj \quad (\text{D.11})$$

The above expressions may then be substituted into equation D.9 to yield

$$x_c = e^{-\zeta\omega_nt}(a_1e^{\omega_djt} + a_2e^{-\omega_djt}) \quad (\text{D.12})$$

This expression may then be altered using Euler relations and by defining $A_1 = (a_1 - a_2)j$ and $A_2 = a_1 + a_2$. The expression for the complimentary solution then becomes

$$x_c = e^{-\zeta\omega_nt}(A_1 \sin(\omega_d t) + A_2 \sin(\omega_d t)) \quad (\text{D.13})$$

The terms in the above equation are combined by defining the constant $A = \sqrt{A_1^2 + A_2^2}$ and the angle $\phi = \tan^{-1}(A_2/A_1)$, so that $A_1 = A \cos(\phi)$ and $A_2 = A \sin(\phi)$. The expression subsequently becomes

$$x_c = Ae^{-\zeta\omega_nt} \sin(\omega_d t + \phi) \quad (\text{D.14})$$

The final step is to solve for the constants. This is accomplished by differentiating the complimentary solution and solving using initial values.

$$\dot{x}_c = -\zeta\omega_n Ae^{-\zeta\omega_nt} \sin(\omega_d t + \phi) + \omega_d Ae^{-\zeta\omega_nt} \cos(\omega_d t + \phi) \quad (\text{D.15})$$

By setting t equal to zero in equation D.14, the relation for the blade's initial tip displacement becomes

$$x_c(0) = A \sin(\phi) \quad (\text{D.16})$$

The expression for the blade's initial tip velocity is found in a similar fashion using equation D.15, resulting in the expression

$$\dot{x}_c(0) = -\zeta\omega_n A \sin(\phi) + \omega_d A \cos(\phi) \quad (\text{D.17})$$

The expression for A , as determined from equation D.16 is then substituted into equation D.17. It then becomes possible to solve for ϕ , which results in

$$\tan(\phi) = \frac{\omega_d x_0}{v_0 + \zeta \omega_n x_0} \quad (\text{D.18})$$

Using trigonometry, it may then be shown that

$$\sin(\phi) = \frac{\omega_d x_0}{\sqrt{(v_0 + \zeta \omega_n x_0)^2 + (x_0 \omega_d)^2}} \quad (\text{D.19})$$

which is in turn substituted into equation D.16 to find the constant

$$A = \sqrt{\frac{(v_0 + \zeta \omega_n x_0)^2 + (x_0 \omega_d)^2}{\omega_d^2}} \quad (\text{D.20})$$

This complimentary solution to the equation of motion is thus

$$x_c = \sqrt{\frac{(v_0 + \zeta \omega_n x_0)^2 + (x_0 \omega_d)^2}{\omega_d^2}} \sin(\phi) \quad (\text{D.21})$$

with

$$\phi = \left(\arctan \left(\frac{\omega_d x_0}{v_0 + \zeta \omega_n x_0} \right) \right) \quad (\text{D.22})$$

D.2.2 Particular Solution

As previously discussed, the blade is subject to a harmonic base excitation. Furthermore, the nature of the excitation is carefully controlled and as a result, its parameters are well defined. The displacement of the base may be expressed as

$$y = Y \sin(\omega_b t) \quad (\text{D.23})$$

where Y is half the base amplitude and ω_b is the excitation frequency.

As is the custom when solving these types of problems, the particular solution of equation D.6 is assumed to be similar in form to its right-hand side. This results in the particular solution and its subsequent derivatives being

$$x_p = B \sin(\omega_b t) + C \cos(\omega_b t) \quad (\text{D.24})$$

$$\dot{x}_p = \omega_b B \cos(\omega_b t) - \omega_b C \sin(\omega_b t) \quad (\text{D.25})$$

$$\ddot{x}_p = -\omega_b^2 B \sin(\omega_b t) - \omega_b^2 C \cos(\omega_b t) \quad (\text{D.26})$$

It should be noted that B and C are constants which will need to be determined and that the second derivative of equation D.23 is

$$\ddot{y} = -\omega_b^2 Y \sin(\omega_b t) \quad (\text{D.27})$$

By substituting the above expressions into the equation of motion, the constants may be determined to be

$$B = \frac{Y\omega_b^2(\omega_n^2 - \omega_b^2)}{(\omega_n^2 - \omega_b^2)^2 + (2\zeta\omega_n\omega_b)^2} \quad (\text{D.28})$$

$$C = \frac{-Y\omega_b^2(2\zeta\omega_n\omega_b)}{(\omega_n^2 - \omega_b^2)^2 + (2\zeta\omega_n\omega_b)^2} \quad (\text{D.29})$$

The particular solution therefore becomes

$$x_p = \frac{Y\omega_b^2}{(\omega_n^2 - \omega_b^2)^2 + (2\zeta\omega_n\omega_b)^2} ((\omega_n^2 - \omega_b^2) \sin(\omega_b t) - (2\zeta\omega_n\omega_b) \cos(\omega_b t)) \quad (\text{D.30})$$

As done in the complementary solution, we define $D = \sqrt{D_1^2 + D_2^2}$ and $\theta = \tan^{-1}(\frac{D_2}{D_1})$ so that $D_1 = D \cos(\theta)$ and $D_2 = D \sin(\theta)$. By stating $D_1 = (\omega_n^2 - \omega_b^2)$ and $D_2 = (2\zeta\omega_n\omega_b)$, the particular solution becomes

$$x_p = \frac{Y\omega_b^2}{(\omega_n^2 - \omega_b^2)^2 + (2\zeta\omega_n\omega_b)^2} (D_1 \sin(\omega_b t) - D_2 \cos(\omega_b t)) \quad (\text{D.31})$$

If we recall that $\sin(\alpha - \beta) = \sin(\alpha) \cos(\beta) - \cos(\alpha) \sin(\beta)$, it becomes apparent that the particular solution may be written as

$$x_p = \frac{Y\omega_b^2}{(\omega_n^2 - \omega_b^2)^2 + (2\zeta\omega_n\omega_b)^2} (D \sin(\omega_b t - \theta)) \quad (\text{D.32})$$

where

$$D = \sqrt{(\omega_n^2 - \omega_b^2)^2 + (2\zeta\omega_n\omega_b)^2} \quad (\text{D.33})$$

and

$$\theta = \tan^{-1}\left(\frac{2\zeta\omega_n\omega_b}{\omega_n^2 - \omega_b^2}\right) \quad (\text{D.34})$$

Finally, the particular solution may be simplified to

$$x_p = \frac{Y\omega_b^2}{\sqrt{(\omega_n^2 - \omega_b^2)^2 + (2\zeta\omega_n\omega_b)^2}} \sin(\omega_b t - \theta) \quad (\text{D.35})$$

D.2.3 Transmissibility

The final solution to the equation of motion may now be expressed as

$$x = \sqrt{\frac{(v_0 + \zeta\omega_n x_0)^2 + (x_0\omega_d)^2}{\omega_d^2}} \sin(\phi) + \frac{Y\omega_b^2}{\sqrt{(\omega_n^2 - \omega_b^2)^2 + (2\zeta\omega_n\omega_b)^2}} \sin(\omega_b t - \theta) \quad (\text{D.36})$$

At this stage, it is convenient to examine the initial conditions of the system in question. The starting position of the blade corresponds to an initial displacement of $x_0 = 0$ and is stationary, $v_0 = 0$. As a result, equation D.36 becomes

$$x = \frac{Y\omega_b^2}{\sqrt{(\omega_n^2 - \omega_b^2)^2 + (2\zeta\omega_n\omega_b)^2}} \sin(\omega_b t - \theta) \quad (\text{D.37})$$

If the displacement response of both the blade's tip and the base are known, it is possible to write an expression for the motion transmissibility of the system in question. This process begins by defining the frequency ratio

$$r = \frac{\omega_b}{\omega_n} \quad (\text{D.38})$$

where ω_b is base excitation frequency and ω_n is the natural frequency of the blade. Equation D.36 may now be written in terms of the frequency ratio. For convenience, equation D.37 has been written as

$$x = X \sin(\omega_b t - \theta) \quad (\text{D.39})$$

where

$$X = \frac{Yr^2}{\sqrt{(1 - r^2)^2 + (2\zeta r)^2}} \quad (\text{D.40})$$

and

$$\theta = \tan^{-1}\left(\frac{2\zeta r}{1 - r^2}\right) \quad (\text{D.41})$$

The motion transmissibility ratio may now be defined as the ratio between blade's tip and base displacement

$$R = \frac{X}{Y} \quad (\text{D.42})$$

which becomes

$$R = \frac{r^2}{\sqrt{(1 - r^2)^2 + (2\zeta r)^2}} \quad (\text{D.43})$$

The motion transmissibility ratio is at a maximum value when

$$\frac{dR(r)}{dr} = 0 \quad (\text{D.44})$$

which results in the expression

$$0 = \frac{2((2\zeta^2 - 1)r^3 + r)}{((4\zeta^2 - 2)r^2 + r^4 + 1)^{\frac{3}{2}}} \quad (\text{D.45})$$

Upon further manipulation, the above equation results in an expression for r when R is a maximum, which will be defined as

$$r^* = \sqrt{\frac{1}{1 - 2\zeta^2}} \quad (\text{D.46})$$

This expression is then substituted into equation D.43 resulting in

$$R^* = \frac{1}{2\zeta\sqrt{1-\zeta^2}} \quad (\text{D.47})$$

R^* is the value for the motion transmissibility ratio, when it is at a maximum. This equation can then be rearranged in order to find an expression which can be used to solve for the damping ratio, assuming the value for R^* is known. As a result, the damping ratio may be found from

$$\zeta = \sqrt{\frac{1 - \sqrt{1 - \frac{1}{R^{*2}}}}{2}} \quad (\text{D.48})$$

Appendix E

Blade Lift and Drag Data

Chapter 6 details the investigation's numerical evaluation. In order to calculate the lift and drag forces imparted on the blade during vibration, it was necessary to obtain the lift and drag data pertaining to the fan blade under investigation. The data in question was obtained from Riegels (1961) and was used to modify a flat plate blade into the profile illustrated in figure 3.2.

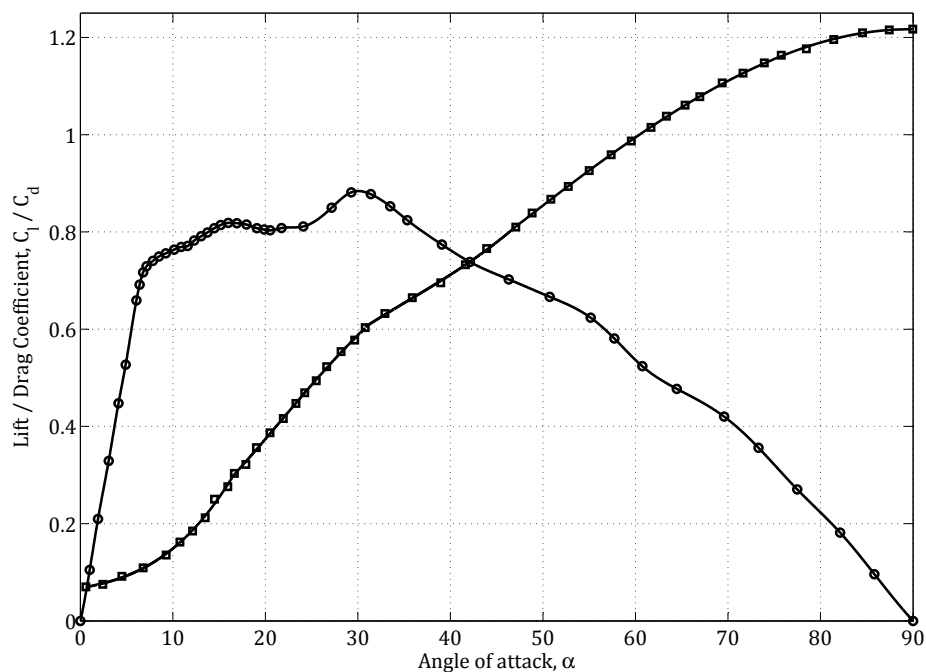


Figure E.1: Lift (C_l) and drag (C_d) coefficient data relative to the blade's angle of attack.

The lift and drag data may be seen in figure E.1. The published data was digitized by recording a number of data points relative to a reference axis. The curves were then reconstructed by separating the digitized data points into groups and constructing polynomials.

The polynomial curves have been summarized in the form of inequalities below.

$$C_l = \begin{cases} 2.1364 \times 10^{-4} \alpha^2 + 0.1078 \alpha - 9.7096 \times 10^{-4}, & \text{if } \alpha < 6.41 \\ 0.0058 \alpha^3 - 0.1453 \alpha^2 + 1.2182 \alpha - 2.6755, & \text{if } 6.41 \leq \alpha < 9.24 \\ -2.5782 \times 10^{-4} \alpha^3 + 0.0099 \alpha^2 - 0.1151 \alpha - 1.1778, & \text{if } 9.24 \leq \alpha < 17.96 \\ -3.3651 \times 10^{-4} \alpha^3 + 0.0208 \alpha^2 - 0.4318 \alpha - 3.8015, & \text{if } 17.96 \leq \alpha < 20.52 \\ 0.0037 \alpha^3 - 0.133 \alpha^2 + 2.0712 \alpha - 11.1177, & \text{if } 20.52 \leq \alpha < 31.32 \\ 0.0002 \alpha^3 - 0.014 \alpha^2 + 0.3589 \alpha - 2.3554, & \text{if } 31.32 \leq \alpha < 57.72 \\ -6.781 \times 10^{-5} \alpha^3 + 0.0134 \alpha^2 - 0.8872 \alpha + 20.3343, & \text{if } 57.72 \leq \alpha < 69.59 \\ -1.1324 \times 10^{-6} \alpha^3 + 0.0001 \alpha^2 - 0.0164 \alpha + 1.398, & \text{if } 69.59 \leq \alpha \end{cases} \quad (\text{E.1})$$

$$C_d = \begin{cases} 0.0002 \alpha^2 + 0.0032 \alpha + 0.0675, & \text{if } \alpha < 16.65 \\ 0.0012 \alpha^2 - 0.0041 \alpha + 0.1178, & \text{if } 16.65 \leq \alpha < 30.79 \\ -0.0013 \alpha^2 + 0.0576 \alpha - 0.2893, & \text{if } 30.79 \leq \alpha < 47.06 \\ 0.0003 \alpha^2 + 0.0022 \alpha + 0.2868, & \text{if } 47.06 \leq \alpha \end{cases} \quad (\text{E.2})$$

The polynomial inequalities were used as if statements in the numerical evaluation, to determine the blade's drag and lift coefficient for a given angle of attack.

List of References

- Antoniou, A. (2007). Part 1: Fir filters - windows method. In: *Tutorial ISCAS 2007*.
- Baker, W.E., William, E., Woolam, E. and Young, D. (1967). Air and internal damping of thin cantilever beams. *International Journal of Mechanical Sciences*, vol. 9, pp. 743 – 766.
- Bambill, D.V., Escanes, S.J. and Rossit, C.A. (2003). Forced vibrations of a clamped-free beam with a mass at the free end with an external periodic disturbance acting on the mass with applications in ships' structures. *Ocean Engineering*, vol. 30, pp. 1065 – 1077.
- Blevins, R.D. (1974). *Flow Induced Vibration of Bluff Structures*. Ph.D. thesis, California Institute of Technology.
- Blevins, R.D. (1977). *Flow-Induced Vibration*. Van Nostad Reinhold.
- Blevins, R.D. (2009). *Harris' Shock and Vibration Handbook (Sixth Edition)*, chap. Vibration of Structures Induced by Fluid Flow, pp. 30.1 – 30.20. McGraw-Hill: New York, Chicago, San Francisco, Athens, London, Madrid, Mexico City, Milan, New Delhi, Singapore, Sydney, Toronto.
- Bredell, J., Kröger, D. and Thiart, G. (2006). Numerical investigation into aerodynamic blade loading in large axial flow fans operating under distorted inflow conditions. *R & D Journal, of the South African Institution of Mechanical Engineering*, vol. 22, pp. 11 – 17.
- Cengel, Y. and Cimbala, J. (2010). *Fluid Mechanics Fundamentals and Applications*. McGraw-Hill: New York, Chicago, San Francisco, Athens, London, Madrid, Mexico City, Milan, New Delhi, Singapore, Sydney, Toronto.
- Cook, R.D., Malkus, D.S., Plesha, M.E. and Witt, R.J. (2002). *Concepts and Applications of Finite Element Analysis (Fourth Edition)*. John Wiley & Sons.
- Dormand, J. and Prince, P. (1980). A family of embedded runge-kutta formulae. *Journal of Computational and Applied Mathematics*, vol. 6, pp. 19 – 26.
- Du Buisson, J. (1988). *The effectiveness of commercially available components used to decrease the aerodynamic drag force on heavy motor vehicles*. Master's thesis, Stellenbosch University.

- Erturk, A. and Inman, D.J. (2008). On mechanical modeling of cantilevered piezoelectric vibration energy harvesters. *Journal of Intelligent Material Systems and Structures*, vol. 19, pp. 1311 – 1325.
- Harris, C.M. and Piersol, A. (2009). *Harris' Shock and Vibration Handbook (Sixth Edition)*, chap. Introduction to the Handbook, pp. 1.1 – 1.27. McGraw-Hill: New York, Chicago, San Francisco, Athens, London, Madrid, Mexico City, Milan, New Delhi, Singapore, Sydney, Toronto.
- Hodges, D.H. and Pierce, G.A. (2011). *Introduction to Structural Dynamics and Aeroelasticity*. Cambridge University Press.
- Inman, D. (2009). *Engineering Vibrations*. Prentice Hall.
- Kammerer, A. and Abhari, R.S. (2009). Experimental study on impeller blade vibration during resonance - part 2: Blade damping. *Journal of Engineering for Gas Turbines and Power*.
- Kielb, J.J. and Abhari, R.S. (2003). Experimental study of aerodynamic and structural damping in a full-scale rotating turbine. *Journal of Engineering for Gas Turbines and Power*.
- Kimber, M., Lonergan, R. and Garimella, S.V. (2009). Experimental study of aerodynamic damping in arrays of vibrating cantilevers. *Journal of Fluids and Structures*.
- Meirovitch, L. (2001). *Fundamentals of Vibrations*. McGraw-Hill, New York.
- Muiyser, J. (2014 January). Personal communication. Stellenbosch University.
- Muiyser, J., Van der Spuy, S., Els, D. and Zapke, A. (2014). Measurement of air flow and blade loading at a large-scale cooling system fan. *R & D Journal, of the South African Institution of Mechanical Engineering*, vol. 30, pp. 30 – 38.
- Riegels, F. (1961). *Results from Wind Tunnel Investigations - Theoretical Foundations*. London Butterworths.
- Sadiku, M.N.O. and Obiozor, C.N. (2000). A simple introduction to the method of lines. *International Journal of Electrical Engineering Education*, vol. 37, pp. 282 – 296.
- Sedlar, D., Lozina, Z. and Vucina, D. (2011). Experimental investigation of the added mass of the cantilever beam partially submerged in water. *Technical Gazette*.
- Shirzadeh, R., Guillaume, P., Runacres, M. and Ahmadi Bidakhvidi, M. (2012). Experimental and numerical study of aerodynamic damping of a piezoelectric fan. In: *15th International Conference on Experimental Mechanics*.
- Tarnopolsky, A.Z., Lai, J.C.S. and Fletcher, H.N. (2002). Aerodynamic damping of randomly excited plates in stationary and moving air. *Journal of Sound and Vibration*.

- Timoshenko, S., Young, D. and Weaver, W. (1974). *Vibration Problems in Engineering*. John Wiley and Sons, New York.
- Venter, S. (1990). *The effectiveness of axial flow fans in A-frame plenums*. Ph.D. thesis, University of Stellenbosch.
- Vu, V., Thomas, M., Lakis, A. and Marcouiller, L. (2007). Effect of added mass on submerged vibrated plates. In: *Proceedings of 25th Seminar on Machinery Vibration*, 7, pp. 40–1. Canadian Machinery Vibration Association CMVA.
- Wright, J. and Cooper, J. (2014). *Introduction to Aircraft Aeroelasticity and Loads*. John Wiley & Sons.